ISSN 0915-9916

Readout

HORIBA Technical Reports

August 2023
English Edition No. 57

HORIBA's Initiatives in the Next-Generation Energy and Environment Fields

2022 Masao Horiba Awards

Analytical and measurement technologies that contribute to the use of hydrogen for a decarbonized society

HORIBA

https://www.horiba.com/publications/readout/

Readout
HORIBA Technical Reports
August 2023 No.57

HORIBA's Initiatives in the Next-Generation Energy and Environment Fields

2022 Masao Horiba Awards

Analytical and measurement technologies that contribute to the use of hydrogen for a decarbonized society

Realizing a carbon neutral society is accelerating worldwide and innovation in the energy field is expected to help achieve both environmental conservation and industrial development. This issue will introduce the Masao Horiba Awards, under the theme of "Analytical and measurement technologies that contribute to the use of hydrogen for a decarbonized society," as well as HORIBA's technologies and initiatives that contribute to the realization of a sustainable society.

In search of fully bloomed wisteria flowers, I visited a garden in the Chubu region. I enjoyed the colors of the flowers and the greenery of the trees along with the fragrance of the flowers in the rain.
-Photographer MATSUI Hideo-
(Member of Nikakai Association of Photographers)

Name of this Journal

This Journal is named "Readout" in the hope that "the products and technology we have created and developed will be read out and so become widely known".

Foreword

Prospects for a Hydrogen Energy Based Society

NAKAMURA Hiroshi

Corporate Officer
Chief Technology Officer
R&D Division General Manager
HORIBA, Ltd.
Doctor of Engineering

The spread of the new coronavirus caused a slowdown in economic activity in many countries around the world, with real GDP growth of -6.3% in 2020, the largest drop since World War II. However, as a response to the crisis, many countries have decided to adopt environmentally sustainable economic measures. The European Union launched its "Green Recovery" measures and announced the "European Green Deal," with the goal of halving greenhouse gas emissions by 2030 and reducing them to virtually zero by 2050. The establishment of the European Recovery Fund was also announced, attracting attention as a fund to support environmentally friendly policies. The U.S. also announced environmentally friendly policies under the Biden administration and announced at the G7 Summit that it would halve its greenhouse gas emissions by 2030.

The European Commission has published a "European Hydrogen Strategy for Climate Neutrality", which states that "green hydrogen", hydrogen produced from renewable energy sources as primary energy, is essential to achieving "carbon neutrality" in 2050. This strategy set a goal of installing at least 6 GW of hydrogen production facilities using water electrolysis by 2024 and 40 GW by 2030. Germany and France have also developed national strategies and plan to invest heavily in hydrogen production, aiming to have 5 GW and 6.5 GW of hydrogen production capacity by 2030, respectively.

The Haber-Bosch process, developed in the early 1900s, made possible the mass production of chemical fertilizers by producing ammonia from nitrogen and hydrogen, which has supported the rapid increase in population since the 20th century. Even today, hydrogen is widely used for petroleum refining and petrochemical products, in addition to ammonia production. However, as of 2020, 95% of the hydrogen used in industry will be so-called "gray hydrogen," produced by steam reforming of fossil fuels, which emits CO_2 during production.

In order to achieve carbon neutrality, hydrogen is once again attracting attention as "green hydrogen," which is produced from renewable energy sources such as

solar and wind power generation, where the unstable power supply is an issue. In addition to conventional industrial applications, hydrogen can be used as fuel for fuel cell vehicles, hydrogen reduction in steelmaking, hydrogen engines that burn hydrogen directly, and gas turbine power generation after conversion to ammonia which is easy to transport.

HORIBA's founding product, the pH meter is based on electrochemical reactions, which are indispensable for the utilization of hydrogen and the catalyst technology. This technology which is indispensable for the realization of a carbon neutral society, was learned from Germany in the early 1900s by the founder Masao Horiba's father, Nobukichi Horiba, a researcher at Kyoto University. He supported the development of chemical engineering in Japan. It can be said that the research and technology that Horiba was involved in at the time of its founding and even before that have led to the company's current efforts to address social issues such as the utilization of hydrogen. Since the late 1990s, we have also been developing technologies for the direct measurement of hydrogen and moisture, and for the measurement of fuel reforming gas and hydrogen combustion gas for the development of fuel cell vehicles, which were booming in the automotive industry. In 2018, we acquired HORIBA FuelCon (HFC), located in Sachsen-Anhalt, Germany, expanding our portfolio to include evaluation equipment, manufacturing equipment, and production quality inspection equipment for fuel cell and water electrolysis research and development. In January 2023, HFC started operation of a new plant "eHUB" (Figure 1), which has tripled its production capacity to meet the rapidly growing demand for manufacturing and evaluation equipment for water electrolysis systems in Europe.

Hydrogen has a very high energy density per unit mass compared to other energy sources. To obtain the same energy as 1 L of liquid gasoline, about 3,000 L of gaseous hydrogen is required, which converted to mass is 270 g of hydrogen for 750 g of gasoline. Incidentally, to store this energy in today's lithium-ion batteries would require 100 times that amount, about 27 kg of mass. In comparison, hydrogen has a very high energy density per unit mass, and thus has potential as a source of energy for mobility and as a means of energy transportation, where mass is an important factor. On the other hand, there are a wide range of technical issues that need to be addressed in order to make it commercially viable, such as its difficult handling due to its gaseous state in the standard state, and its low efficiency when converted to other forms of energy such as electricity, heat, or e-fuel.

HORIBA hopes to contribute to the realization of a carbon neutral society by applying its analysis and measurement technologies to the search for new materials for fuel cells and water electrolyzers, the development of hydrogen combustion technology, and the development of catalysts for the efficient production of synthetic fuels from hydrogen and CO_2.

Figure 1 Exterior of new facility "HORIBA eHUB".

* Editorial note: This content in based on HORIBA's investigation at the year of issue unless otherwise stated.

Scenarios for Realizing Carbon Neutrality

YAMAJI Kenji
President
Research Institute of Innovative Technology for the Earth (RITE)
Dr. Eng.

Global warming is a global issue that should be tackled by the entire human race over the long term. Rather than simply addressing the global warming issue, it is necessary to achieve a balance between the 17 goals of the SDGs (United Nations Goals for Sustainable Development) and the 3Es (energy security, economic efficiency, and environmental compatibility), which are the basic goals of Japan's energy policy. If we lower the baseline of CO_2 emissions through social innovations to achieve the SDGs, and then build a system to produce and efficiently use clean secondary energy such as electricity and hydrogen without CO_2 emissions through technological innovations, we can create a scenario for the realization of carbon neutrality, which will solve the global warming problem.

Introduction

The Russian invasion of Ukraine, which began in February 2022, is causing a serious energy crisis. The major difference from the two oil crises of the 1970s being that this crisis occurred as the world as a whole was making a major move toward achieving carbon neutrality (decarbonization) as a measure against global warming. Of course, there are many other differences from those days. The prices of not only oil but also natural gas and coal are increasing rapidly, and the energy demand of developing countries is larger than that of developed countries.

Even before the invasion, energy prices were on the rise as fossil resource development was curbed by the trend toward decarbonization and reduced demand due to the spread of the new coronavirus infection. Then came the invasion. Russia is the world's largest exporter of natural gas and one of the top three exporters of oil and coal. The sanctions against Russia have led to a sharp decline in Russian energy exports to Europe and other countries, but imports by China, India, and other emerging economies have complicated the situation. Particularly serious is the price of natural gas in Europe, where the spot price in 2022 is 10 times higher than it was two years ago. Europe is expected to increase its imports of liquefied natural gas (LNG) in the future, and competition for LNG has begun, with LNG prices skyrocketing. This will hinder developing countries from switching from coal to natural gas and will be an obstacle to global warming countermeasures. Despite the energy crisis, global warming countermeasures cannot be halted.

In order to solve the global warming problem, it is ultimately necessary to achieve net zero greenhouse gas emissions (carbon neutrality). The long-term goal of the Paris Agreement is to "keep the global average temperature increase below 2°C above pre-industrial levels and pursue efforts to limit it to 1.5°C." To achieve this goal, the goal was to achieve a decarbonized society, in other words, carbon neutrality, in which global greenhouse gas emissions are reduced to virtually (net) zero by the second half of this century. However, the IPCC Special Report on the 1.5°C target (2018) stated that carbon neutrality must be achieved by 2050 in order to reach the 1.5°C target, and this triggered a movement to raise the long-term target to carbon neutrality by 2050, with Europe taking the lead. The increased ambition to achieve carbon neutrality by 2050 quickly spread around the world, including the U.S. under the Biden administration. The Paris Agreement's effort target is now becoming the main goal. More than 80% of Japan's greenhouse gas emissions are energy-derived CO_2. This paper will consider how to achieve carbon neutrality in the midst of the energy crisis.

Carbon Neutrality Achieved through Innovation

Energy systems that optimally realize carbon neutrality will require the mobilization of various innovations in both technology and society. The central focus is on secondary energy media that can be used cleanly and efficiently, with electricity being used at present, and hydrogen being used as a fuel and heat source in the future. Figure 1 shows the composition of the realization of carbon neutrality by placing electricity and hydrogen at the center and arranging various innovations.

Since electricity and hydrogen can be produced from a variety of resources, technological innovation can lead to low-carbon and decarbonization. Assuming CCUS (CO_2 Capture, Utilization, and Storage) technology, the use of fossil resources as well as nuclear power and renewable energy is not excluded. However, since power sources with naturally fluctuating output, such as photovoltaic and wind power, are expected to be introduced on a large scale in the future, the role of energy storage technologies, including electrolytic hydrogen storage (PtG), will become important. In addition, flexibility and robustness will be required for power networks that interconnect naturally fluctuating power sources.

The use of electricity will continue to increase with the development of the digital society, the electrification of the transportation sector, and the increase in heat supply by heat pumps. Distributed power sources such as photovoltaic power generation and cogeneration, storage batteries for electric vehicles, and hot water storage tanks for heat pump water heaters will also be increasingly utilized.

The system of electric power transmission and distribution is undergoing major changes as a result of the power system reform, and it is expected to shift from the traditional form of supplying electricity in response to demand to network formation and operation that integrates supply and demand. The use of digital technology will support such network innovation.

The industrial sector is expected to utilize hydrogen as well as promote further electrification. The theme of 2022 Masao Horiba Awards was also on analysis and measurement technologies that contribute to the utilization of hydrogen. In addition to the use of hydrogen in fuel cells, demand for hydrogen is expected to increase for combustion power generation and heat utilization, including use as fuel ammonia, and as a raw material for various synthetic fuels and chemical substance synthesis with the progress of carbon recycling. Of course, the hydrogen used in this process must be produced in a CO_2-free manner.

If the super-smart society (Society 5.0) realizes a sharing circular economy, not only will energy demand be greatly reduced through the substitution of energy and materials by information, but the system integration of energy and information will be further advanced, and distributed resources such as facilities located on the demand side will

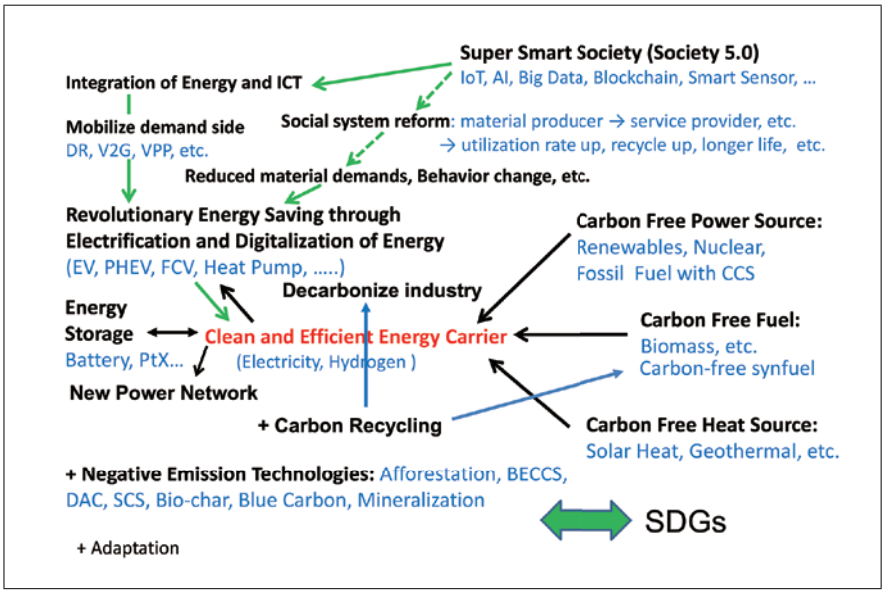

Figure 1 Composition of carbon neutral realization.

be utilized more efficiently. The number of information devices such as smart phones that realize various functions through application software will continue to increase, and the substitution of energy and materials by information is expected to advance at the device level as well. As a result, we can envision the possibility of revolutionary energy savings through electrification and digitalization. However, it will be necessary to cope with the increased demand for electricity associated with information processing, such as blockchain, and it will be necessary to coordinate with innovations in the information field, such as quantum computers.

Composition of Carbon Neutral Realization

If we look at human economic activities as a whole, such as steelmaking, cement production, chemical industry, and agriculture, it will be difficult to achieve zero emissions of greenhouse gases even if all the above measures are implemented. Therefore, it is necessary to prepare technologies to capture CO_2 from the atmosphere, such as afforestation, DAC (CO_2 capture from the atmosphere), BECCS (biomass energy use with CCS (CO_2 capture and storage)), and mineral fixation of CO_2 using waste concrete.

Then, it is necessary to strike a balance between adaptation to possible global warming and realization of goals other than global warming in the SDGs (United Nations Goals for Sustainable Development). From a broader perspective, if the baseline of CO_2 emissions can be lowered through social innovations aimed at achieving the SDGs, and if clean secondary energy such as electricity and hydrogen can be produced and used efficiently without CO_2 emissions through technological innovations, a solution to the global warming problem can be found. emission-free production and efficient use of clean secondary energy such as electricity and hydrogen through technological innovation.

Rebuilding the 3 E's with Nuclear Energy

There are various opinions about nuclear power, but it is certainly an effective technology for combating global warming as an energy source that does not emit CO_2. At the GX (Green Transformation) Implementation Conference in August 2022, Japan made clear its stance on replacing and building new nuclear power plants to make full use of nuclear energy. The government has announced that it will move forward with the restart of existing nuclear power plants, and has begun to take concrete steps to extend operation periods and develop next-generation reactors. In February 2023, the Japanese government adopted a cabinet decision on a basic policy toward the realization of GX and drafted a law on the promotion of a smooth transition to a decarbonized growth-oriented economic structure.

In the wake of the Russian military invasion of Ukraine, the importance of energy security and economic efficiency has been reaffirmed in energy policy, which had been biased toward global warming countermeasures, and the basic policy of simultaneously achieving the 3 E's of energy security, economic efficiency, and environmental measures is being reaffirmed. In this context, it is noteworthy that the government has begun to actively address nuclear energy policy, which it had avoided for political reasons.

However, the harsh reality surrounding nuclear power will not change. We cannot expect a revival of nuclear power unless we focus on priority policies with realism. In this regard, I believe that restarting nuclear power plants and extending their operation periods should be carried out as a matter of course, but I feel that the development of next-generation reactors is in jeopardy. It is true that new and additional facilities are needed to develop human resources, but this can be handled with innovative light water reactors with enhanced safety. What is questionable in the discussion of next-generation reactors is that fast reactors and nuclear fusion are still being discussed. These have been promoted through national projects and international joint development, but even after more than 50 years of development, they have not reached the goal of commercialization.

Since the late 1950s, various types of reactors have been developed, including fast breeder reactors, high-temperature gas reactors, and molten salt reactors, but in the 1960s, light water reactors were eventually commercialized and introduced worldwide. The United Kingdom, which developed and commercialized the gas reactor, has also chosen the LWR as its future reactor of choice for new construction.

Among the next-generation reactors, I am focusing on the small modular reactor (SMR), which is expected to improve safety and economics through mass production of small reactors. The smaller the reactor, the larger its surface area relative to its volume, and the easier it is to cool than larger reactors. This is called inherent safety

improvement. On the other hand, a module is a production system in which a set of components with uniform standards is manufactured in a factory and assembled as a unit, and the unit is further assembled and constructed on site. This can be likened to a prefabricated house. Conventional nuclear power plants are one-of-a-kind, with construction taking place on site, even for the same design type, while SMRs are expected to have high quality control and shortened construction periods because most of the parts will be manufactured in a factory.

The SMR concept has actually been around for a long time. None of them were realized, but as I recall, GE was developing a sodium-cooled fast reactor named PRISM in the 1980s. There was also a plan to build a high-temperature gas-cooled reactor developed by Germany as a modular reactor in South Africa. However, it could not compete with the light water reactors in practical use.

Among the SMRs that are once again in the spotlight, we believe that the concept of using small light water reactors is promising. This is because small LWRs are already in practical use to power submarines, aircraft carriers, and icebreakers. Japan has a long history of developing LWRs, including the "Mutsu". The reason why small-sized LWRs have not been commercialized except for military use and icebreakers is largely due to the social reason that the market could not be developed due to concerns about nuclear power. However, small power reactors can be used in remote areas and as mobile power generating vessels. We have high expectations for the development of SMRs for light water reactors.

Importance of Expanding the Field of View

Mobilization of various technological and social innovations to achieve carbon neutrality requires an expansion of horizons. In terms of spatial expansion, various efforts will be required, ranging from local community initiatives to international collaboration and sectoral coupling to link industries and demand categories. On the time axis, efforts during the transition period leading to the realization of carbon neutrality will also be important. The realization of carbon neutrality requires efforts from a wide range of perspectives, including technology, society, local economies, and international politics.

The reality, however, is harsh. COP26 in November 2021 was repeatedly reported that Japan won the Fossil Prize, but the reason for the award was Prime Minister Fumio Kishida's announcement of "zero-emission thermal power generation" using hydrogen and ammonia. In addition, Norway received the Fossil Prize for its promotion of CCS (CO_2 Capture and Storage), and France received the Fossil Prize for its announcement to build new nuclear power plants. Zero emissions from thermal power, CCS, and nuclear power are all important measures to combat global warming. To realize the lofty goal of carbon neutrality, narrowing the options by excluding specific technologies in this way is a major obstacle.

The global warming problem has a structure in which the burden of countermeasures is borne by each region, but the benefits of the countermeasures benefit the entire world. In order to deal with the problem of such structure, it is extremely important to maintain coordinated actions throughout the world. Creating a situation where major countries leave or excluding specific technologies will destroy the coordination and lead to the self-destruction of global warming countermeasures. Realizing a tough goal such as global decarbonization requires acknowledging the diversity of technologies and cultures and mobilizing all measures.

In addition to individual innovative technologies that directly contribute to CO_2 reduction, such as hydrogen utilization and CCUS, the realization of carbon neutrality also requires the use of versatile common infrastructure technologies such as digital technology, power electronics, analysis and measurement technology, biotechnology, and urban management technology, which at first glance may seem unrelated to CO_2 reduction.

GX (Green Transformation) Policy Development

In the past few years, policies with various nicknames, such as the Green Growth Strategy and the Clean Energy Strategy, have been proposed, but these trends are now being bundled together in the GX (Green Transformation) Council. The comprehensive approach that energy and environmental policies should have, such as decarbonization to be achieved together with stable energy supply and maximum utilization of nuclear power as well as renewable energy, is beginning to appear with concrete policies. The government is preparing a 20 trillion yen GX Transitional Bond to induce 150 trillion yen in private investment toward carbon neutrality.

While it is politically easy to advocate the adoption of

renewable energy as a main source of power and carbon neutrality, both of which are highly supported by the public, it was politically difficult to mention the realization of a stable energy supply and the utilization of nuclear power. The soaring fuel prices and growing concerns about supply instability triggered by the Russian military invasion of Ukraine certainly helped, but another important factor was the foreseeable stability of the government, as no national elections were scheduled in the near future. In this respect, the GX Executive Council's decision was the fruit of a political decision.

However, the draft of the GX Executive Conference is expected to be difficult to materialize because of its diverse content. For example, the introduction of growth-oriented carbon pricing, specifically the introduction of emissions trading (GX-ETS) and a carbon levy, has been proposed, but the details of the system such as the timing of the introduction and the establishment of rules for paid auctions, have only been outlined in broad strokes. It also states that the revenues from carbon pricing will be used to finance the redemption of GX Economic Transition Bonds, but does not indicate the scale of the specific mechanism or the timing of its introduction.

In general, policy measures can be divided into two categories: "carrot" and "stick". In this case, carbon pricing is the stick and the GX Economic Transition Bonds is the carrot. It could be said that the GX Transitional Bonds are a good combination of both, but the specifics of the policy have not yet been finalized, so it is difficult to praise them without giving them credit. I have been involved in renewable energy policies, including the design of the Renewable Portfolio Standard (RPS), which mandates the introduction ratio of renewable energy sources, and the Feed-in-Tariff (FIT) system for renewable electricity, and I am keenly aware of the importance of the details of the system. As the saying goes, "God is in the details," and it is important to point out that specific policy details are crucial in dealing with issues that involve many stakeholders in complex ways.

Conclusion

Global warming is a global issue that should be tackled by the entire human race over the long term, on the order of 100 years. In order to create a sustainable future, we must not only address the global warming issue, but also balance the 17 goals of the UN SDGs and the 3Es (energy security, economic efficiency, and environmental compatibility), which are the basic goals of Japan's energy policy.

As outlined in this paper, a scenario for solving the global warming problem can be envisioned if the baseline of CO_2 emissions is lowered through social innovation toward the achievement of the SDGs, and a system for producing and efficiently using clean secondary energy such as electricity and hydrogen without CO_2 emissions is built through technological innovation.

* This article has been translated by Readout Editorial Office.

2022 Masao Horiba Awards Award Details

About Masao Horiba Awards

The Masao Horiba Award was established in 2003, to support scientists and experts who are devoting themselves to research and development that will generate innovative technology in analysis and measurement. It also aims to strengthen the position of measurement technologies within the scientific and industrial world. The field for the award is decided each year with a focus on the principles and fundamental technologies fostered by HORIBA, and the award highlights unique research and development with the findings and potential that deserves a global recognition.

Eligible fields

Analytical and measurement technologies that contribute to the use of hydrogen for a decarbonized society

Screening Committee

- Chairperson

YAMAJI Kenji
President, Research Institute of Innovative Technology for the Earth (RITE),
Professor Emeritus, The University of Tokyo Green Innovation Strategy Meeting

- Judges

Scott SAMUELSEN
Professor
Mechanical and Aerospace Engineering, University of California, Irvine

ISHITANI Osamu
Professor
School of Science, Chemistry, Tokyo Institute of Technology
Specially Appointed Professor, Department of Chemistry, Graduate School of Advanced Science and Engineering, Hiroshima University

ISHIHARA Tatsumi
Professor
Deputy Director, International Institute for Carbon Neutral Energy, Kyushu University
Principal Professor, Department of Applied Chemistry, Faculty of Engineering
Department of Bioengineering, Kyushu University

SATOKAWA Shigeo
Professor
Faculty of Science and Technology, Seikei University

MIZUNO Yusuke
Department Manager, Alternative Energy Conversion Department,
Business Incubation Division, HORIBA, Ltd.

HANAKI Yasunari
Manager, New Energy Technology, Alternative Energy Conversion Center,
Business Incubation Division, HORIBA, Ltd.

Masao Horiba Awards Winners

Dr. SATO Katsutoshi

Designated Associate Professor
Department of Chemical Systems, Graduate School of Engineering,
Nagoya University

[Research Theme]

Design of Novel Catalytic Nitrogen Reduction Sites Based on Atomic-Resolution Electron Microscopic Analysis

Dr. TAKAHASHI Yasufumi

Professor,
Department of Electronics, Graduate School of Engineering,
Nagoya University

[Research Theme]

Development of the Electrochemical Imaging Technology for Visualizing Catalytic Active Site

Dr. NAKAMURA Takashi

Associate Professor
Institute of Multidisciplinary Research for Advanced Materials,
Tohoku University

[Research Theme]

Development of Electrochemical Techniques for Defect Engineering on Advanced Energy Materials

Honorable Mention Winner

Dr. TAKAHASHI Yukina

Associate Professor
International Institute for Carbon-Neutral Energy Research (I^2CNER),
Kyushu University

[Research Theme]

Development of a Highly Efficient Hydrogen Generation System by Plasmon-Induced Charge Separation Using Sunlight as an Energy Source

Dr. Helge Sören STEIN

Tenure Track Professor,
Institute for Physical Chemistry (IPC) & Helmholtz Institute Ulm (HIU),
Karlsruhe Institute of Technology (KIT)

[Research Theme]

Data Driven Acceleration of Materials Discovery Through Integrated Correlative Spectroscopy, Synthesis, and Experimentation

* Editorial note: This content in based on HORIBA's investigation at the time of the award unless otherwise stated.

Design of Novel Catalytic Nitrogen Reduction Sites Based on Atomic-Resolution Electron Microscopic Analysis

SATO Katsutoshi

Understanding the structure and chemical state of the active sites is important for the development of highly active catalysts. However, it is difficult to conduct the necessary analyses without exposing reduced catalyst to air, which can alter its structure. We have developed a means of loading reduced catalysts into analytical instruments, such as transmission electron microscopes and various spectroscopic detectors, that avoids exposing the catalyst to the air. Using our non-air-exposure analysis technique, we were able to investigate the nitrogen reduction sites of novel ammonia synthesis catalysts and elucidate the synergistic mechanisms between the catalysts' structures and chemical states. These analyses ultimately allowed us to develop catalysts with high activities at the low temperatures needed for ammonia synthesis using renewable energy. We expect that our non-air-exposure analysis technique will become an important tool for the development of novel catalytic reaction processes, particularly those related to the use of ammonia as a hydrogen carrier, which is an important milestone for establishment of a carbon-neutral society.

Introduction

Design of active sites is essential for the development of highly active catalysts. X-ray diffraction, X-ray absorption spectroscopy, infrared spectroscopy, and Raman spectroscopy are powerful tools for the characterization of heterogeneous catalysts; however, these techniques cannot directly capture the structure and characteristics of the active site because they provide only average information. Transmission electron microscopy (TEM) has the advantage of position-selective observation of targets; however, in the study of supported catalysts, where the size of the active site is below the nanoscale and the structure is too disordered, electron microscopy has traditionally played only a supplementary role for observing morphology and measuring particle size. In recent years, technological innovations such as increased resolution by using spherical aberration correctors and the ability to conduct highly sensitive elemental analyses by using large-area energy-dispersive X-ray fluorescence (EDX) detectors have greatly improved what can be achieved with TEM. Adding to these innovations, we have developed a

sample-loading technique that allows simultaneous observation of the structure and chemical state of the active sites of heterogeneous supported metal catalysts at the atomic-level.

Recently, hydrogen carriers have attracted attention as means of storing and transporting renewable energy. One such hydrogen carrier is ammonia, because of its high energy density (12.8 GJ m^{-3}), high hydrogen content (17.6 wt%), ease of liquefaction and suitability for storage and transportation, and the fact that it can be used to produce hydrogen without emission of CO_2.[1] Ammonia is produced industrially via the Haber-Bosch process using double-promoted iron catalysts. However, the currently available catalysts are all optimized for large-scale processes operating at high temperatures and pressures, meaning their performances are insufficient for processes that are powered by renewable energy and conducted under much milder conditions. Thus, to address the need for novel ammonia synthesis catalysts, we used our non-air-exposure analysis technique to conduct analyses and develop several catalysts with ammonia synthesis activities superior to those of conventional catalysts. Here, we discuss our sample-loading technique and the development of our improved catalysts.

Outline of our sample-loading technique

In heterogeneous catalysts, active sites are usually formed on the catalyst surface during activation (reduction). However, when these active sites are exposed to air, their structure and chemical state are changed by reaction with atmospheric oxygen and water vapor. For example, Ce^{4+} is reduced to Ce^{3+} under high-temperature, reductive conditions, but Ce^{3+} is extremely sensitive to oxygen and is easily oxidized back to Ce^{4+} upon contact with air. Therefore, the state of the active site cannot be analyzed by TEM by using the usual sample preparation method of grinding and grid preparation in air.

To address this issue, we developed an approach that uses a glove box and special airtight sample holder to prevent the catalyst from being exposed to the air (Figure 1). In brief, after activation (reduction), the catalyst is moved to a glove box filled with an inert gas. Once inside the glove box, the catalyst is placed within the airtight receptacle of a special sample holder. The sample holder is then removed from the glove box and loaded into the TEM instrument. This operation allows the activated catalyst to be introduced into the optical tube of the TEM instrument without exposing it to air, and to be observed and analyzed while maintaining its surface structure and state after reduction.

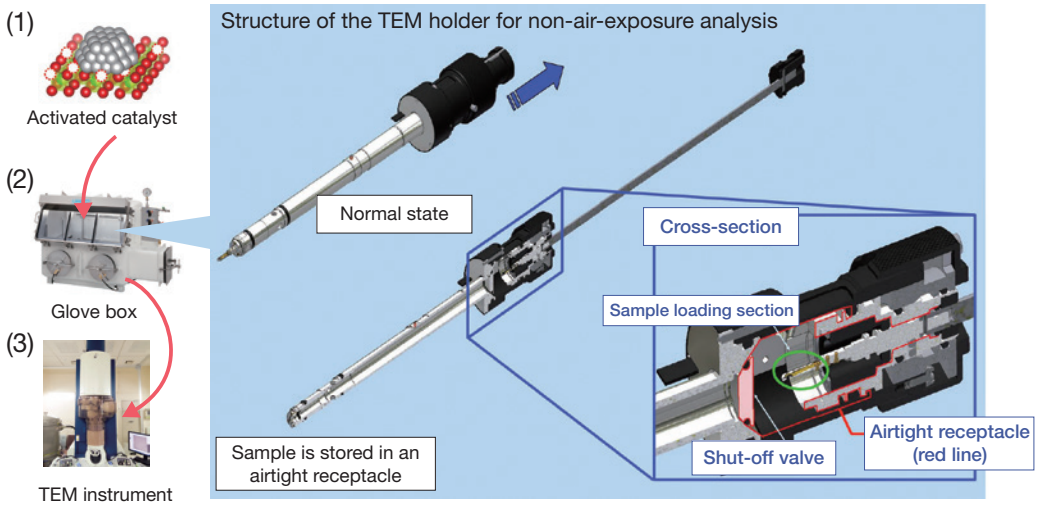

Figure 1 Overview of the sample-loading technique and a schematic showing the structure of the sample holder.
(1) The catalyst is activated (reduced) and then moved to a glove box filled with an inert gas.
(2) The catalyst is then placed within the airtight receptacle of a special sample holder.
(3) The sample holder is then removed from the glove box and inserted into the transmission electron microscope for analysis.

Example application: Supported Ru catalysts

Under mild conditions, supported ruthenium (Ru) catalysts show higher ammonia synthesis activity than the usual double-promoted iron catalysts.[1-3] We developed a cerium-lanthanum composite oxide supported Ru catalyst ($Ru/La_{0.5}Ce_{0.5}O_{1.75}$) and found that this catalyst exhibited better activity than conventional supported Ru catalysts; this higher activity was achieved by reducing the catalyst at 650°C, which is a much higher temperature than that used for the reduction of conventional ammonia-synthesis catalysts such as $Ru/Cs^{+}/MgO$ and Ru/CeO_2.[4]

Using our non-air-exposure analysis technique, we were able to observe the elemental composition of the surface of the $Ru/La_{0.5}Ce_{0.5}O_{1.75}$ catalyst by using an EDX detector and to examine the electronic state of Ce by using an electron-energy-loss spectroscopy (EELS) detector (Figure 2). EELS analysis revealed that Ce^{3+} was more abundant near the surface of the support (Figure 2c). In addition, detailed analysis of the interface between the Ru nanoparticles and the / $/La_{0.5}Ce_{0.5}O_{1.75}$ support revealed that it was Ce^{+3} rich (Figure 2d, e). The rate-determining step in ammonia synthesis is dissociation of the N_2 molecule. To promote this dissociation, electrons can be donated to N_2 molecules adsorbed on the catalyst surface. Our analysis indicated that Ru adjacent to Ce^{3+} was a strong nitrogen reduction site because Ce^{3+} is in a more electron-rich state than is Ce^{4+}.

From our study of the Ru/ $La_{0.5}Ce_{0.5}O_{1.75}$ catalyst, we formulated a guiding principle for catalyst preparation, which is that reduction at high temperature induces the dynamics of the support and produces an active site at the interface with Ru. Following this guiding principle, we prepared a barium (Ba)-doped $La_{0.5}Ce_{0.5}O_{1.75}$ support, loaded it with Ru, and subjected it to high-temperature reduction, which afforded a $Ru/Ba/LaCeO_x$ catalyst with world-class ammonia synthesis performance.[5] We then subjected the reduced catalyst to TEM analysis (Figure 3). We found that the majority of the surface of the Ru nanoparticle was covered with nanosized oxides of low crystallinity (nanofractions) (Figure 3a) and that these nanofractions contained Ba, La, Ce^{4+}, and Ce^{+3} (Figure 3b). These elements have strong electron-donating ability; therefore, the Ru atoms adjacent to the nanofractions showed strong ability to donate electrons to nitrogen and high activity for nitrogen reduction. In addition, Ba was found to play a major role in the formation of these unique structures. The surface of the support is destabilized during the high-temperature reduction by forming a composite oxide incorporating Ba^{2+} with a large ionic radius. To reduce their own surface energy, the resulting composite oxides migrate to the surface of the Ru nanoparticles as nanofractions. Like Ce^{3+}, Ba is also extremely sensitive to atmospheric oxygen and water vapor; therefore, our non-air-exposure sample-loading technique proved useful for clarifying the structure and formation of the active site.

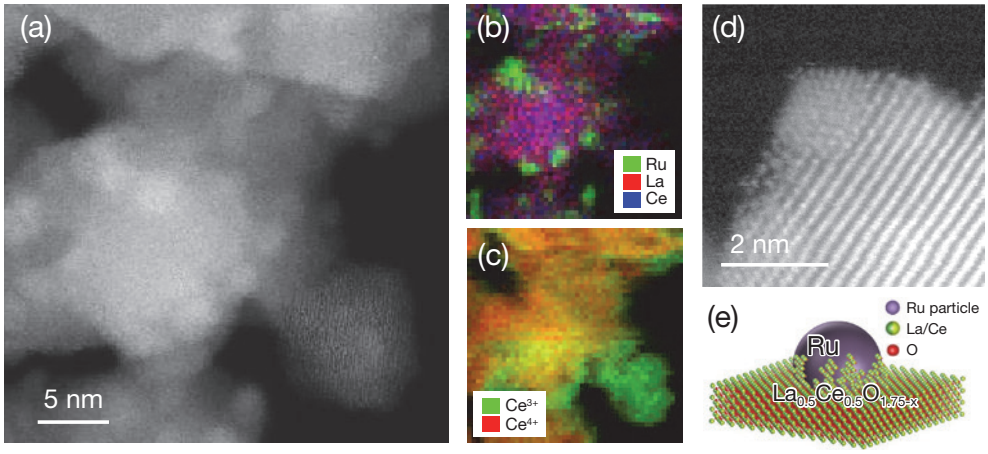

Figure 2 Microscopic analysis of Ru/ $La_{0.5}Ce_{0.5}O_{1.75}$ without exposure to air.
(a) High-angle annular dark-field (HAADF) image. (b) Elemental map of the catalyst, as determined by energy-dispersive X-ray fluorescence analysis. (c) Color map of the valence state of Ce, as determined by electron energy loss spectroscopy. (d) Atomic-resolution HAADF image of an Ru nanoparticle. (e) Schematic illustration of the Ru/L $La_{0.5}Ce_{0.5}O_{1.75}$ surface after reduction.

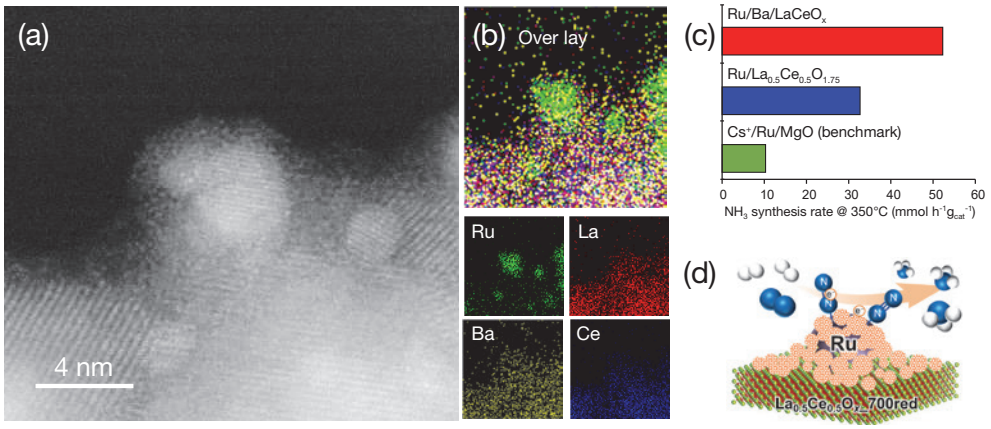

Figure 3 Microscopic analysis of Ru/Ba/LaCeO$_X$ without exposure to air. (a) Atomic-resolution high-angle annular dark-field image of the area around several Ru nanoparticles. (b) Elemental map of the catalyst, as determined by energy-dispersive X-ray fluorescence analysis. (c) Ammonia synthesis activity of Ru/Ba/LaCeO$_x$, Ru/La$_{0.5}$Ce$_{0.5}$O$_{1.75}$, and Cs+/Ru/MgO. Reaction conditions: 1.0 MPa, SV = 72,000 mL h^{-1} gcat^{-1}, N_2/H_2 = 1/3. (d) Schematic illustration of the active site of Ru/Ba/LaCeO$_x$ after reduction.

Example application: Supported non-noble metal (Co) catalysts

We next extended our investigation to supported non-noble metal catalysts and found that Co@BaO/MgO, with magnesium oxide (MgO) as the support, exhibited very good ammonia synthesis activity.[6] Co@BaO/MgO not only achieved higher activity than conventional Co catalysts (250 times higher reaction rate per active site), but also surpassed that of an Ru-based benchmark catalyst (Figure 4). Elemental mapping revealed that the catalyst surface contained a structure comprising Co nanoparticles covered by nanofractions of BaO (Figure 4a). Results of first-principles calculations suggest that formation of this structure promotes dissociation of adsorbed nitrogen as a result of most of the Co nanoparticle surface's becoming electron-rich from electron donation by BaO. Further microscopic analyses revealed the mechanism underlying the formation of the active sites: During high-temperature reduction, Ba species with low melting points are generated and dispersed over the support; Co nanoparticles then collect the Ba species as they are moved across the support by thermal vibrations, resulting in deposition of a BaO nanofraction on the surface of the Co nanoparticles.

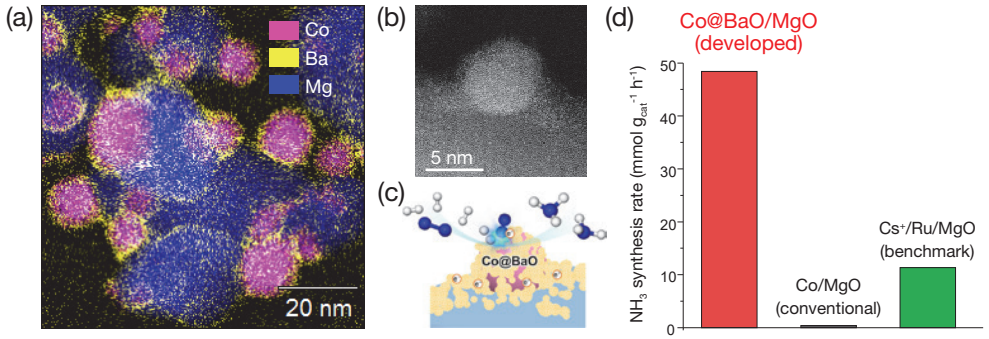

Figure 4 Microscopic analysis of Co@BaO/MgO. (a) Elemental map of the catalyst without exposure to air, as determined by energy-dispersive X-ray fluorescence analysis. (b) Atomic-resolution high-angle annular dark-field image of the area around several Co nanoparticles. (c) Schematic illustration of the surface of Co@BaO/MgO after reduction. (d) Ammonia synthesis activity of Co@BaO/MgO, Co/MgO, and Cs$^+$/Ru/MgO. Reaction condition: 1.0 MPa, SV = 72,000 mL h^{-1} gcat^{-1}, N_2/H_2 = 1/3, 350°C.

Conclusion

Precise design of active sites is important for the development of highly active catalysts. Using our non-air-exposure analysis technique, we successfully developed several highly active catalysts for ammonia synthesis. We expect that our analysis technique will contribute to elucidating further guiding principles for the design of active sites, and to the realization of highly active catalysts for a broad range of reactions.

References

[1] K. Sato, K. Nagaoka, Boosting Ammonia Synthesis under Mild Reaction Conditions by Precise Control of the Basic Oxide-Ru Interface, *Chem. Lett*., 50 (2021) 687-696.

[2] K. Sato, K. Imamura, Y. Kawano, S. Miyahara, T. Yamamoto, S. Matsumura, K. Nagaoka, A low-crystalline ruthenium nano-layer supported on praseodymium oxide as an active catalyst for ammonia synthesis, *Chem. Sci*., 8 (2017) 674-679.

[3] S. Miyahara, K. Sato, Y. Kawano, K. Imamura, Y. Ogura, K. Tsujimaru, K. Nagaoka, Ammonia synthesis over lanthanoid-oxide supported ruthenium catalysts, *Catal. Today*, 376 (2021) 36-40

[4] Y. Ogura, K. Sato, S. Miyahara, Y. Kawano, T. Toriyama, T. Yamamoto, S. Matsumura, S. Hosokawa, K. Nagaoka, Efficient ammonia synthesis over a $Ru/La_{0.5}Ce_{0.5}O_{1.75}$ catalyst pre-reduced at high temperature, *Chem. Sci*., 9 (2018) 2230-2237.

[5] K. Sato, S. Miyahara, Y. Ogura, K. Tsujimaru, Y. Wada, T. Toriyama, T. Yamamoto, S. Matsumura, K. Nagaoka, Surface Dynamics for Creating Highly Active Ru Sites for Ammonia Synthesis: Accumulation of a Low-Crystalline, Oxygen-Deficient Nanofraction, *ACS Sustainable Chem. Eng*., 8 (2020) 2726-2734.

[6] K. Sato, S. Miyahara, K. Tsujimaru, Y. Wada, T. Toriyama, T. Yamamoto, S. Matsumura, K. Inazu, H. Mohri, T. Iwasa, T. Taketsugu, K. Nagaoka, Barium Oxide Encapsulating Cobalt Nanoparticles Supported on Magnesium Oxide: Active Non-Noble Metal Catalysts for Ammonia Synthesis under Mild Reaction Conditions, *ACS Catal*., 11 (2021) 13050-13061.

Dr. SATO Katsutoshi

Designated Associate Professor,
Department of Chemical Systems Engineering,
Graduate School of Engineering,
Nagoya University

Development of the Electrochemical Imaging Technology for Visualizing Catalytic Active Site

TAKAHASHI Yasufumi

To develop high-performance catalysts, it is important to understand the relationship between the micro/nanoscale structures of catalysts and catalytic activity. Catalytic reactions progress in multiple steps, such as diffusion, adsorption, and dissociation of molecules in solution. Therefore, local operando measurement technology in liquid is indispensable for visualizing catalytic active sites. To visualize the catalytic active site, a nanopipette filled with electrolyte is used to form a nanoscale electrochemical cell on the sample by developing scanning electrochemical cell microscopy (SECCM). Using this technique, we visualized the catalytically active sites of MoS_2 nanosheets, which are expected to catalyze the hydrogen evolution reaction.

Introduction

To slow global warming, reducing CO_2 emissions is essential. Among them, electrochemical hydrogen evolution reaction (HER) is one of the key technologies to produce hydrogen known as a clean energy source. Platinum (Pt) is the catalyst that can efficiently generate hydrogen. Since the price of Pt is high, the development of a catalyst to replace Pt is desired.

Two-dimensional (2D) layered transitional metal dichalcogenides[*1], molybdenum disulfide (MoS_2) is one of the most promising precious rare metal-free catalysts for HER.[1] To improve the catalytic activity of MoS_2, significant efforts have been made in terms of conductivity improvement, chemical doping, phase transition, strain, and defect engineering.[2] Quantitatively identifying and characterizing catalytically active sites in MoS_2 are critically important for understanding the catalysis of MoS_2. However, it is still difficult to directly visualize the HER activity site on MoS_2 nanosheets. Therefore, it is necessary to develop a measurement technology to connect the relationship between the spatial distribution and the electrochemical activity of the HER active sites.

As an electrochemical imaging tool, the combination of scanning probe microscopy and microelectrode is effective to sense the surface reactivity of the catalysis with a micrometer scale. Scanning electrochemical microscopy (SECM[*2]) has been demonstrated to be one of the powerful tools for determining the relationship between the surface morphology of a sample and its electrochemical activities for screening highly catalytically active sites in catalytic materials.[3] However, the spatial resolution of

SECM is the issue for characterizing local electrochemical activity because of the difficulty of the miniaturization of the microelectrode. Scanning electrochemical cell microscopy (SECCM), which uses a nanopipette as a probe in a local and movable electrochemical cell, is an effective tool for operando characterization of surface structures electrochemically in a submicron spatial resolution.[4] The advantages of SECCM are that it is a reproducible and reliable technique for fabricating nanoprobes together with fast electrochemical characterization due to its small capacitive current and its ability to prevent sample contamination during scanning.

In this report, the inhomogeneous HER activity on a triangular 1H-MoS_2 monolayer nanosheet, a heterostructures of MoS_2 and WS_2 nanosheets were visualized by using SECCM.[5] Our data provides information about the local catalytic properties as well as electrochemical images of the HER current, Tafel slope, and overpotential by measuring the cyclic voltammograms (CVs) at all measurement points during the imaging. These SECCM measurement unveiled heterogeneous reactivity, relationship of layer number and HER activity, and aging effect.

*1 Transition-metal dichalcogenides (TMDs) are composed of three atomic planes and often two atomic species: a metal and two chalcogens.

*2 SECM uses microelectrode as a probe to detect a oxidation/reduction current on sample surface.

Scanning electrochemical cell microscopy (SECCM)

The SECCM uses a moveable nanopipette probe containing a 0.5 M H_2SO_4 solution and a Pd-H_2 quasi-reference counter electrode (QRCE) (Figure 1a). In the case of chloride ion free solutions, Pd-H_2 QRCE was generally used for SECCM experiments. All the potentials were converted into electric potentials when the reversible hydrogen electrode was used for the reference electrode. The following procedure was used to bring the nanopipette towards the sample surface so that the liquid meniscus just made contact at a series of predefined positions, with an electrochemical measurement at each point. First, the nanopipette (meniscus) was withdrawn from its existing position by a specified distance, typically 0.3 µm. Next, the vertical position of the probe was maintained for 60 ms, while the nanopositioning stage moved the specimen to a new imaging point in the xy plane. Then, the nanopipette was lowered at constant fall rate of 7 nm ms^{-1} while monitoring the current. Immediately after detecting a current (2 pA threshold) by forming the electrical contact between the nanopipette and the sample through the nanopipette meniscus, the approach was stopped and the vertical position of the nanopipette was saved along with the x,y co-ordinate to form a topography map. Local cyclic voltammogram was performed by sweeping the applied voltage (scan rate was set at 130-150 V/s, the measurement time was 20 ms/point) after 0.2 ms wait for suppression of capacitive current. After the electrochemical measurement, the nanopipette was quickly withdrawn by the specified distance to start a new measurement cycle. In this way, simultaneous pictures of topography and redox activity were built up.

HER reactivity mapping on MoS_2 nanosheet

1H-MoS_2 nanosheets were characterized by measuring the cyclic voltammograms (CVs) at all measurement points during the SECCM imaging. CV scan rate was set at 130 V/s, the measurement time was 20 ms/point, and the imaging time (128 × 128 points) was typically 40 min. The current image was obtained by picking up the current signal from CV or applied DC voltage (-1.3 V vs. RHE). An electrode surface area with a radius of 50 nm in the electrochemical cell was used to calculate the current density. The overpotential was evaluated at a 30 mA/cm^2 current density. The CV measurement was done at all of the scanning points, and SECCM provided three electrochemical mapping images of the HER current, Tafel slope, and overpotential, produced simultaneously. SECCM images and a graph of the electrochemical properties of the 1H-MoS_2 nanosheets are shown in Figure 1 (b-d). At the edge region, 1H-MoS_2 nanosheets showed a high current response, a low overpotential, and a low Tafel slope. Notably, it was also observed that there were some activities as a line on the HOPG, which corresponds to the HOPG step edges showing slightly high current responses. In order to characterize the HER catalytic activity of the edge and terrace regions of the 1H-MoS_2 nanosheets, CV curves were selected and averaged from the edge and terrace regions, respectively, shown in Figure 1(e-g). An overpotential with a HER current density at 30 mA/cm^2 and a Tafel slope of 1H-MoS_2 nanosheets edge region, terrace region, and HOPG step are 0.94 V (versus RHE), 1.06 V (versus RHE), and 1.15 V (versus RHE) and 130 mV/dec, 130 mV/dec, and 121 mV/dec, respectively. The relatively larger overpotentials were obtained by the SECCM measurement than typical bulk measurement. In the case of SECCM measurement, the IR drop effect was neglectable because of the small faradaic current. The origin of the overpotentials would be due to the difference of the number of catalytic active sites. These results indicate that the edge region of the 1H-MoS_2 nanosheets show low overpotential but the Tafel slope was not seen remarkble

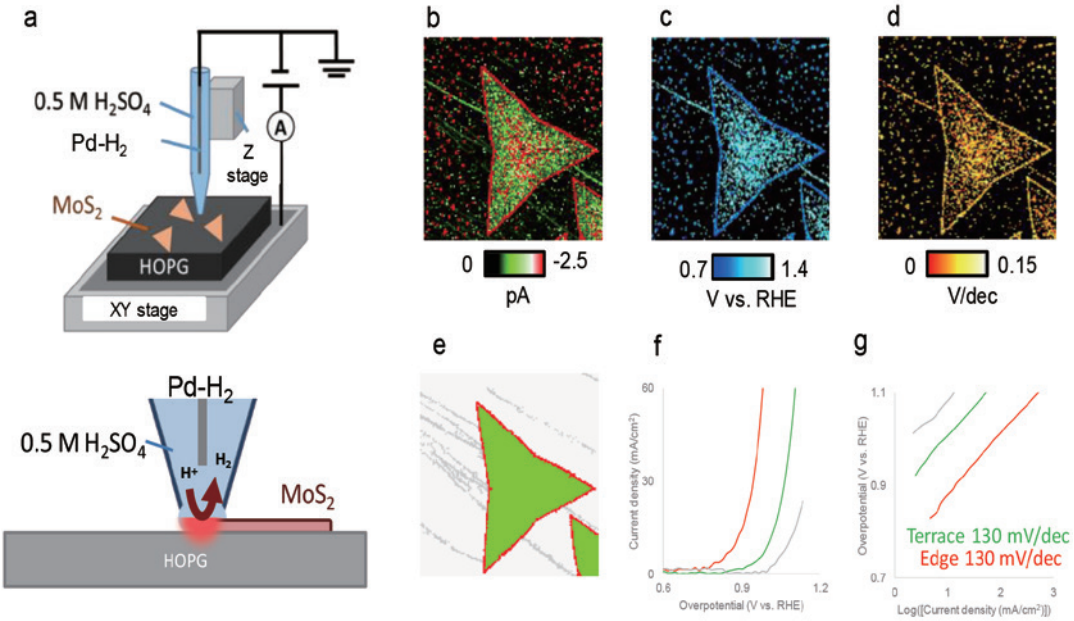

Figure 1 (a) Schematic illustration of SECCM measurements of MoS_2 nanosheets. Pd-H_2 used as a quasi-reference electrode. Nanopipette filled with 0.5 M H_2SO_4. SECCM (b) current, (c) overpotential (30 mA/cm^2), (d) Tafel slope images of 1H MoS_2 nanosheets on HOPG substrate. Scansizes were 15 × 15 μm^2. Scan rate is 130 V/s. Sweep Voltage were -1.3 V vs. RHE. (e) MoS_2 nanosheets edge(red), terrace(green), and HOPG edge(grey) tricolor images. Graphs showing the (f) overpotential and (g) Tafel slope on the 1H MoS_2 edge (red), terrace (green), and HOPG edge(grey) regions.

difference between edge and terrace region for HER catalysis. The current image shows a three highly active lines contrast at the center, which may correspond to grain boundaries or nanowires in the chemical vapor deposition grown 1H-MoS_2 nanosheets, in addition to the highly active edges.

Electrochemical activation of MoS_2 nanosheet for enhance the HER activity

The improvement of the HER activity is an important research target for dichalcogenide catalysts. Frank and coworkers recently reported that the electrochemical generation of sulfur vacancies can improve the HER activity.[6] Briefly, sulfur vacancies generated by applying a negative potential to MoS_2 are more stable than sulfur on the basal plane. At these sulfur vacancies sites, hydrogen adsorption is thermodynamically favoured than sulfur resorption. Therefore, electrochemically generated sulfur vacancies are stable and work as HER catalytic active sites. We have performed similar experiment using SECCM to improve HER activity at a local area on the MoS_2 nanosheets in order to investigate the position-dependent activation properties. The local SECCM CV imaging of a 1H-MoS_2 nanosheet was performed in three different regions with different scan voltages of −1.10, −1.20, and −1.40 V versus RHE to investigate the relationship between the applied voltage and the activation. After electrochemical activation, CV measurements and imaging were performed over a large-scale scanning area to capture a whole 1H-MoS_2 nanosheet in order to characterize the local SECCM activation effects. Figure 2(a-c) shows the electrochemical images of the activated 1H-MoS_2 nanosheet. The electrochemically activated area shows a high current response, a low overpotential, and a low Tafel slope. A high HER activity was observed in the area activated by the scan of up to −1.40 V versus RHE, whereas no significant improvement was observed in the HER activity when the scan was reversed at −1.20 V versus RHE. It was also observed that there was SECCM electrochemical treatment induced homogeneous HER activation in the treated area. These results suggest that the electrochemical activation has a threshold voltage (−1.40 vs. RHE) for improving the HER activity. Defect engineering is also a well-known technique that has been used to improve the HER activity of MoS_2, but its mechanism is unclear. As a demonstration of a defect-engineered sample measurement, we have imaged the HER activity of an over-annealed 1H-MoS_2 nanosheet (300°C in a sulfur atmosphere for 30 min), which had a lot of cracks. Figure 2(d-f) shows the SECCM images of the overannealed 1H-MoS_2 nanosheet. The cracked regions show a low overpotential response and a similar response at their edges. SECCM is also useful for evaluating the treatment effect for improving the catalytic activity of the MoS_2 nanosheet.

HER activity of the MoS_2 - WS_2 heteronanosheet

Atomic-layer semiconducting heterostructures is an important for tuning the band width.[7] However, electrochemical reactivity is closely related to adsorption / dissociation of molecules and electron transfer and Tafel–Volmer reaction is the bottle neck process of HER reaction. To characterize the heterostructures HER activity, we visualized lateral and stacked heterostructure based on MoS_2 and WS_2 heteronanosheet using SECCM and conformed nanosheet topography using AFM (Figure 3(a,b)). The mono or bilayer level lateral and stacked MoS_2 and WS_2 heteronanosheet structure was clearly visualized by AFM. Specific catalytic ability was not observed at the heterojunction, but different current signal was obtained on MoS_2 and WS_2 heteronanosheet (Figure 3(c)). To investigate the detail of HER activity difference, we performed high magnification SECCM imaging. The current response is corresponding with the region and clearly categorize the current response of MoS_2 edge (green), WS_2 terrace(red), MoS_2 terrace(blue), and kish graphite terrace(grey).

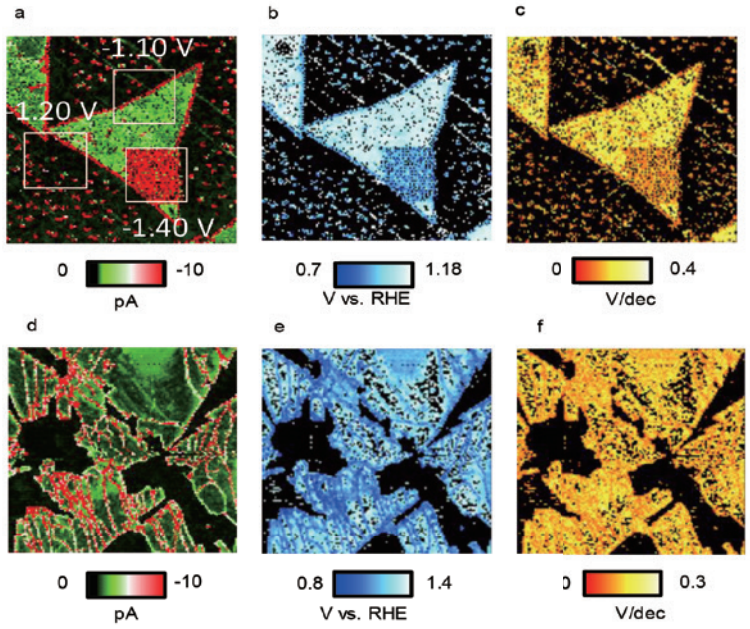

Figure 2 (a) current (b) overpotential (30 mA/cm^2) and (c) tafel slope images of electrochemical activation and imaging of 1H MoS_2 nanosheets on HOPG substrate. Scansize was 10 × 10 mm^2 and -1.2 V vs. RHE. (d) current (e) overpotential (30 mA/cm^2) and (f) tafel slope images of heating activated 1H MoS_2 nanosheets on HOPG substrate. Scansize was 10 × 10 mm^2. -1.1 V vs. RHE.

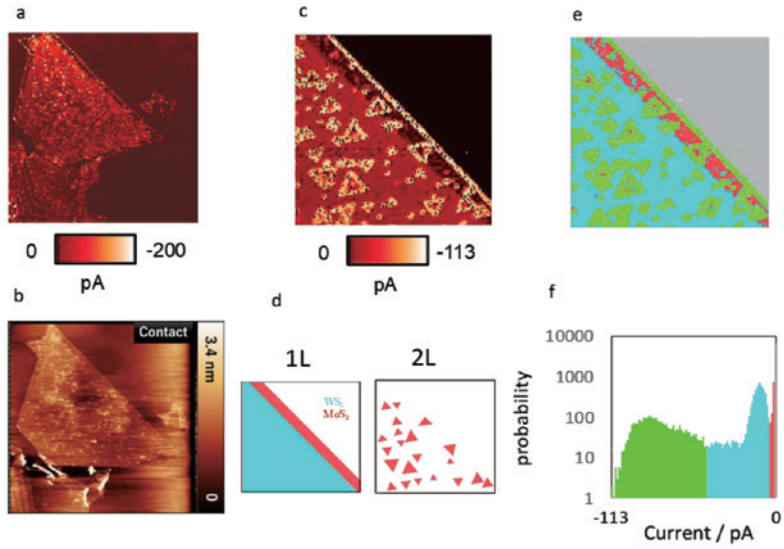

Figure 3 (a) SECCM and (b) AFM images of MoS_2 and WS_2 heteronanosheet on kish graphite. Scansizes were 20 × 20 mm^2 and 18 × 18 mm^2. Applied voltage was -1.0 V vs. RHE. (c) High magnification SECCM, (d) Schematic illustration, and (e) Four color of MoS_2 and WS_2 heteronanosheet image divided based on current and (f) Data from the SECCM images current plotted as histograms. Scansize was 5 × 5 mm^2 and -1.1 V vs. RHE.

Characterization of the Layer number related HER activity

The layer number is also reported as an important factor for HER activity because of the electron conductivity related with layer number.[8] Therefore, as a next experiment, we characterized the relation of layer number and HER activity. Figure 4(a) shows the multi layered MoS_2 and WS_2 heteronanosheet. To investigate the layer dependent HER activity, we categorized the 1st (red), 2nd(green), and 3rd (grey) layer and characterize the overpotential and Tafel slope. Surprisingly, we could not see clear difference of overpotential (30 mA/cm^2) and Tafel slope, 0.91 vs. RHE. and 185 mV/dec, at each layer number. (Figure 4 (d, e)). SECCM local electrochemical imaging is important to directly visualizing and characterizing the local catalytic activity without being buried in the average response.

Characterization of local aging phenomena

Understanding the aging phenomena is very important to use the catalytic material for long time. Nikhil and coworkers reported the aging effect of MoS_2 and WS_2 nanosheets by photoluminescence and XPS.[9] They have reported that the origin of the aging of MoS_2 was due to oxidation process of the transition metals at the edge parts and adsorption of organic contaminants. However, these methods are difficult to characterize the catalytic activity. SECCM can directly visualize the aging effect on transition metal dichalcogenide nanosheet. We characterized HER activity of fresh and partially degraded following room-temperature storage in air for 11 month after the initial synthesis MoS_2 and WS_2 heteronanosheet. The fresh sample shows high activity at the edge. In the case of the pyramid and spiral shape structure WS_2 nanosheets, top regions showed significantly high HER activity (Figure 5(a, b)). On the other hand, edge region of aging sample showed lower current signal compared to terrace region (Figure 5(c)). We also characterize the sample using CV mode SECCM for characterizing overpotential and Tafel slope (Figure 5(d)). The overpotential (30 mA/cm^2) of edge region (0.91 vs. RHE) was higher than terrace region (0.88 vs. RHE). About the Tafel slow, we could not see significant difference between edge and terrace of MoS_2 and WS_2 heteronanosheet. The degradation of MoS_2 and WS_2 heteronanosheet may be expected to derive from the reaction with oxygen, water, and adsorbed organic contamination. These result mean that characterization of progress of the heterogeneous degradation of HER activity is also important application of SECCM.

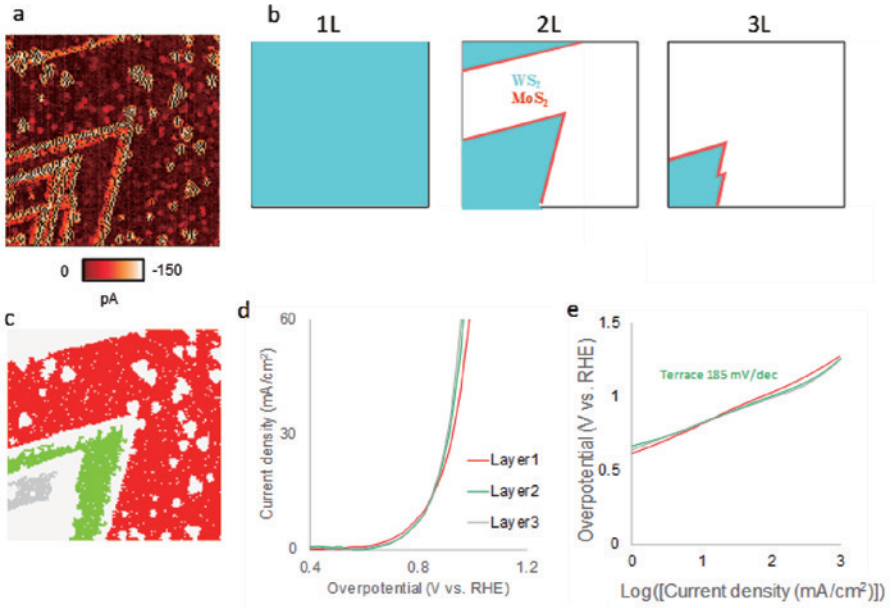

Figure 4 (a) SECCM and (b) Schematic illustration and (c) tricolor images of 1st (red), 2nd (green), 3rd (grey) of MoS_2 and WS_2 heteronanosheet on kish graphite. Scansize was 6 × 6 mm^2 and -1.0 V vs. RHE. Graphs showing the (d) overpotential and (e) Tafel slope of the 1st (red), 2nd (green), 3rd (grey) regions.

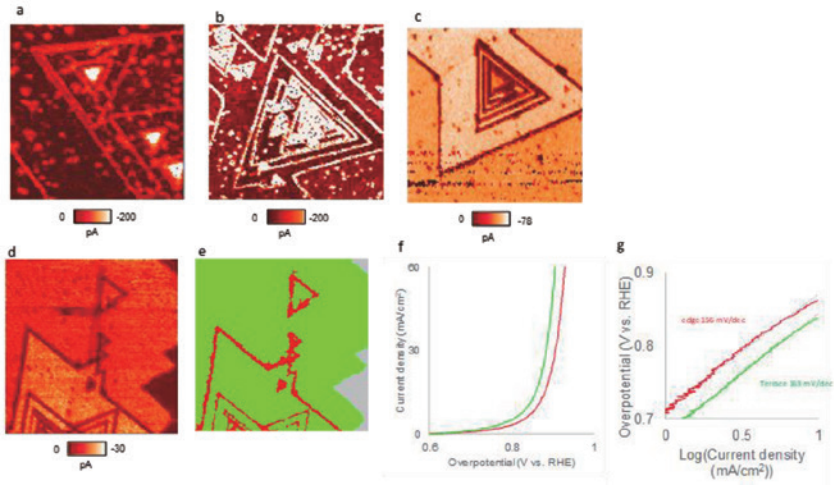

Figure 5 SECCM images of (a, b) fresh and (c) aging MoS_2 and WS_2 heteronanosheet on kish graphite. Scansize were (a) 8 × 8 mm^2 and (b-e)10 × 10 mm^2, respectively. Applied voltage were -0.4 V vs. RHE and -0.9 V vs. RHE, respectively. SECCM (d) current imaging of the aging MoS_2 and WS_2 heteronanosheet and (e) tricolor images of edge (red), terrace (green), and HOPG terrace. Scansize was 7 × 7 mm^2 and -0.4 V vs. RHE and -0.9 V vs. RHE. Graphs showing the (f) overpotential and (g) Tafel slope of the aging MoS_2 and WS_2 heteronanosheet edge (red) and terrace (green) regions.

Conclusion

We have developed SECCM for visualizing HER catalytically active sites in real-space on MoS_2 nanosheets by measuring the distributions of the current, overpotential, and Tafel slope with a submicroscale spatial resolution. The visualization of the HER active sites provides solid experimental evidence to support the previous theoretical prediction and assumption that there is an inhomogeneous catalytic activity between the edges and terraces of 1H-MoS_2 nanosheets. Moreover, the high spatial resolution of SECCM reveals an inhomogeneous HER activity from grain boundarys, small nanosheets, and electrochemically activated regions, which indicates that the HER catalysis of MoS_2 nanosheets may be improved by structure engineering. This study also demonstrates that SECCM is a powerful tool for evaluating the local HER activity for designing the suitable catalytic active structure, phase and can be widely applied for the characterization of 2D catalytic materials.

References

[1] Jaramillo, T. F.; Jorgensen, K. P.; Bonde, J.; Nielsen, J. H.; Horch, S.; Chorkendorff, I. Identification of active edge sites for electrochemical H_2 evolution from MoS_2 nanocatalysts. *Science* **2007**, *317* (5834), 100-102. DOI: 10.1126/science.1141483.

[2] Li, H.; Tsai, C.; Koh, A. L.; Cai, L. L.; Contryman, A. W.; Fragapane, A. H.; Zhao, J. H.; Han, H. S.; Manoharan, H. C.; Abild-Pedersen, F.; et al. Activating and optimizing MoS_2 basal planes for hydrogen evolution through the formation of strained sulphur vacancies (vol 15, pg 48, 2016). *Nat Mater* **2016**, *15* (3). DOI: 10.1038/NMAT4564.

[3] Fernandez, J. L.; Walsh, D. A.; Bard, A. J. Thermodynamic guidelines for the design of bimetallic catalysts for oxygen electroreduction and rapid screening by scanning electrochemical microscopy. M-Co (M : Pd, Ag, Au). *Journal of the American Chemical Society* **2005**, *127* (1), 357-365. DOI: 10.1021/ja0449729.

[4] Takahashi, Y.; Kumatani, A.; Munakata, H.; Inomata, H.; Ito, K.; Ino, K.; Shiku, H.; Unwin, P. R.; Korchev, Y. E.; Kanamura, K.; et al. Nanoscale visualization of redox activity at lithium-ion battery cathodes. *Nature communications* **2014**, *5*, 5450. DOI: Artn 5450
Doi 10.1038/Ncomms6450.

[5] Takahashi, Y.; Kobayashi, Y.; Wang, Z.; Ito, Y.; Ota, M.; Ida, H.; Kumatani, A.; Miyazawa, K.; Fujita, T.; Shiku, H.; et al. High-Resolution Electrochemical Mapping of the Hydrogen Evolution Reaction on Transition-Metal Dichalcogenide Nanosheets. *Angewandte Chemie* **2020**, *59* (9), 3601-3608. DOI: 10.1002/anie.201912863 From NLM PubMed-not-MEDLINE.

[6] Tsai, C.; Li, H.; Park, S.; Park, J.; Han, H. S.; Norskov, J. K.; Zheng, X.; Abild-Pedersen, F. Electrochemical generation of sulfur vacancies in the basal plane of MoS_2 for hydrogen evolution. *Nature communications* **2017**, *8*, 15113. DOI: 10.1038/ncomms15113.

[7] Kobayashi, Y.; Yoshida, S.; Maruyama, M.; Mogi, H.; Murase, K.; Maniwa, Y.; Takeuchi, O.; Okada, S.; Shigekawa, H.; Miyata, Y. Continuous Heteroepitaxy of Two-Dimensional Heterostructures Based on Layered Chalcogenides. *Acs Nano* **2019**, *13* (7), 7527-7535. DOI: 10.1021/acsnano.8b07991.

[8] Yu, Y. F.; Huang, S. Y.; Li, Y. P.; Steinmann, S. N.; Yang, W. T.; Cao, L. Y. Layer-Dependent Electrocatalysis of MoS_2 for Hydrogen Evolution. *Nano Lett* **2014**, *14* (2), 553-558. DOI: 10.1021/nl403620g.

[9] Gao, J.; Li, B.; Tan, J.; Chow, P.; Lu, T.-M.; Koratkar, N. Aging of Transition Metal Dichalcogenide Monolayers. *Acs Nano* **2016**, *10* (2), 2628-2635. DOI: 10.1021/acsnano.5b07677.

[10] Chen, L.; Liu, B. L.; Abbas, A. N.; Ma, Y. Q.; Fang, X.; Liu, Y. H.; Zhou, C. W. Screw-Dislocation-Driven Growth of Two-Dimensional Few-Layer and Pyramid-like WSe_2 by Sulfur-Assisted Chemical Vapor Deposition. *Acs Nano* **2014**, *8* (11), 11543-11551. DOI: 10.1021/nn504775t.

[11] Fan, X. P.; Jiang, Y.; Zhuang, X. J.; Liu, H. J.; Xu, T.; Zheng, W. H.; Fan, P.; Li, H. L.; Wu, X. P.; Zhu, X. L.; et al. Broken Symmetry Induced Strong Nonlinear Optical Effects in Spiral WS_2 Nanosheets. *Acs Nano* **2017**, *11* (5), 4892-4898. DOI: 10.1021/acsnano.7b01457.

Dr. TAKAHASHI Yasufumi

Professor,
Department of Electronics,
Graduate School of Engineering,
Nagoya University

Development of Electrochemical Techniques for Defect Engineering on Advanced Energy Materials

NAKAMURA Takashi

Highly efficient energy storage/conversion devices such as fuel cells and advanced batteries are expected as key technologies for carbon-neutral and sustainable society by utilizing clean hydrogen. In energy functional materials for above-mentioned applications, defects like oxygen vacancy play an important role for their material functionalities. Therefore, understanding true properties of defect is essentially important for defect engineering. The author has been working on the establishment of electrochemical techniques which enable direct evaluation on defect functionality. Furthermore, we have been developing defect control technologies. In this paper, some examples of defect engineering on catalysts and battery materials are given.

Introduction

For the realization of carbon-neutral and sustainable society, efficient utilization of renewable energy is essential. For that, advancing energy conversion/storage technologies such as hydrogen production, rechargeable batteries, electrolysis and fuel cells are important. Cation doping is the most common and effective strategy to advance functionalities of the component of above-mentioned energy conversion/storage devices. However, cation doping is becoming less effective since it has been widely examined so far. For further development of energy functional materials, we focus on the utilization of defects which inherently exist in the materials and play an important role for catalytic, electric and electrochemical properties. It is important to understand decisive factors for the functionalities and establish rational guidelines for defect engineering based on fundamental sciences. Moreover, developing defect control technology is also important goal of our work to exceed the present limit of the material exploration. For the first topic, we have been working on the development of functional energy materials which inherently contain electrochemically active point defects such as oxygen vacancy (unoccupied oxygen site) and interstitial oxygen (excess oxygen at cryptographically vacant space), and for the second topic, we advanced the electrochemical cell as a reactor which can flexibly control defect structure in the target material. Impacts and future benefit of the applicant's work is summarized in Figure 1.

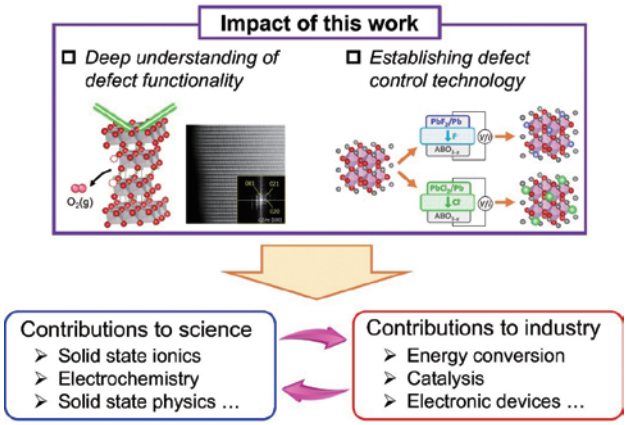

Figure 1 Impacts and future benefits of the present work.

Formation of oxygen defects in layered perovskite oxides $(La,Sr)_2NiO_{4+\delta}$

Perovskite-related oxides are regarded as promising water splitting catalysts and electrode materials for fuel cells.[1-3] Their catalytic properties are strongly influenced by oxygen defects such as oxygen vacancy and interstitial oxygen, and therefore, understanding the mechanism of oxygen defect formation is essentially important. Here, to investigate oxygen defect formation in layered perovskite oxides $(La,Sr)_2NiO_{4+\delta}$ (Figure 2-a), we applied two experimental techniques. One was the thermogravimetry (TG) which can evaluate oxygen content variation by detecting the weight change due to oxygen defect formation, Δw_s, and the other was coulometric titration (CT) which can evaluate oxygen content and equilibrium oxygen chemical potential by using the electrochemical cell composed of an oxide-ion conductor. For TG, very accurate symmetrical balance is installed into glass/ceramics chamber where temperature and atmospheric condition are controlled by a heater and gas-mixtures (Figure 2-b). Variation of oxygen content can be evaluated from the weight change by

$$\Delta\delta = \frac{M_s}{M_O}\frac{\Delta w_s}{w_s} \qquad (1)$$

where $\Delta\delta$, M_s, M_O, and w_s are the relative variation of oxygen nonstoichiometry, the formula weight of the sample and oxygen atom, and the weight of the specimen, respectively. Controllable $P(O_2)$ range by O_2-Ar gas-mixtures is 10^{-4} to 1 bar. This is not enough to evaluate the oxygen defect formation in $(La,Sr)_2NiO_{4+\delta}$.

During the CT measurement, the amount of oxygen in the specimen was controlled by the electric charge passed through the cell. After a specified amount of electric charge was passed, $\Delta\delta$ was calculated by the equation

$$\Delta\delta = \frac{C}{2FM_s} \qquad (2)$$

where C and F is the total amount of electric charge and the Faraday constant, respectively. Equilibrium oxygen partial pressure, $P(O_2)_{eq}$, corresponding to a certain oxygen content was obtained from the electromotive force between the inside and the outside of the cell, E, under the equilibrium state as

$$P(O_2)_{eq} = P(O_2)_{RE}\exp\left(\frac{4FE}{RT}\right) \qquad (3)$$

where $P(O_2)_{RE}$, R, and T are the oxygen partial pressure at the reference electrode, the gas constant and the temperature, respectively. The oxygen content was determined by the weight change of the sample after reduction decomposition under hydrogen atmosphere.

Figure 2-b, 2-c and 2-d shows the oxygen content variation of $La_2NiO_{4+\delta}$, $La_{1.8}Sr_{0.2}NiO_{4+\delta}$ and $La_{1.6}Sr_{0.4}NiO_{4+\delta}$ as a function of equilibrium oxygen partial pressure.[4] Since both TG and CT were applied complementary in this work, oxygen defect formation under wide $P(O_2)$ range was successfully evaluated. $La_{1.8}Sr_{0.2}NiO_{4+\delta}$ showed representative oxygen content variation behavior of a layered perovskite oxide. In high $P(O_2)$ atmosphere, $La_{1.8}Sr_{0.2}NiO_{4+\delta}$ showed oxygen-excess composition by accepting interstitial oxygen in the rock-salt structure, while it showed oxygen-deficient composition by oxygen vacancy formation in low $P(O_2)$ atmosphere. Plateau-like behavior of the oxygen content against $P(O_2)$ was reasonably observed near the stoichiometric oxygen composition ($4+\delta \sim 4.00$) which is consistent with thermodynamic estimation.[5] Such oxygen defect formation also depends on the acceptor concentration, Sr content in this system. As Sr concentration increases, the oxygen vacancy formation proceeds easier, while the formation of interstitial oxygen needs stronger driving force.

The observed oxygen defect formation mechanism was investigated by defect chemical and thermodynamic analyses. The defect equilibrium model was established from the site conservation, defect equilibrium reactions and charge neutrality under the rigid band approximation with p-type degenerated electronic state

$$P(O_2)^{1/2} = \frac{[O_i'']}{[V_i^{\times}]} \exp\left[\frac{\Delta G_I^{\circ} - a[O_i'']}{RT} + 2\ln\left\{\exp\left(\frac{N_A}{D_{VB}V_m}[h^{\bullet}]\right) - 1\right\}\right] \quad (4\text{-}1)$$

$$[O_i''] = \frac{-(6K_f - \delta + K_f\delta) + \sqrt{(6K_f - \delta + K_f\delta)^2 + 8K_f(1 - K_f)(4 + \delta)}}{2(1 - K_f)} \quad (4\text{-}2)$$

where $[O_i'']$, $[V_i^{\times}]$, $[h^{\bullet}]$, ΔG_I°, ΔG_f°, K_f, a, and D_{VB} are the molar concentration of interstitial oxygen, that of vacant interstitial site, that of hole, the Gibbs free energy change of interstitial oxygen formation, that of oxygen Frenkel formation, the equilibrium constant of oxygen Frenkel defect formation, the regular solution parameter and the density of state of the valence band. The derivation of the above defect equilibrium model is summarized in our work.[4] The calculated δ-T-$P(O_2)$ relation is added in Figures 2-b, 2-c and 2-d. As illustrated, the defect equilibrium model can explain oxygen composition variation with T and $P(O_2)$ very well, meaning that the defect structure under certain T and $P(O_2)$ can be estimated precisely by this model. Such fundamental knowledge about oxygen defect formation is essentially important to design defect structures and maximize the functionalities of oxygen defects.

Lattice oxygen stability in lithium-ion battery cathode materials Li(Ni,Co,Mn)O_2

Transition metal oxides are key components of secondary batteries such as alkali metal-ion and anion batteries, sufficient stability of which is thus vitally important for ensuring high energy density and safety. However, problems attributed to the lattice oxygen instability in transition metal oxide cathodes have been widely reported, such as capacity degradation, gas generation and catastrophic thermal runaway.[6,7] These highlights the importance of insight into decisive factors for lattice oxygen stability. In this section, our recent works on the evaluation of lattice oxygen stability in layered rock-salt Li(Ni,Co,Mn)O_2 are summarized. We succeeded to evaluate the oxygen release behavior

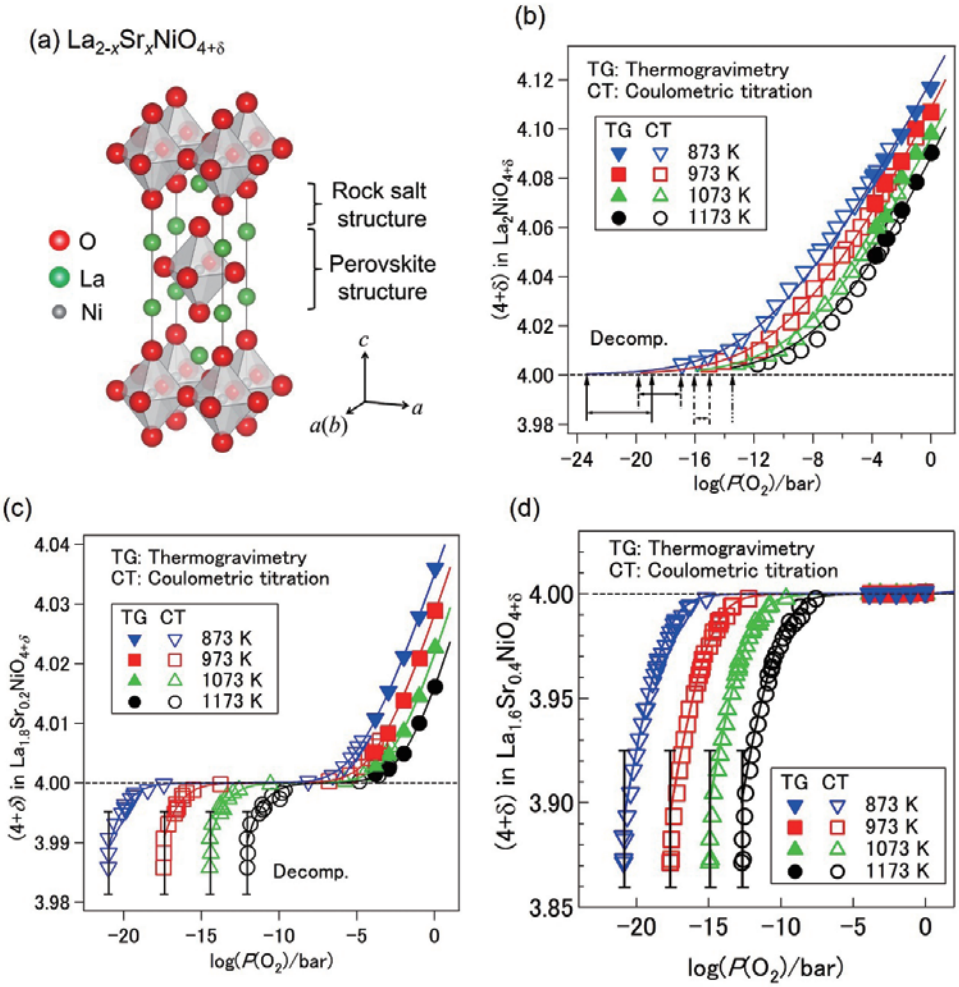

Figure 2 (a) Crystal structure of $(La,Sr)_2NiO_{4+\delta}$. Oxygen content variation (oxygen nonstoichiometry) of (b) $La_2NiO_{4+\delta}$, (c) $La_{1.8}Sr_{0.2}NiO_{4+\delta}$ and (d) $La_{1.6}Sr_{0.4}NiO_{4+\delta}$ as a function of equilibrium oxygen partial pressure. Closed and open symbols were measured by thermogravimetry and by coulometric titration, respectively. Calculated δ-T-$P(O_2)$ relation by the defect equilibrium model (Eq. 4) are shown as solid lines.

of lithium-ion battery cathode by applying the high-temperature solid-state-ionic techniques shown in the previous section, namely TG and CT. Oxygen release behavior and relevant changes in crystal and electronic structures were investigated and analyzed based on defect chemistry and thermodynamics.[8,9]

The molar ratio of oxygen over transition metal, O/TM, against $P(O_2)$ in $LiNi_{1/3}Co_{1/3}Mn_{1/3}O_2$ (NCM111) is summarized in Figure 3-a. In the figure, O/TM = 2 represents the stoichiometric oxygen composition and O/TM < 2 represents the oxygen deficient composition. The oxygen content of the pristine NCM111 was determined by iodometric titration. The oxygen content decreased along with lower equilibrium $P(O_2)$ in the gaseous phase. With totally 4.8 mol% oxygen deficiency introduced in the lattice, NCM111 remained its original layered rock-salt structure without phase transformation or reduction decomposition as confirmed by XRD (Figure 3-b). All XRD profiles of the oxygen-deficient NCM111 were indexed by $R\bar{3}m$, and no impurity peak was observed by oxygen release. However, gradual broadening of diffraction peaks was observed with increasing oxygen deficiency. This indicated the deterioration of crystallinity with oxygen deficiency, despite changes of grain size and morphology was not significant. Diffraction peaks shifted to lower angle with oxygen release, indicating the expansion of the crystal lattice. In addition, the intensity ratio the 003 and 004, I_{003}/I_{104}, declined from 1.36 in the pristine to 0.80 in the 4.8 mol% oxygen-deficient NCM111, indicating disorder of the layered structure by anti-site defect formation (exchange of Li and Ni) as reported in earlier works.[10,11] To investigate the charge compensation mechanism due to oxygen release, oxygen-deficient NCM111 (0.5 mol%, 2.0 mol%, 3.5 mol% and 4.8 mol%) were characterized by X-ray absorption spectroscopy (XAS), and transition metal L-edge spectra are summarized in Figure 3-c, 3-d and 3-e. Probing depth of the fluorescence X-ray mode is typically hundreds nanometers which is close to the size of as-synthesized primary particles, therefore obtained data reflect the bulk information. In Ni L-edge spectra, the intensity of the peak around 855 eV (L_{III} edge) decreases slightly from the pristine to the samples with 0.5 mol% and 2.0 mol% oxygen deficiency, and keep invariant with further oxygen release. These spectral changes suggest that high-valent Ni was reduced to Ni^{2+} until 2.0 mol% oxygen release, and was invariant by further oxygen release. The reduction behavior observed for Ni suggests the existence of small quantity of Ni^{3+} in the pristine sample, which can be explained by negative defects such as cation vacancy or excess Li at the transition metal site (Li''_{TM}). In Co L-edge spectra, there was no observable spectral variation until 0.5 mol% oxygen deficiency, while the shoulder peaks around 778 eV in L_{III} edge appeared with 2.0 mol% oxygen release, indicating that Co was reduced from ca. 0.5 mol% of oxygen loss. The increase of shoulder peaks with oxygen loss suggest that Co acted as the main reduction species when the amount of oxygen loss exceeded 0.5 mol%. The absorption spectra of Mn showed no significant change from the pristine to 4.8 mol% oxygen release, meaning that the contribution of Mn^{4+} reduction is negligibly small in NCM111. From the spectral changes at Ni, Co and Mn L-edge, the charge compensation mechanism due to oxygen release in NCM111 can be explained as follows. In the initial stage of oxygen release only high-valent Ni is selectively reduced followed by the selective reduction of Co^{3+} species, while the reduction of Mn^{4+} is negligible.

As discussed, the charge neutrality was balanced by selective reduction of high-valent Ni in the initial stage of oxygen release in NCM111. This strongly indicates that the presence of high-valence Ni significantly destabilizes lattice oxygen and facilitates oxygen release. To confirm this hypothesis, oxygen release from high Ni concentration NCM series, $LiNi_{0.5}Co_{0.2}Mn_{0.3}O_2$ (NCM 523) and $LiNi_{0.6}Co_{0.2}Mn_{0.2}O_2$ (NCM622), were investigated in a similar manner. Because nominal oxidation state of Ni in NCM111, NCM523 and NCM622 is 2, 2.4 and 2.667, respectively, oxygen release easily proceeds in high Ni NCM. As summarized in Figure 3-f, the δ vs. $P(O_2)$ curve of NCM622 appears in higher $P(O_2)$ region than that of NCM111, while NCM523 shows similar oxygen release behavior to NCM622 except 2-δ < 1.93. These results indicate that lattice oxygen is less stable with increasing Ni valence state and support our hypothesis that high-valent Ni destabilizes lattice oxygen. For more quantitative discussion, partial molar enthalpy of oxygen, $(h_O\text{-}h_O^0)$, was calculated from δ-T-$P(O_2)$ relation which represents necessary energy for oxygen release. Figure 3-g shows $-(h_O\text{-}h_O^0)$ as functions of the amount of released oxygen δ and reduction species during oxygen release; circular symbols show Ni reduction and square symbols show Co reduction. As can be clearly confirmed, $-(h_O\text{-}h_O^0)$, in other words necessary energy for oxygen release, essentially depends on reduction transition metal. Oxygen release with Ni reduction needs less than 0.5 eV, while that with Co reduction needs more than 2.0 eV. It can be concluded that the presence of high valent Ni significantly degrades lattice oxygen stability. As demonstrated in this work, thermodynamic evaluation can pave the way for quantitative and direct discussion on lattice oxygen stability of battery materials. Undoubtedly, transition metal oxides play an important role in the next-generation batteries, including not only

advanced lithium-ion batteries but also multivalent metal-ion batteries and alkali metal-ion batteries. Oxygen release and issues induced by lattice oxygen activity are inevitable problems. We expect the methodology demonstrated in this work will establish guidelines of designing and tailoring advanced energy materials for robust and high-energy-density batteries.

Development of electrochemical reactors for anion defect engineering

Since conventional cation doping strategy is becoming less effective due to wide variety of attempts so far, anion doping gains attention as a new strategy for further advancement of energy functional materials. For efficient utilization of functionalities of anion defects, electrochemical reactors for the control of anion defect species have been developing by the authors' research team. The schematic picture of the reactor and superiorities are summarized in Figure 4. The reactor has some great advantages compared with conventional synthesis techniques such as high-pressure synthesis, mechanical milling, topochemical reaction.[12-14] First, the driving force of the anion defect doping can be controlled by the external voltage according to the Nernst equation. When A^{n-} is controlled by the electrochemical reactor, the chemical potential of the neutral A at the target material μ_A is expressed by the Nernst equation by

$$\mu_A = \mu_{A,CE} + nFE \quad (5)$$

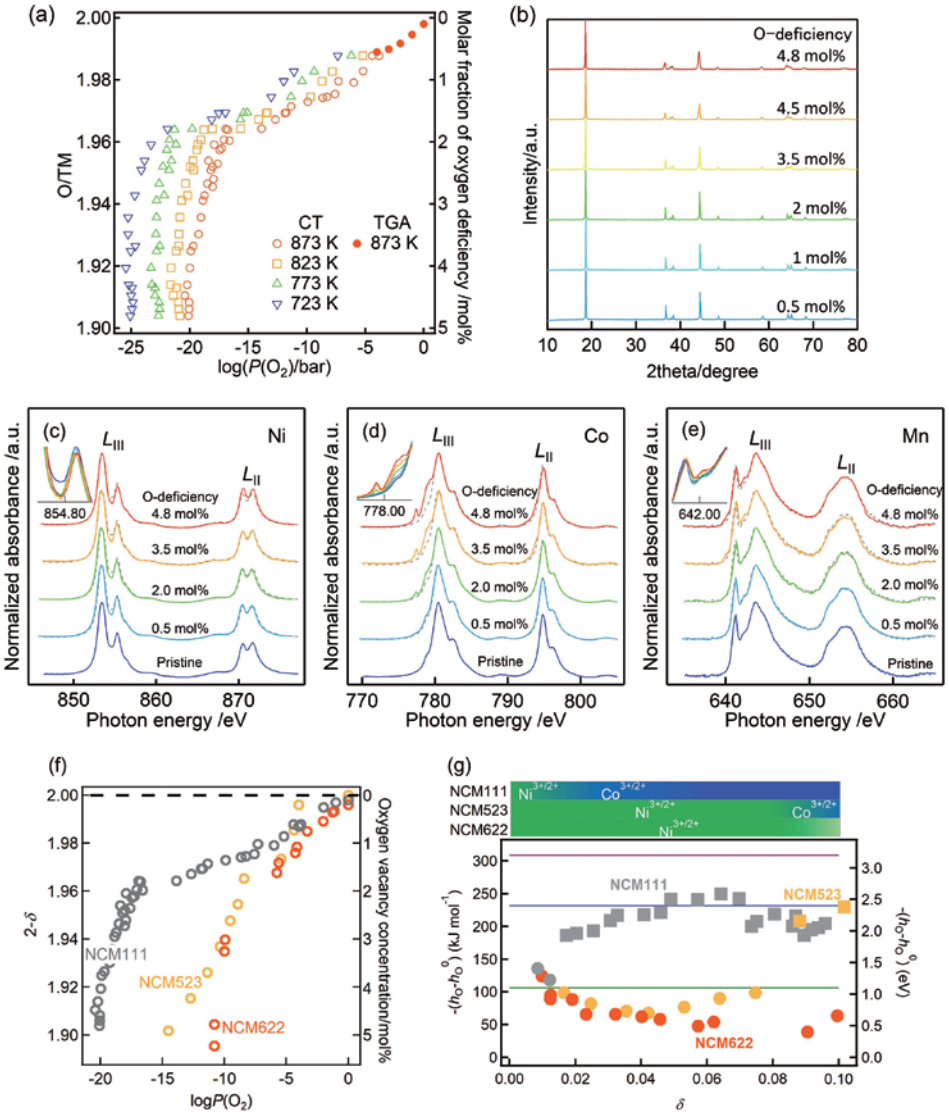

Figure 3 (a) Oxygen release behavior of NCM111 and (b) XRD patterns of oxygen-deficient NCM111. XAS spectra of oxygen-deficient NCM111 at (c) Ni L-, (d) Co L- and (e) Mn L-edge. Oxygen release behavior of NCM111, NCM532 and NCM622 measured at 873 K. (f) $-(h_O-h_O^0)$ as a function of δ. Circular symbols show $-(h_O-h_O^0)$ by Ni reduction and square symbols show that by Co reduction.

where E and $\mu_{A,CE}$ are the electrode potential and the chemical potential of A at the counter electrode, respectively. This means that the reactor can create extremely high activity condition (even impossible condition by conventional techniques) just by applying external voltage. Second, wide variety of anionic defects are controllable by changing the electrolyte. Third, the amount of doped anionic species can be quantitatively controlled by the charge passing through the cell. Considering these advantages, our electrochemical reactor can pave the way to extend the possibility of defect engineering and mixed-anion compounds.

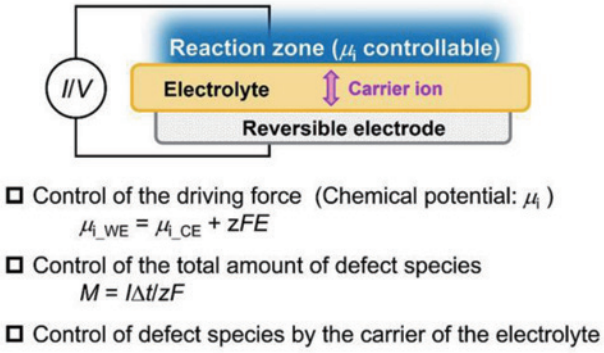

Figure 4 Schematic illustration of the electrochemical reactor for anion defect control.

Conclusions

As a new strategy for further development of energy conversion/storage technologies, we take notice of the utilization of defects in energy functional materials. To achieve this, it is necessary to establish basic sciences regarding defect formation and their functionalities, and to develop a new technology for flexible and easy control of defect species in the target material. As a case study of the first purpose, oxygen defect formation in a layered perovskite oxide $(La,Sr)_2NiO_{4+\delta}$ is summarized, since oxygen defects such as oxygen vacancy and interstitial oxygen play an important role for catalytic activity and electrochemical properties in this material. Oxygen defect formation behavior was investigated, and a defect equilibrium model based on defect chemistry and thermodynamics was proposed. The proposed model agrees very well with observed oxygen content variation with T and $P(O_2)$. Moreover, these experimental and analytical techniques are applied to understand the mechanism of oxygen release from lithium-ion battery cathodes. Although this is an unprecedented challenge in a battery research field, we, for the first time, report fruitful fundamental knowledge of oxygen release. For instance, our work revealed that reduction species (transition metal being reduced during oxygen release) essentially determine the lattice oxygen stability. For the second purpose, we are developing electrochemical reactors composed of an anion conductor which can flexibly, easily and quantitatively control anion defect species in the target material. While the concept of the reactor and schematic illustrations are shown in this paper, some promising results will be shown soon. Complementary advancement of both the establishment of fundamental sciences on defects and the development of defect control techniques is going to contribute to technological innovation of energy functional materials based on defect engineering, and consequently, contribute to the realization of carbon-neutral and sustainable society.

References

[1] A. P. Tarutin, J. G. Lyagaeva, D. A. Medvedev, L. Bi, A. A. Yaremchenko, *J. Mater. Chem. A*, 2021, 9, 154-195.
[2] P. C. Meenu, P. K. Smanta, T. Yoshida, N. J. English, S. P. Datta, S. A. Singh, S. Dinda, C. Chakraborty, S. Roy, *ACS Appl. Energy Mater.*, 2022, 5, 503-515.
[3] H. Li, Y. Chen, J. Ge, X. Liu, A. C. Fisher, M. P. Sherburne, J. W. Ager, Z. J. Xu, *JACS Au*, 2021, 1, 108-115.
[4] T. Nakamura, K. Yashiro, K. Sato, J. Mizusaki, *Solid State Ionics*, 2009, 180, 368-376.
[5] C. Wagner, *Prog. Solid State Chem.* 1971, 6, 1-15.
[6] X. Feng, M. Ouyang, X. Liu, L. Lu, Y. Xia, X. He, *Energy Storage Mater.*, 2018, 10, 246-267.
[7] S. Shrifi-Asl, J. Lu, K. Amine, R. Shahbazian-Yassar, *Adv. Ener. Mater.*, 2019, 9, 1900551.
[8] X. Hou, Y. Kimura, Y. Tamenori, K. Nitta, H. Yamagishi, K. Amezawa, T. Nakamura, *ACS Energy Lett.*, 2022, 7, 1687-1693.
[9] X. Hou, K. Ohta, Y. Kimura, Y. Tamenori, K. Tsuruta, K. Amezawa, T. Nakamura, *Adv. Energy Mater.*, 2021, 11, 2101005.
[10] T. Ohzuku, A. Ueda, M. Nagayama, *J. Electrochem.* Soc., 1993, 140, 1862-1870.
[11] J. Zheng, P. Xu, M. Gu, J. Xiao, N. D. Browning, P. Yan, C. Wang, J. G. Zhang, *Chem. Mater.*, 2015, 27, 1381-1390.
[12] N. Takeda, I. Ikeuchi, R. Natsui, K. Nakura, N. Yabuuchi, *ACS Appl. Energy Mater.*, 2019, 2, 1629-1633.
[13] M. Yang, J. A. Rodgers, L. C. Middler, J. Oró-Sró, A. B. Jorge, A. Fuertes, J. P. Attfield, *Inorg. Chem.*, 2009, 48, 11498-11500.
[14] H. Kageyama, K. Hayashi, K. Maeda, J. P. Attfield, Z. Hiroi, J. M. Rondinelli, K. R. Poeppelmeier, *Nat. Commun.*, 2019, 9, 772.

Dr. NAKAMURA Takashi
Associate Professor,
Institute of Multidisciplinary Research for Advanced Materials,
Tohoku University

Development of a Highly Efficient Hydrogen Generation System by Plasmon-Induced Charge Separation Using Sunlight as an Energy Source

TAKAHASHI Yukina

Although the total amount of sunlight is large, the energy density per unit area is small and the supply is unstable. Therefore, it is important in practical use to devise some means to store and increase the energy density. The localized surface plasmon resonance (LSPR) of metal nanoparticles increases the density of solar energy, and the phenomenon of plasmon-induced charge separation (PICS), which occurs when metal nanoparticles are combined with semiconductors, can be used to convert light energy into electrochemical energy, which can be used to generate hydrogen from solar energy. This paper describes a research plan to develop a highly efficient hydrogen generation system using solar energy.

Introduction

A stable supply of renewable energy that does not rely on fossil resources such as oil and coal is essential to the realization of a sustainable society. Among the energy sources such as solar, wind, hydro, geothermal, tidal, and biomass, which can always be supplied from nature, solar is a particularly promising energy source. This is because the energy is obtained from outside the closed system of the earth, where the law of conservation of energy holds. The sun generates enormous amounts of energy through nuclear fusion. Only a small fraction of that energy reaches the Earth's surface. The energy reaching the surface of the earth and the sea is approximately 3 x 10^{24} J y^{-1}.[1] This value is approximately 5000 times as large as world energy consumption.[2] However, although an enormous amount of light energy falls on the earth in total, it has the disadvantage of having a small energy density per unit area. In addition, since it is dependent on nature, the supply is unstable because it is greatly affected by the seasons and weather, with the exception of some regions such as the Sahara Desert. In other words, it is an important issue in the implementation of the system to store a large amount of energy when it is supplied in large quantities, to downsize the system to produce only the necessary amount in small quantities when needed on site, and to devise ways to increase the energy density. Among them, we are focusing on ways to increase energy density.

Photoenergy harvesting in order to increase the energy density

One of the solutions is by using metal nanoparticles in order to dense the light energy. When metals are nano-sized from several nanometers to a hundred nanometers in diameter, they have the effect of trapping the photoenergy of incident light in the nanospace beyond the diffraction limit of the particle surface (Figure 1). This effect is based on a phenomenon called localized surface plasmon resonance (LSPR), and the resonance wavelength can be controlled from the UV to the near-infrared, depending on the metal species, particle size, shape, aggregation state, and refractive index of the surrounding medium. This property has been applied to sensors using the shift of plasmon peak wavelengths, and is also known to enhance both photoexcitation and emission processes of photoactive materials, such as dyes and quantum dots, on the surface of nanoparticles, which can be used for surface enhanced Raman scattering (SERS),[3] photocurrent enhancement of solar cells,[4-8] and luminescence enhancement of fluorescent dyes.[9] Theoretically, the light energy harvesting effect by LSPR is calculated to be tens to millions of times larger than that of incident light. The light energy harvesting effect of LSPR can overcome the disadvantage of sunlight, which has a low energy density per unit area.

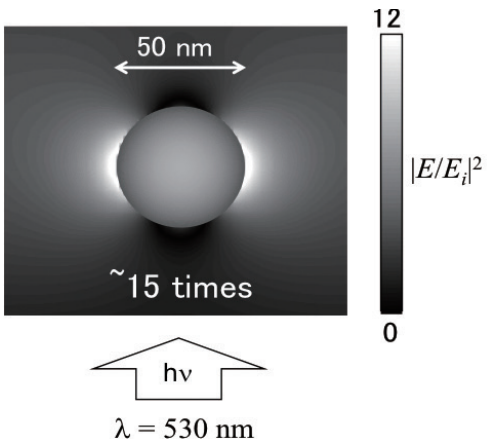

Figure 1 Photo-harvesting effect of a gold nanoparticle with the diameter of 50 nm based on LSPR (calculation).

Photoenergy conversion to other energy

There is also a method of directly utilizing light energy captured by metal nanoparticles without the use of dyes or other means. When plasmonic metal nanoparticles are combined with a semiconductor such as titanium dioxide, electrons in the metal nanoparticles transfer into the conduction band of the semiconductor under light irradiation at resonance wavelengths, a phenomenon called plasmon-induced charge separation (PICS) (Figure 2).[10] This leads to a reduction reaction on the semiconductor and an oxidation reaction on the metal nanoparticles, and is expected to be applied to sensors,[11] photoelectric conversion devices,[10,12] and visible-light-responsive photocatalysts.[10,13] In this system, light irradiation causes charge transfer to proceed directly without the use of dyes. Therefore, energy loss can be eliminated by constructing a simple system, and high conversion efficiency can be expected. This can be used in the hydrogen generation reaction by water reduction and hydrocarbon generation reaction by carbon dioxide reduction to convert light energy into chemical energy that can be stored, thereby overcoming the disadvantages of sunlight, which is unstable in supply.

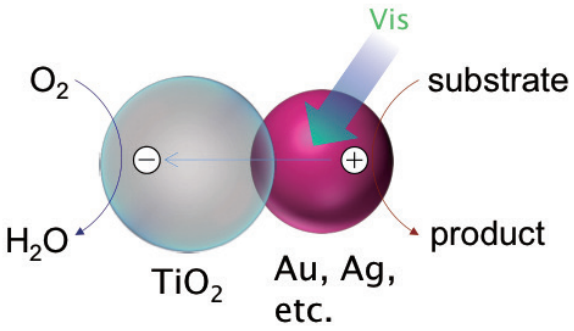

Figure 2 Schematic illustration of the conventional PICS.

Problems with conventional PICS system

However, conventional PICS has several problems due to the use of n-type semiconductors. One is the low stability of metal nanoparticles. Since oxidation reactions occur on the metal nanoparticles, it may cause the metal nanoparticles themselves to dissolve, even silver nanoparticles, which are known to be relatively stable. We have been studied to solve the problem. We succeeded in improving the thermal stability of spherical silver nanoparticles, by introducing an Al_2O_3 nanomask as a template of the nanoparticles, and the chemical stabilities by coating with a thin and dense titanium dioxide film.[14] In same way, by coating with titanium dioxide film, we improved stabilities of gold nanorods,[15] and silver nanoplates,[16] which are effective for the use of near-infrared light due to their shape anisotropy but are easily deformed into a spherical shape. However, the use of cheaper and less unstable metals was desired.

Second is the low efficiency of the charge separation. The photoelectric conversion efficiency (η) of the conventional PICS was approximately 1%.[10] In titanium dioxide photocatalysts, metal nanoparticles supported on the photocatalyst function as an electron pool that suppresses recombination of excited electrons and holes, as evidenced by their use as reduction sites.[17] Therefore, electrons transferred to the semiconductor after charge separation by conventional PICS are likely to undergo reverse electron transfer to the metal nanoparticles (recombination in the broad sense). It was supported by the reports that charge separation lifetime improved from picoseconds to microseconds by changing the semiconductor combined with the metal nanoparticles from n-type to p-type.[18]

Highly efficient hydrogen generation via PICS system with a p-type semiconductor

We therefore propose that the above problem can be solved by using a p-type semiconductor, which reverses the charge transfer, because the reduction reaction can proceed on the metal nanoparticles used in PICS (Figure 3).[19] The catalytic effect of the metal nanoparticles in the reduction reaction can also be expected. As a result, the selectivity of the reaction products can be improved. For example, copper is known to be able to reduce carbon dioxide to C2 compounds such as ethanol and ethylene when used as an electrode in electrochemical reactions.[20] Therefore, it is expected that by controlling the type of metal and crystal planes that make up the nanoparticles, arbitrary chemical reactions can be promoted, such as the generation of hydrogen and the generation of specific hydrocarbons through the reduction of carbon dioxide. In same way, as the p-type semiconductor, for example, iridium oxide is a proven material as an electrode for the electrochemical oxidation of water,[21] and is expected to water splitting into oxygen and hydrogen. The proposed system is theoretically expected to be dramatically more efficient than conventional systems.

It was noted above that conventional PICS system can be applied to sensing devices. The proposed system can also work as a sensor with higher sensitivity than conventional one. It may be possible to simultaneously detect the hydrogen generation reaction as an electrical signal in the novel system. It will be able to detect not only hydrogen generation reactions, but also the progress of beneficial chemical reactions. This sensing system will be useful in a variety of systems in the future.

Conclusion

We have described the possibility of a novel, highly efficient hydrogen generation system using PICS with a p-type semiconductor. The proposed novel system is expected to realize high-sensitivity sensing at the same time. We believe that the realization of this system, which is expected to be able to effectively harvest and utilize energy of sunlight, will contribute to solving energy problems of the world.

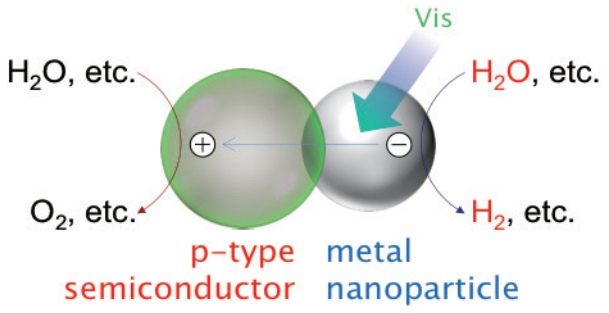

Figure 3 Schematic illustration of the PICS with p-type semiconductor.

References

[1] Solar Energy Perspectives, OECD/IEA, 2011.
[2] bp Statistical Review of World Energy 2020.
[3] M. Fleischman, P. J. Hendra, A. J. McQuillan, *Chem. Phys. Lett.*, 26, 163 (1974).
[4] C. Wen, K. Ishikawa, M. Kishima, K. Yamada, *Sol. Energy Mater. Sol. Cells*, 61, 339 (2000).
[5] S. D. Standridge, G. C. Schats, T. Hupp, *J. Am. Chem. Soc.*, 131, 8407 (2009).
[6] K. R. Catchpole, S. Pillai, J. *Luminescence*, 121, 315 (2006).
[7] D. Derkacs, S. H. Lim, P. Matheu, W. Mar, E. T. Yu, *Appl. Phys. Lett.*, 89, 093103 (2006).
[8] K. Nakayama, K. Tanabe, H. A. Atwater, *Appl. Phys. Lett.*, 93, 121904 (2008).
[9] P. Anger, P. Bharadwaj, L. Novotny, *Phys. Rev. Lett.*, 96, 113002 (2006).
[10] Y. Tian, T. Tatsuma, *J. Am. Chem. Soc.*, 127, 7632 (2005).
[11] T. Tatsuma, Y. Katagiri, S. Watanabe, K. Akiyoshi, T. Kawawaki, H. Nishi, E. Kazuma, *Chem. Commun.*, 51, 6100 (2015).
[12] Y. Takahashi, T. Tatsuma, *Appl. Phys. Lett.*, 99, 182110 (2011).
[13] E. Kowalska, R. Abe, B. Ohtani, *Chem. Commun.*, 241 (2009).
[14] Y. Takahashi, T. Tatsuma, *Nanoscale*, 2, 1494 (2010).
[15] Y. Takahashi, N. Miyahara, S. Yamada, *Anal. Sci.*, 29, 101 (2013).
[16] Y. Takahashi, K. Suga, T. Ishida, S. Yamada, *Anal. Sci.*, 32, 275 (2016).
[17] W. Kubo, T. Tatsuma, *J. Mater. Chem.*, 15, 3104 (2005).
[18] Z. Lian, M. Sakamoto, H. Matsunaga, J. J. M. Vequizo, A. Yamakata, M. Haruta, H. Kurata, W. Ota, T. Sato, T. Teranishi, *Nat. Commun.*, 9, 2314 (2018).
[19] Y. Takahashi, Y. Yamadori, T. Murayama, S. Shingo, S. Yamada, in preparation.
[20] Y. Hori, R. Takahashi, Y. Yoshinami, A. Murata, *J. Phys. Chem. B*, 101, 7075 (1997).
[21] Y. Takahashi, T. Tatsuma, *Electrochemistry*, 82, 749 (2014).

Dr. TAKAHASHI Yukina

Associate Professor,
International Institute for Carbon-Neutral Energy Research (I^2CNER),
Kyushu University

Data Driven Acceleration of Materials Discovery Through Integrated Correlative Spectroscopy, Synthesis, and Experimentation

Helge Sören STEIN

An acceleration of the transition towards renewable energy production and storage necessitates new breakthrough materials. Discovering such new and improved materials does, however, call for new paradigms that incorporate combinatorial materials science and high-throughput experimentation to fast-track materials scaling from discovery to product. Herein a brief example of materials science acceleration through integrating complex workflows is explored as implemented in the platform for accelerated electrochemical energy storage research (PLACES/R) located at the Helmholtz Institute Ulm. With the synthesis, characterization, and performance evaluation techniques, we seek to unravel the physicochemical relationships between composition, structure, processing, and performance to discover and upscale future materials for short- and long-term energy storage.

Introduction

There is a critical need for new and improved materials for intermittent renewable energy storage[1] in both stationary and mobile applications.[2] Here it is however not just important to find the highest performing[3] material for a given functional property,[4] but it is also important to discover materials that are scalable. Scalable on the TWh scale, which is the energy storage need of countries and continents, means that a material may only be comprised of earth abundant constituents and made through low-temperature green-chemistry processes.[2] Most of the currently available chemistries for Hydrogen production[5] or for batteries[6] do only fulfill this requirement in part leaving great opportunities for materials discovery and optimization.[7]

The first wave of trying to accelerate materials science was started in fact in the 1990s in Japan[8] after some early experiments in the 1950s in Germany.[9] Both times scientists tried to optimize expensive to manufacture materials like dental alloys[9],[10] containing gold or silver. The method of choice back then, and still today, was the synthesis of thin films using various CVD or PVD techniques.[11] In the 1990s there was a trend towards automation which is why there had been a trend for almost 30 years to deploy automation to materials science.[12]

The advancements in the field of "combinatorial materials science" (CMS) offered bespoke combinatorial synthesis and high-throughput characterization (using high-throughput experimentation - HTE). Many of these had the idea of connecting these systems to data management but few implemented a thorough integration.[13] In the late 2010s there was then the push for accelerated materials understanding in the so called "materials genome initia-

tive".[14],[15] There scientists sought to screen hundreds of thousands of materials using computational tools to then synthesize them using the methods available from CMS and HTE. The paradigm then was to perform so called inverse design such that one could query a functional property and receive from correlators and models a structure, composition, or processing route. Given however the vast breath and complexity of the chemical space it became evident that the descriptors and underlying physicochemical relationships were well beyond one- or two-dimensional descriptors and with the explosive rise of capabilities in data science the community shifted towards autonomous materials science. In autonomous materials science there is the idea to build so called materials acceleration platforms (MAP)[12],[16] in which research tasks such as synthesis, characterization, data-management etc. are not just accelerated through automation or use of databases but also integrated through data pipelines and robotic automation.[6] Using the perspective of accelerated and integrated research tasks one can in fact measure the acceleration of materials science through the MAP paradigm. Early demonstrations have in fact shown accelerations[4] of up to 20x but even greater accelerations should become available in the near future.

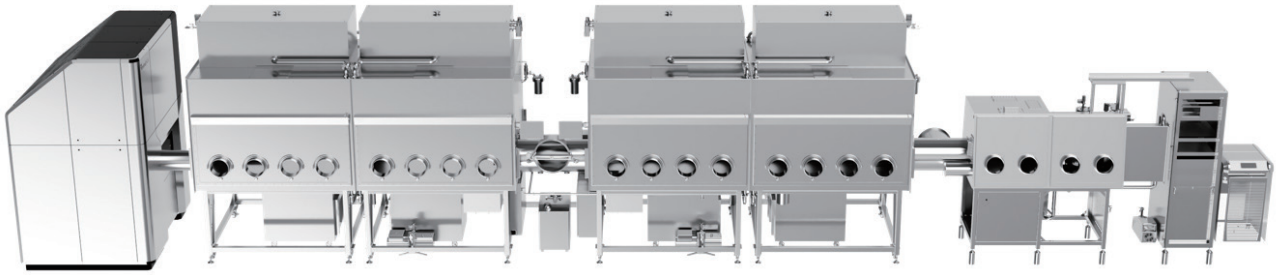

Figure 1 Rendering of the platform for accelerated electrochemical energy storage research (PLACES/R) that houses (from left to right) a near ambient pressure X-ray photoelectron spectrometer (NAP-XPS), high-throughput spectrometers and electrolyte formulation robots (left glove box), several scanning droplet cells and a coin cell assembly robot (right glovebox) as well as a sputtering system (right hand side).

Building a platform

In the following I will briefly describe an example set of measurements that highlight how the paradigm of a materials acceleration platform can be implemented. A platform is more than the sum of its parts as the overall added value is being created in the integration of its modules. Alone each setup and method can be accelerated but it is the integration that makes the difference over conventional high-throughput materials research.

Automation framework

The first and foremost important tool to build a platform that can acquire data on various of materials on different carriers using a multitude of techniques is the automation framework.[7] Given the challenge of building a laboratory[6] that utilizes instruments from a variety of vendors my current team, my coworkers from JCAP and I developed the hierarchical experimental laboratory automation and orchestration framework (HELAO). For this software we have written drivers for each and every device in our laboratory that expose them through a REST API - essentially a web server to which commands can be send. The driver functions are relatively low level i.e. turning a motor by 12 revolutions at 5 revolutions/second. More complex features are grouped into something we call action servers i.e. moving a probe by 5 mm in x-direction and 2 mm in y-direction. A sequence of actions or sequence of events makes up an experiment. A list of experiments makes up a campaign or session. Because the communication with actions and drivers can be achieved through small JSON files (essentially nested dictionaries containing instructions) an experimental session becomes programmable and interchangeable[17] between instruments (devices make up instruments).

Data management

Having all data acquisition and reporting done through code also enables fine grained data management that also entails all details of how data was acquired and processed. Any downstream processing,[18],[19] if automated, can also be integrated and be used to expand the capabilities of autonomous workflows. Currently we have drivers for stages, robots, I/O boards, potentiostats and spectrometers including even NMR. We can thus build complex workflows.

Instruments

Second are the instruments themselves. In electrochemical energy storage research there are a lot of pertinent techniques, we do however currently focus on Raman and FTIR spectroscopy in a self-build integrated setup called HITS (High-throughput spectrometer), four scanning droplet cells to perform millimeter scale high-throughput half-cell battery research (MISCHBARES), a setup for Autonomous Synthesis and Analysis of Battery electrolytes (ASAB), an automatic battery assembly robot (AutoBASS),[20] and various auxiliary and supporting techniques like high-throughput XRF and near ambient pressure XPS.

Examples

Due to the modularity of our platform,[6] there is not a single common or even "standard" workflow but several emblematic "workflow paths" through which insights can be generated. The earliest example in our laboratory was in fact the corrosion of copper and subsequent analysis using Raman and FTIR as offered through our in-house build high-throughput spectrometer (HITS) that has two Raman probes (green and red lasers) and a FTIR probe from OEM manufacturers.[21] A great benefit of high-throughput Raman spectroscopy is, that it is a relatively fast hyperspectral mapping technique that cannot just be used to fingerprint a crystal structure, but it also bears the possibility to pinpoint the location of a measurement area with great accuracy. Figure 2 shows an emblematic mapping of a materials library where the false color spots demarcate areas at which electrochemical experiments were performed. Further correlation between the Raman signals and the electrochemical protocol employed can unravel corrosion behavior. Here, we used a simple copper foil, but the possibilities are virtually unlimited in terms of materials composition through combinatorial synthesis techniques such as reactive magnetron sputtering or coating of powders.

Coating of powders is however a tedious process that requires manual finetuning of process parameters. We have however recently employed screen printing of electrodes to manufacture materials libraries for use in the scanning droplet cell (SDC). These libraries offer the benefit of being rapidly deposited and then analyzed by various subsequent methods such as X-ray fluorescence (XRF), SDC and HITS prior and post to SDC. In Figure 3 a XRF intensity map over such a materials library containing 121 Lithium iron phosphate, a common cathode material in batteries, measurement areas are shown. These measurement areas can now be analyzed using all the available techniques in our lab and be also used in full cell setups using larger area coatings (different screen-printing mask) in the AutoBASS[20] setup. The AutoBASS setup is shown in Figure 4. Here, a single battery can be assembled by a robot in under 3 minutes.

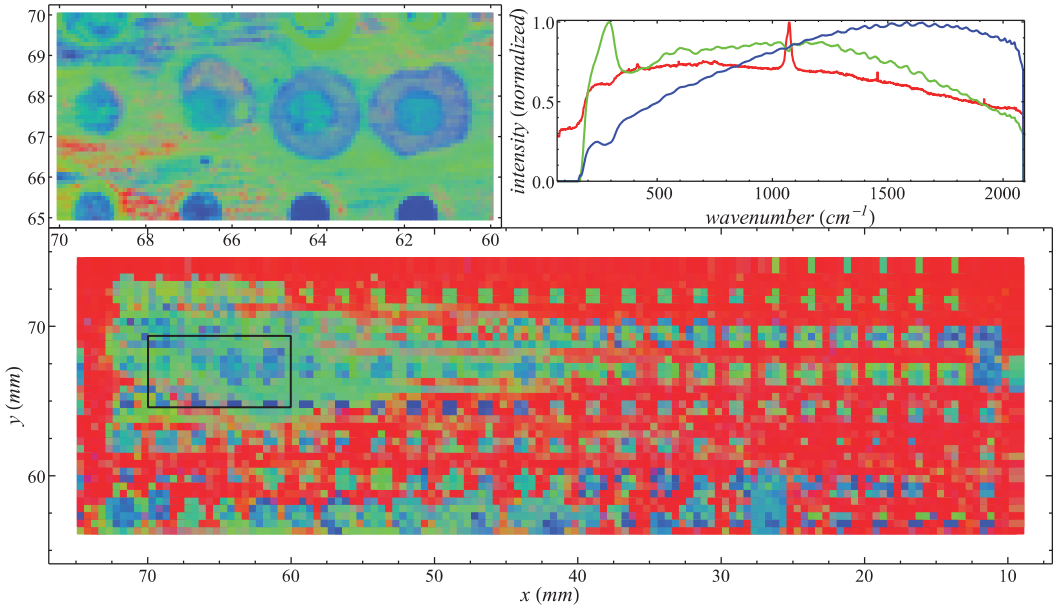

Figure 2 False color mappings using Raman spectroscopy and non-negative matrix factorization to create maps of three different phases corresponding to a background of metallic copper, and two corrosion phases. The top left image shows a zoomed in region, the top right shows the deconvoluted base spectra and the bottom part of the figure shows a large area overview of the materials library. The black box marks the area in which a high-resolution mapping was performed. The corrosion products were produced using scanning droplet cell electrochemistry.

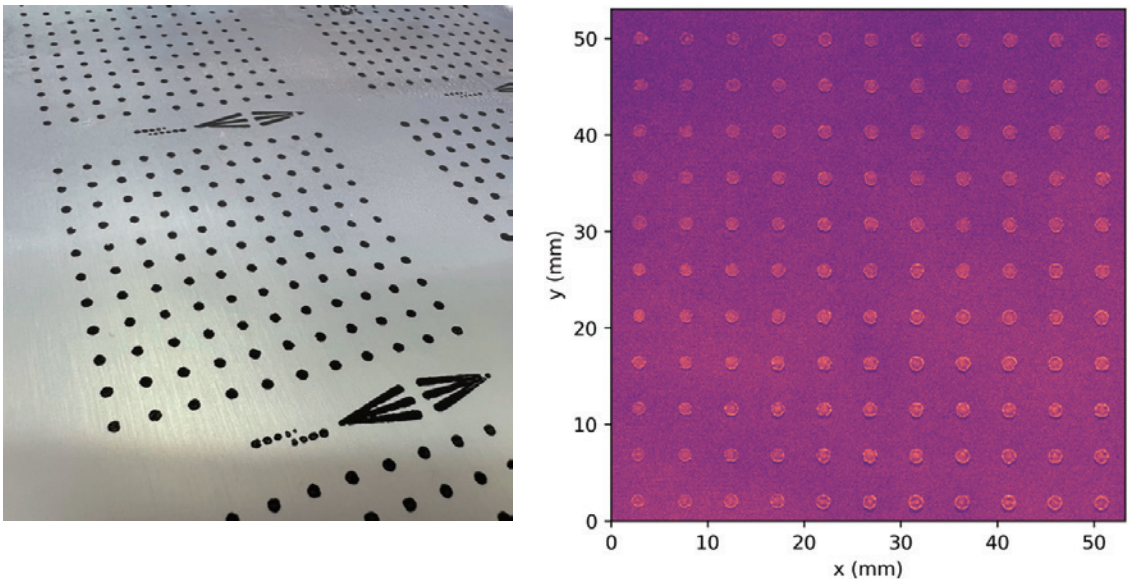

Figure 3 Left: Photograph of a screen printed materials library of Lithium iron phosphate (LFP) after drying in ambient air.
Right: X-ray fluorescence mapping of a materials library coated through screen printing after drying. Brighter spots mark the areas where LFP was deposited through the screen printing mesh. The slight gradient from the top left to the bottom right is intended as the mask contained different effective mesh sizes to vary LFP loading over the materials library. The XRF measurements were performed using a HORIBA XGT-9000 with a polycapillary probe. Using the scanning droplet cell in a similar way as shown in Figure 2 it is possible to assess real battery materials without measurement area crosstalk.

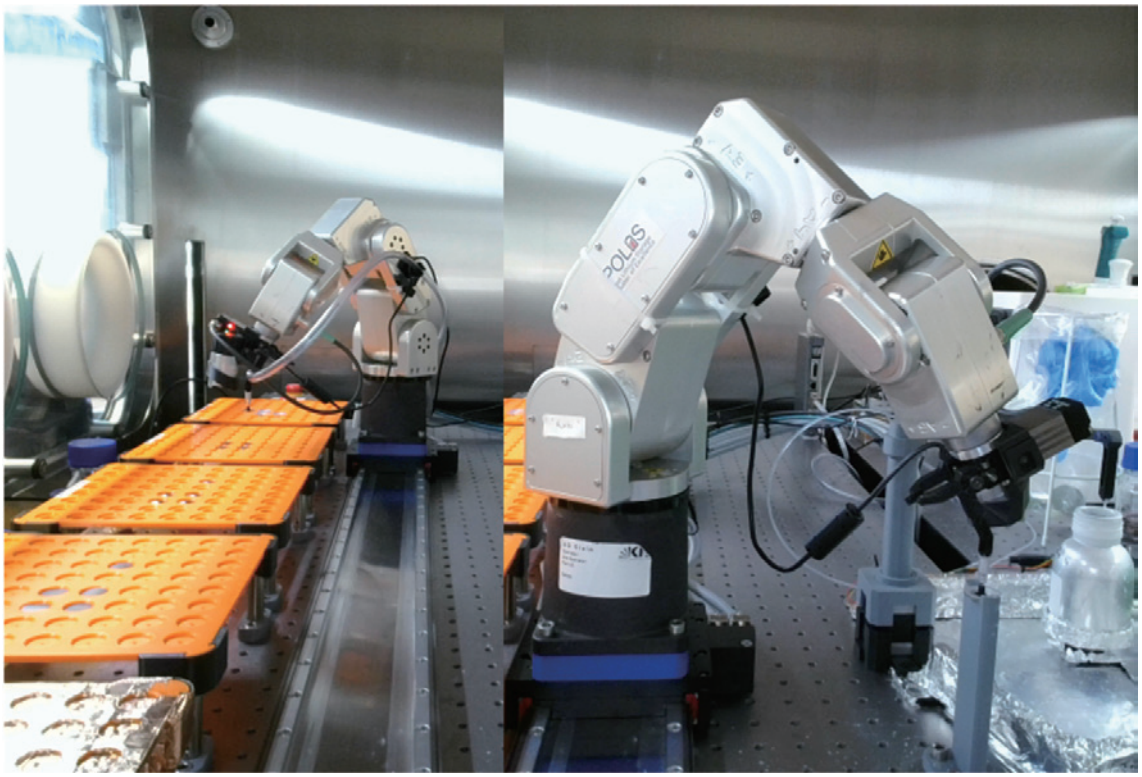

Figure 4 Photograph of the pick and placing actions of AutoBASS, a robot for the automatic assembly of coin cell batteries. On the left the robot is shown picking up cell components that are placed onto an assembly post on the right. On the assembly post additional steps such as electrolyte filling are performed. The entire process is housed inside a nitrogen filled glovebox to avoid moisture and oxygen impurities.

Conclusion

Using additional tools such as ASAB and the XPS we can thus cover the entire materials research value chain and integrate insights from all steps of battery research and even catalysis. Being able to acquire data from bulk, interface, and interphase processes in combination with system and long-term effects opens up new and interesting research directions. Through fine grained data management and automation control we also have the unique opportunity to deploy A.I. guidance of our robotic systems. With novel orchestration paradigms and software such as FINALES we can even integrate external data sources and measurement requests to build workflows across laboratories and modalities to create the lab of the future.

Acknowledgements

I thank my entire team that made this platform possible. For this technical report I'd especially thank Jackson Flowers, Fuzhan Rahmanian, Leah Nuss, Stefan Fuchs and Bojing Zhang.

References

[1] J. Amici *u. a.*, „A Roadmap for Transforming Research to Invent the Batteries of the Future Designed within the European Large Scale Research Initiative BATTERY 2030+“, Advanced Energy Materials, S. 2102785, 2022.

[2] M. Fichtner *u. a.*, „Rechargeable Batteries of the Future—The State of the Art from a BATTERY 2030+ Perspective“, *Advanced Energy Materials*, S. 2102904, 2021.

[3] A. Benayad *u. a.*, „High-throughput experimentation and computational freeway lanes for accelerated battery electrolyte and interface development research“, *Advanced Energy Materials*, Bd. 12, Nr. 17, S. 2102678, 2022.

[4] B. Rohr *u. a.*, „Benchmarking the Acceleration of Materials Discovery by Sequential Learning“, *chemrxiv*, S. 10-26434, 2019.

[5] L. Zhou *u. a.*, „Combinatorial screening yields discovery of 29 metal oxide photoanodes for solar fuel generation“, *Journal of Materials Chemistry A*, Bd. 8, Nr. 8, S. 4239-4243, 2020.

[6] H. S. Stein *u. a.*, „From materials discovery to system optimization by integrating combinatorial electrochemistry and data science“, *Current Opinion in Electrochemistry*, S. 101053, 2022.

[7] F. Rahmanian *u. a.*, „Enabling Modular Autonomous Feedback-Loops in Materials Science through Hierarchical Experimental Laboratory Automation and Orchestration“, *Advanced Materials Interfaces*, Bd. 9, Nr. 8, S. 2101987, 2022.

[8] H. Koinuma und I. Takeuchi, „Combinatorial solid-state chemistry of inorganic materials“, *Nature Mater*, Bd. 3, Nr. 7, Art. Nr. 7, Juli 2004, doi: 10.1038/nmat1157.

[9] A. Boettcher, G. Haase, und R. Thun, „Strukturuntersuchung von Mehrstoffsystemen durch kinematische Elektronenbeugung“, *Z. Metallkde.*, Bd. 46, Nr. 5, S. 386-400, 1955.

[10] J. Li *u. a.*, „Combinatorial screening of Pd-based quaternary electrocatalysts for oxygen reduction reaction in alkaline media“, *Journal of Materials Chemistry A*, Bd. 5, S. 67-72, 2016.

[11] A. Ludwig, „Discovery of new materials using combinatorial synthesis and high-throughput characterization of thin-film materials libraries combined with computational methods“, *npj Computational Materials*, Bd. 5, Nr. 1, Dez. 2019, doi: 10.1038/s41524-019-0205-0.

[12] H. S. Stein und J. M. Gregoire, „Progress and prospects for accelerating materials science with automated and autonomous workflows“, *Chemical Science*, Nr. 10.1039/C9SC03766G, 2019.

[13] L. Banko und A. Ludwig, „Fast-Track to Research Data Management in Experimental Material Science-Setting the Ground for Research Group Level Materials Digitalization“, *ACS Comb. Sci.*, Bd. 22, Nr. 8, S. 401-409, Aug. 2020, doi: 10.1021/acscombsci.0c00057.

[14] M. L. Green *u. a.*, „Fulfilling the promise of the materials genome initiative with high-throughput experimental methodologies“, *Applied Physics Reviews*, Bd. 4, Nr. 1, S. 11105, 2017, doi: 10.1063/1.4977487.

[15] A. Jain *u. a.*, „Commentary: The materials project: A materials genome approach to accelerating materials innovation“, *APL Materials*, Bd. 1, S. 011002, 2013.

[16] M. M. Flores-Leonar *u. a.*, „Materials Acceleration Platforms: On the way to autonomous experimentation“, *Current Opinion in Green and Sustainable Chemistry*, Bd. 25, S. 100370, Okt. 2020, doi: 10.1016/j.cogsc.2020.100370.

[17] M. D. Wilkinson *u. a.*, „The FAIR Guiding Principles for scientific data management and stewardship“, *Scientific Data*, Bd. 3, S. 160018-9, März 2016, doi: 10.1038/sdata.2016.18.

[18] F. Rahmanian *u. a.*, „Conductivity experiments for electrolyte formulations and their automated analysis“, *Sci Data*, Bd. 10, Nr. 1, S. 43, Jan. 2023, doi: 10.1038/s41597-023-01936-3.

[19] F. Rahmanian *u. a.*, „One-Shot Active Learning for Globally Optimal Battery Electrolyte Conductivity“, *Batteries & Supercaps*, Bd. 5, Nr. 10, S. 1-9, 2022, doi: 10.1002/batt.202200228.

[20] B. Zhang, L. Merker, A. Sanin, und H. S. Stein, „Robotic cell assembly to accelerate battery research“, *Digital Discovery*, Bd. 1, Nr. 6, S. 755-762, Dez. 2022, doi: 10.1039/D2DD00046F.

[21] S. Daboss, F. Rahmanian, H. S. Stein, und C. Kranz, „The potential of scanning electrochemical probe microscopy and scanning droplet cells in battery research“, *Electrochemical Science Advances*, S. e2100122, 2021.

Dr. Helge Sören STEIN

Tenure Track Professor,
Institute for Physical Chemistry (IPC) & Helmholtz Institute Ulm (HIU),
Karlsruhe Institute of Technology (KIT)

HORIBA Institute for Mobility and Connectivity^2 for Contributing to the Transformation of Energy and Mobility Systems

KINOSHITA Akio

A new research institute was established in July 2021 at the University of California, Irvine with a donation from the HORIBA Group. The institute aims to promote research from a new perspective by integrating and rethinking the social infrastructure of energy and mobility, which will be deeply interrelated in the future. This article introduces the concept of the institute and some examples of its activities.

Figure 1 HIMaC^2 Opening Ceremony. (Oct. 11, 2022)
(from left to right) HIMaC^2 Inaugural Director Vojislav Stamenkovic, HORIBA, Ltd. Chairman & Group CEO Atsushi Horiba, UCI Chancellor Howard Gillman, HORIBA Ltd. Executive Corporate Officer Jai Hakhu, UCI Dean of Engineering Magnus Egerstedt.

Introduction -Trends in Energy and Mobility

The entire world is now facing an urgent challenge to cope with global warming. As of the COP26 summit, more than 150 countries including the G20 have set a deadline for declaring their carbon neutrality goals. In response to this, shifting to renewable energy has become a major trend, and energy procurement has become a major focus of attention from the perspective of national security. On the other end, mobility is one of the major sources of energy consumption and the rapid expansion of electric vehicles is progressing, especially in China and Europe, followed by the US and other regions.

In parallel, automobiles are becoming more automated and connected, and some attempts are being explored to save energy as a whole by having a group of vehicles run in a coordinated manner using these technologies. This situation can be seen as an indication of the process of integration of the three major infrastructures of energy, mobility, and information and communication. These structural changes are the basic background for the establishment of the HORIBA Institute for Mobility and Connectivity^2 (HIMaC^2).

Research Direction at HIMaC² - Background and Concept

The energy supply system that forms the basis of today's society is based on the concept of a stable supply of electricity produced intensively at a rather limited number of power plants, as in the case of electric power generation > transmission > distribution. In contrast to this so-called one-way structure of power supply from the center to every corner of the entire grid, there is now a rapidly growing demand for expanding the use of renewable energy and local production for local consumption of energy. With this trend, elements such as photovoltaic cells and rechargeable batteries as intermediate energy storage are being added, and the electric power network which has been one-way and stably controlled, is changing to a more distributed, open and interactive form.

As is well known, renewable energies such as solar power, wind power, wave power, etc., all fluctuate greatly and are difficult to predict, which is a major challenge from the viewpoint of stable supply. It is not always clear how they should be arranged and operated, and how to guarantee the stable operation of the entire system. In addition to the placements of generation and storage capacities and the scheduling of charging and discharging, how to design and operate the network, including system stability assurance, resilience against unexpected fluctuations, and total cost including maintenance and renewal, are issues that should be fully considered.

On the other hand, automobiles have long derived most of their energy from gasoline and diesel fuel refined from crude oil, which exists unevenly on earth. Instead, we are now entering a period of change that is said to occur only once every 100 years, and the use of electric vehicles is expanding significantly. Future vehicles will also need to be seen as an integrated part of the network, storing electric energy and interacting with the electric power network through charging and discharging. In addition, hydrogen will play an important role as an energy medium, converted from electrical energy via water electrolysis and used as a medium for energy storage and transportation, or directly as an energy source for vehicle propulsion via onboard fuel cells or even internal combustion engines.

From this perspective, the energy network including automobiles is shown in Figure 2. First, a variety of renewable energy sources are provided as primary energy. In addition, automobiles will be equipped with large-capacity storage batteries, and hybrid and battery EVs will directly transfer energy to and from the network side. In such a "21st century type" energy network, it is necessary to explore a new front of technologies such as energy management method for decentralized and interactive energy network, and all the technology pieces for

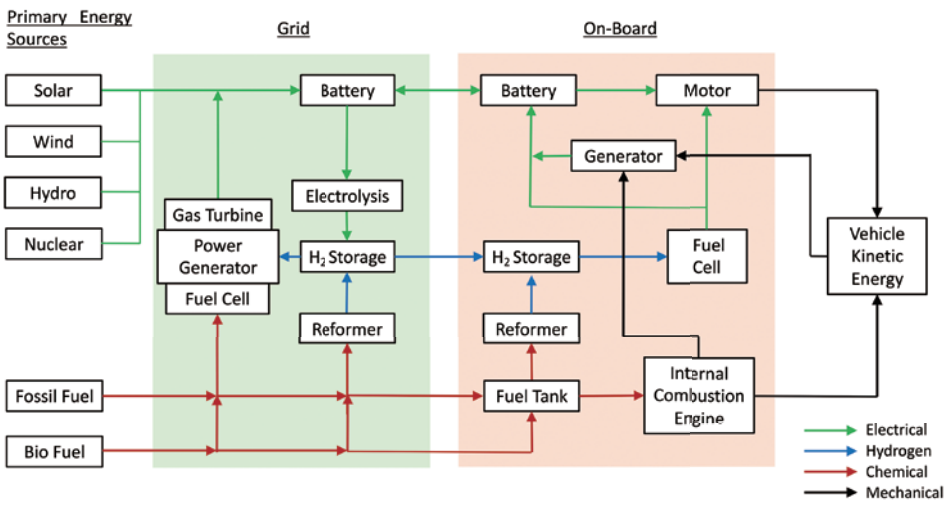

Figure 2 A Comprehensive View of Energy Network Integrated with Vehicles.

energy conversion systems by means of electrochemical reactions instead of combustion reactions.
In addition to the improvement of the efficiency of energy conversion as a basic challenging research issue, understanding and controlling the dynamic behavior of the system as a whole is also an unexplored area. Because of the interdisciplinary nature of the problem and the fact that it involves not only individual elements but also multiple layers of systems, a cross-disciplinary approach is indispensable in order to understand the essential aspects of the problem and to consider the direction of next-generation infrastructure.

Laboratory Structure of HIMaC^2

The Advanced Power and Energy Program (APEP) at the University of California, Irvine (UCI) has a long history of leading research in the energy field. UCI has pioneered a variety of research projects, such as combustion research as early as 1970, when the Muskie Act was introduced, power grid research, and hydrogen energy utilization technology. On the basis of these long-standing achievements, HIMaC^2 was established being aware of the aforementioned energy network issues, and Prof. Vojislav Stamenkovic, a world leader in the field of electrochemical materials science, was appointed as the inaugural director of the institute.
HIMaC^2 is composed of the following four laboratories, reflecting the recognition of the issues described in the previous chapter.

- Vehicle Evolution Laboratory (VEL): This laboratory evaluates and researches on-board electric vehicle elements and system technologies. For this purpose, the VEL is equipped with HORIBA measurement systems, dynamometers, and environmental chambers for rechargeable battery evaluation (Figure 3).

- Grid Evolution Laboratory (GEL): This laboratory is for conducting research on the grid level problems, including Grid-to-vehicle and Vehicle-to-grid power network dynamics. The GEL is equipped with a grid simulator that can reproduce dynamic phenomena in various power systems.

Figure 3 Vehicle Evolution Laboratory.

- Connected and Autonomous Mobility Laboratory (CAML): This laboratory conducts research on the impact of Vehicle-to-vehicle and Vehicle-to-infrastructure communication on individual vehicles, traffic flow, energy efficiency, etc., as well as AI-based control, which includes the possibility of automated driving. The CAML has introduced a simulation platform for cooperative driving control developed by HORIBA MIRA.

- Analytic Laboratory (AL): The following state-of-the-art HORIBA analytical instruments are installed to analyze and study the advanced electrochemical materials that form the fundamental basis of the above-mentioned systems and grid-level phenomena.
  - LabRAM HR Evolution Nano: AFM Raman Spectrometer
  - XGT-9000: X-ray Analytical Microscope (Micro-XRF)
  - nanoPartica SZ-100V2: Nanoparticle Analyzer
  - GD-Profiler2: Glow Discharge Optical Emission Spectrometer

Since future issues in the energy field will cover a deep multi-layered structure ranging from materials properties to devices, systems, and even to the entire grid, each laboratory is organized according to the respective hierarchical level. By organically combining these laboratories, it is possible to tackle new issues and phenomena by traversing the hierarchy, which may not have been sufficiently addressed in the past. In addition, UCI can conduct actual experiments at the grid level by using its on-campus energy network itself as an independent microgrid. This microgrid is also connected to photovoltaic cells and hydrogen-related facilities, providing an environment that can handle an extremely broad and comprehensive range of studies. With the unique research functions and configurations described above, the institute has great potential for future research horizons.

HIMaC² Research Project Examples

Although HIMaC² is still in the start-up phase shortly after its opening, various research projects have already been initiated, including many funded by major government agencies. The following is a list of major projects underway at the time of this writing.

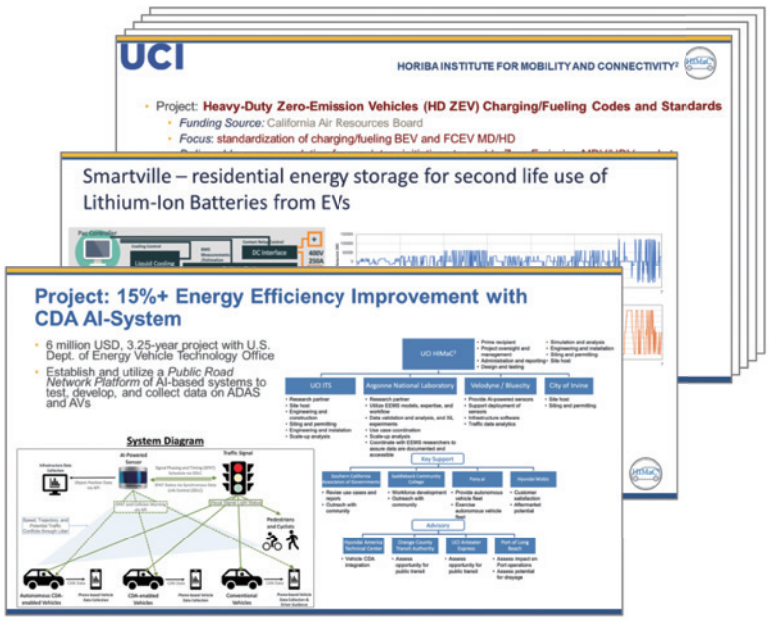

Figure 4 Examples of Research Projects at HIMaC².

1. Smartville: Research on technologies to utilize used batteries with a spin-off company from University of California, San Diego
2. Microgrid-in-a-Meter: Research on technologies to cope with dynamic events such as power outages in isolated grid systems including photovoltaic cells
3. HD-ZEV Charging/Fueling Codes and Standards: Basic research for standardization of energy fueling codes for heavy-duty electric and hydrogen vehicles
4. Aqueous, air breathing long-duration energy system: Research on a new type of non-Li-ion battery
5. Smart Cities and Connected and Autonomous Vehicles: Research on AI-based traffic control infrastructure coordination to improve energy efficiency with a view to self-driving vehicles
6. M^2CFT: Research on catalytic materials for the anode as part of the Million Mile Fuel Cell Truck Consortium
7. Break Dust Project: Evaluation study on the effects of brake and tire dust

Many of the above projects are supported by public organizations, e.g., 3 is publicly funded by the California Air Resources Board, and 4 and 5 are funded by the federal Department of Energy. In addition, many joint projects with other universities and research institutes are underway.

Conclusion

As mentioned above, the HORIBA Institute for Mobility and Connectivity[2] has started its activities at a right timing, when the energy and mobility networks are undergoing major changes. The institute is already taking a leadership role at the forefront of unprecedented research into the diverse issues that society as a whole will face in the future. It is expected to pioneer new knowledge that will contribute to solving future issues through specific research projects in collaboration with various stakeholders, including government, academia, industry across the energy and mobility sectors.

Lastly, in preparing for the establishment of this institute, we owe much to Professor Scott Samuelsen, the founder of APEP and a long-time leader in energy research in the United States. I conclude this article by expressing our gratitude to Professor Samuelsen for his forward-looking leadership through all the steps that enabled this landmark institute.

KINOSHITA Akio

Fellow
HORIBA, Ltd.
Ph.D.

Analytical Techniques Contributing to the Research and Development of All-Solid-State Batteries

TSUBOTA Takayuki
Manager
EV Battery Analysis & Evaluation section
EV Battery Solution Center
Kobelco Research Institute, inc.
Doctor of Science

The worldwide shift to EVs in automobiles is accelerating in order to reduce CO_2 during driving, and the demand for rechargeable batteries is increasing. Research and development of all-solid-state batteries using solid electrolytes that exhibit high Li ion conduction is underway, and this paper outlines the development trends and challenges. Analytical technology corresponding to non-atmospheric exposure is essential for the practical application of all-solid-state batteries. Comprehensive analytical evaluation and analysis techniques are important, including chemical state and structural analysis of solid electrolytes, observation techniques for the junction interface between solid particles in all-solid-state batteries, and electronic conductivity path analysis.

Introduction

Since the adoption of the Paris Agreement at COP21 (21st Conference of the Parties to the United Nations Framework Convention on Climate Change) in 2015, the world has taken a major step toward the realization of a decarbonized society. In Japan, “Achieving a carbon neutral, decarbonized society by 2050” was declared in October 2020. Carbon neutrality means that greenhouse gas emissions and sinks must be balanced and virtually zero. In December of the same year, the “Green Growth Strategy for Carbon Neutrality in 2050” was formulated.

Energy decarbonization includes electrification, hydrogenation, and the use of carbon-recycling fuels, but storage batteries are essential for promoting electrification. In the automotive industry, the European Union (EU) has agreed to effectively ban the sale of gasoline-powered and other internal combustion engine vehicles by 2035. In Japan, a policy to achieve 100% electric vehicles in new passenger car sales by 2035 was announced in 2021. The electric vehicles referred to here are electric vehicles (EV), hybrid vehicles (HV), plug-in hybrid vehicles (PHEV), and fuel cell vehicles (FCV). Against this backdrop of decarbonization, the shift to EVs is accelerating in the automotive industry.

Liquid-based Li ion batteries are mainly used in EVs. Since battery performance has a large impact on vehicle performance, such as cruising range and acceleration, development of materials such as active materials for positive and negative electrodes, separators, and electrolyte is underway to achieve higher capacity, higher input/output, and improved durability. However, the energy density of liquid-based Li ion batteries is said to be limited at around 250 Wh / kg, and new batteries with even higher energy density are required. Sodium ion batteries as post Li ion batteries and multivalent cation batteries such as calcium ion batteries are being considered.

In recent years, the development of sulfide-based solid electrolytes, which are high Li ion conductors, has been actively pursued, and all-solid-state Li ion batteries have attracted attention as a new type of battery that is expected to have an energy density higher than that of liquid-based Li ion batteries.

Kobelco Research Institute. Inc (KRIJ) possesses technologies for prototyping and internal resistance analysis of Li ion rechargeable batteries, degradation analysis of components through battery disassembly and instrument analysis, computer simulation, and safety evaluation. Further to this, they have established comprehensive evaluation and analysis technologies for rechargeable batteries. In all-solid-state batteries, we have technologies ranging from the synthesis of solid electrolytes to battery

prototyping and evaluation, and we are supporting research and development of all-solid-state batteries.

This paper reports on the analytical techniques required for the research and development of all-solid-state batteries, focusing on a case study in collaboration with HORIBA, Ltd.

Features and Challenges of All-Solid-State Li ion Batteries

All-solid-state Li ion batteries are characterized by the fact that the electrolyte is replaced by a solid electrolyte that is a high ionic conductor, and the cathode composite layer, solid electrolyte layer, and anode composite layer are all composed of solid materials. Solid electrolytes are mainly classified into sulfide systems[1-7] represented by $Li_7P_3S_{11}$, $Li_{10}GeP_2S_{12}$ (LGPS) and oxide systems[8] represented by $Li_7La_3Zr_2O_{12}$ (LLZ). By selecting solid electrolytes, which have electrochemical stability at higher potentials compared to liquid electrolytes, it is possible to use 5V-class active materials such as $LiNi_{0.5}Mn_{1.5}O_4$ that have been difficult to apply in liquid-based batteries, thus increasing energy density.

Good input/output characteristics are also expected. In electrolyte, anions in addition to Li ions contribute to conduction, resulting in low transfusion rate, but anions in solid electrolyte only form the framework and do not contribute to conduction. In other words, solid electrolyte is a single conductor of Li ion and the transporter ratio is 1, resulting in high ionic conductivity.

Sulfide-based solid electrolytes, such as glass sulfide electrolyte $Li_7P_3S_{11}$,[1,2] the crystalline electrolyte $Li_{10}GeP_2S_{12}$ (LGPS),[3-5] and the argyrodite-type Li_6PS_5X (X=Cl, Br, I),[6,7] have excellent ion conductivity. Solid electrolytes with ion conductivities of the order of 10^{-2} S/cm, exceeding that of organic electrolytes, have been reported. Figure 1(a) shows the ionic conductivity of solid electrolytes synthesized by our company.[9] The crystal structure of Li_6PS_5Cl, an argyrodite-type sulfide solid electrolyte, is shown in Figure 1(b) as a representative crystalline electrolyte. The chloride ions form a face-centered cubic (FCC) lattice (4a, 4c) and the Li ions are randomly distributed in tetrahedral positions; P occupies the tetrahedral site (4b) and S forms a PS_4^{3-} tetrahedral unit in the structure.

While all-solid-state Li ion batteries are expected to have high energy density and high input/output characteristics, there are challenges in materials and manufacturing processes for practical use, and research and development is being conducted from this perspective. Since all the components of an all-solid-state battery are solid, it is required to form and maintain a good bonding interface between the solid electrolyte and the active material interface. It is crucial to monitor the battery's deformation during molding as well as the active material's expansion and contraction due to charging and discharging. For this reason, the development of all-solid-state batteries with flexible deformation capabilities using sulfide-based solid electrolytes is primarily being supported for automotive applications. Solid sulfide electrolytes are highly reactive and easily hydrolyzed by moisture in the atmosphere to generate hydrogen sulfide, so they must be handled in a low

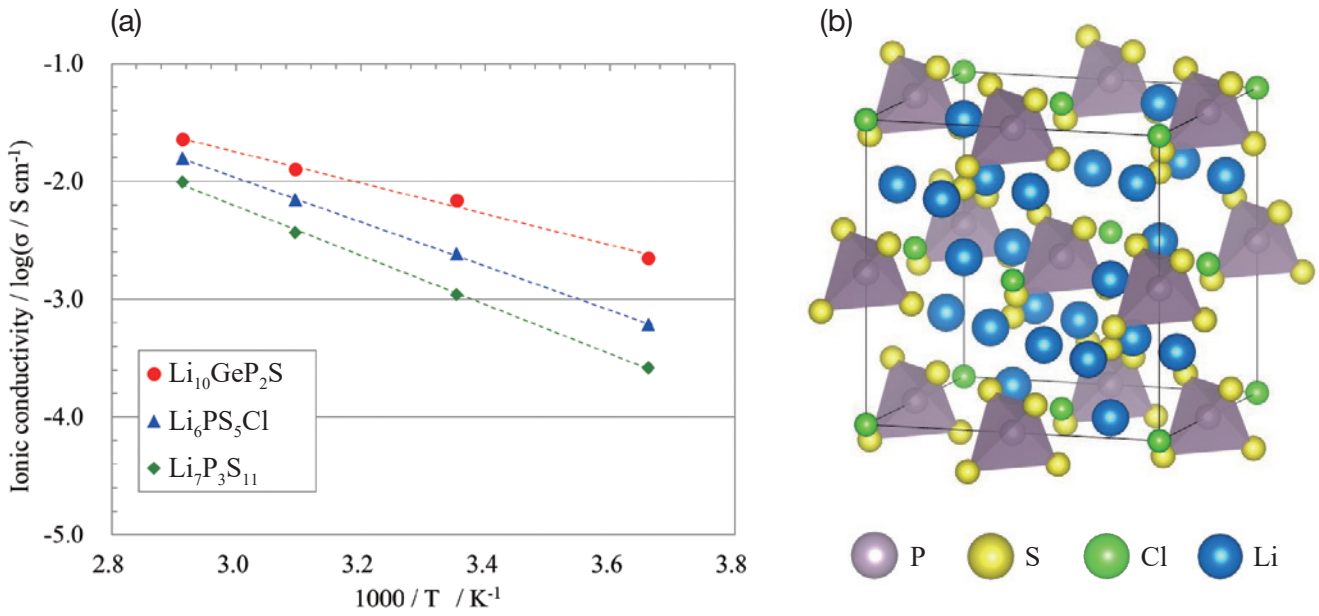

Figure 1 (a) Ion conductivity of sulfide-based solid electrolytes. (b) Crystal structure of Li_6PS_5Cl solid electrolytes.

Table 1 Analysis technology for secondary batteries.

Development issues		Focus points	Analytical methods
Optimization of solid-state electrolytes	Improvement of ionic conductivity	• Crystal structure • Chemical state	• XRD, in-situ XRD • Raman, in-situ Raman
	Improvement of stability	• Atmospheric stability	• Exposure test + Gas analysis
Optimization of the coating layer	Improvement of coverage Homogenization of the coating	• Coverage, uniformity	• XPS, TOF-SIMS
Optimization of electrode and cell structures	Improvement of the dispersibility of materials	• Dispersion state, unevenness	• SEM + image analysis
	Improvement of the flowability of materials	• Flowability, adhesion	• Flowability test
	Understanding of material and electrode strengths	• Crushing strength, hardness • Modulus of elasticity	• Crushing test, Nanoindentation • SPM, Nanoindentation
	Improvement of the adhesion of each layer	• Interface adhesion	• SAICAS, peel test
	Optimization of Li ion and electron paths	• Electrode structure observation • Effective conductivity analysis	• 3D-FIB-SEM • Image analysis • Symmetric cells + resistance analysis
Battery characteristics Optimization of battery characteristic control and management	Understanding of battery characteristics	• Cycle characteristics, temperature characteristics	• Creating prototype cells + charge/discharge test
	Clarification of the degradation mechanism	• Composition distribution in the electrode • Chemical state distribution in the electrode • Reaction phase at the interface between solid electrolyte and active material • Valence and local structure of active material • Morphological changes during charge/discharge	• GD-OES • Diagonal cutting XPS • Cryo biaxial Cs-STEM • XAFS/Synchrotron radiation • In-situ SEM
	Understanding of thermal properties	• Thermal conductivity • Specific heat	• Hot disk method, heat transfer analysis • DSC, external heating evaluation of cells
	Understanding of safety	• Reaction heat evaluation	• DSC • Safety test

dew point Ar atmosphere glove box with strict moisture control.[10] In various types of analysis, it is essential to handle the materials in a non-exposed atmosphere throughout the entire process from sampling, transportation to the analysis equipment, and measurement. Table 1 shows a list of analytical techniques required for research and development of all-solid-state batteries.

Application of Raman Spectroscopy (RS) in Solid Electrolyte Synthesis

The synthesis of solid electrolytes can be roughly divided into solid-phase and liquid-phase processes. Mechanical alloying (MA), which is typical of solid-phase processes, is a method used to obtain solid electrolytes in amorphous or thermodynamically metastable phases by mechanically applying energy to accelerate chemical reactions. The liquid phase procedure involves submerging the starting material in an organic solvent, speeding up the chemical reaction through shaking or stirring, and then volatilizing the organic solvent through heating to produce solid electrolytes. In this study, we employed the solid-phase process to synthesize an argyrodite-type sulfide solid electrolyte, Li_6PS_5Cl, which is being considered for application in all-solid-state batteries for automotive use. After mixing the starting materials in an Ar atmosphere glovebox with a dew point of -70°C or lower in a molar ratio of Li_2S: P_2S_5: LiCl = 0.625: 0.125: 0.25 at.%, the precursor was prepared by the MA process using a planetary ball mill.

Figure 2(a) shows the results of crystal structure analysis by X-ray diffraction (XRD). As the precursor synthesis progresses, the peaks of Li_2S and LiCl derived from raw materials decrease, but amorphization also progresses, making it difficult to attribute the state by XRD. In other words, evaluation is done by XRD and ion conductivity measurement after crystallization by heat treatment following the MA process since XRD, which is good at evaluating crystallinity, cannot identify the development of chemical processes. If the chemical reaction is subsequently found to be insufficient during the MA process, a large amount of man-hours is required to redo the process, which reduces productivity at the manufacturing site.

Therefore, KRIJ and HORIBA have been studying a compact Raman spectrometer that enables in-line evaluation of solid electrolytes after MA. RS is an oscillatory spectroscopy method that uses Raman scattered light to evaluate materials. The scattered light includes Rayleigh scattered light with the same wavelength as the incident light and Raman scattered light with a different wavelength from the incident light due to the interaction between the incident light and the material. The wave-

length difference corresponds to the energy of the molecular vibration of the target material. The chemical bonding state can be obtained from the peak position, molecular structure information and crystal structure from the spectral shape, crystallinity from the peak half-width, and physical property information such as stress and strain from the peak position shift.

Figure 2(b) shows the results of crystal structure analysis using a compact laser Raman spectrometer manufactured by HORIBA, Ltd. The laser wavelength was 532 nm and the laser power was 3 mW. It was confirmed that the peaks derived from Li_2S and P_2S_5, which are raw materials, decrease as the precursor synthesis proceeds by MA, and the peaks derived from PS_4^{3-} tetrahedral unit of Li_6PS_5Cl appear and become sharp. Thus, RS can capture the progress of chemical reactions in MA and is a useful analytical technique in solid electrolyte synthesis.

Observation Technique for Solid Electrolytes

The crystal structure of solid electrolytes is observed using a spherical aberration corrected scanning transmission electron microscope (Cs-STEM). Since the state of solid electrolytes easily changes due to reactions with moisture, they are sampled in a glove box with a low dew point Ar atmosphere, inserted into a focused ion beam (FIB) machine while maintaining an inert gas atmosphere, and TEM samples are extracted by the cross-sectional microsampling method. The TEM sample is then thinned by FIB processing. Figure 3 shows the Cs-STEM observation results of LLZ, an oxide-based solid electrolyte. Although LLZ is an oxide, it is susceptible to electron beam damage and is easily altered, making observations at room temperature difficult. We have succeeded in taking atomic column images of LLZ by using an atmospheric non-open-cooled biaxial holder that enables crystal band axis observation by biaxial tilting, in addition to reducing thermal damage by cooling during observation.

All-solid-state Battery Electrode Prototyping and Electrode Structure Evaluation Technology

In liquid-based Li ion batteries, the electrolyte soaks into the porous electrode and an active material/electrolyte interface is formed spontaneously. In sulfide-based all-solid-state batteries, the solid electrolyte, active material, and conductivity aid must be pre-mixed and uniformly

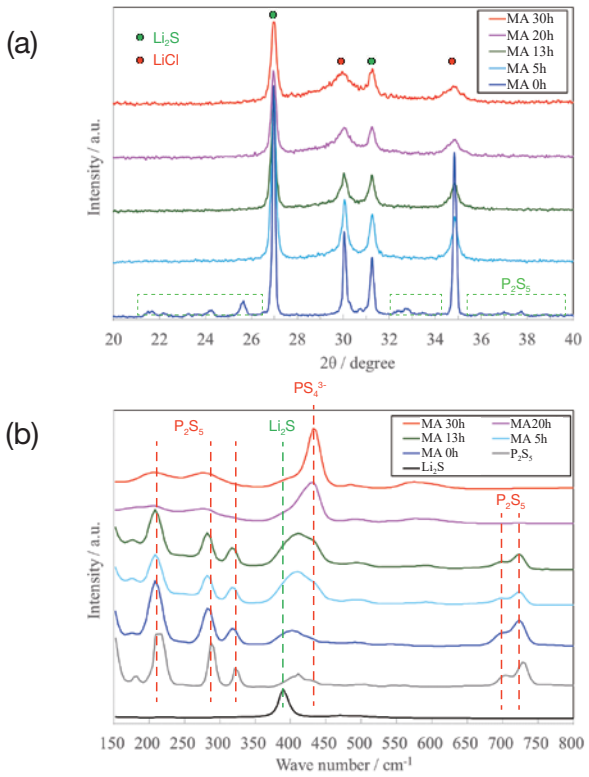

Figure 2 (a) Ion conductivity of sulfide-based solid electrolytes. (b) Crystal structure of Li_6PS_5Cl solid electrolytes.

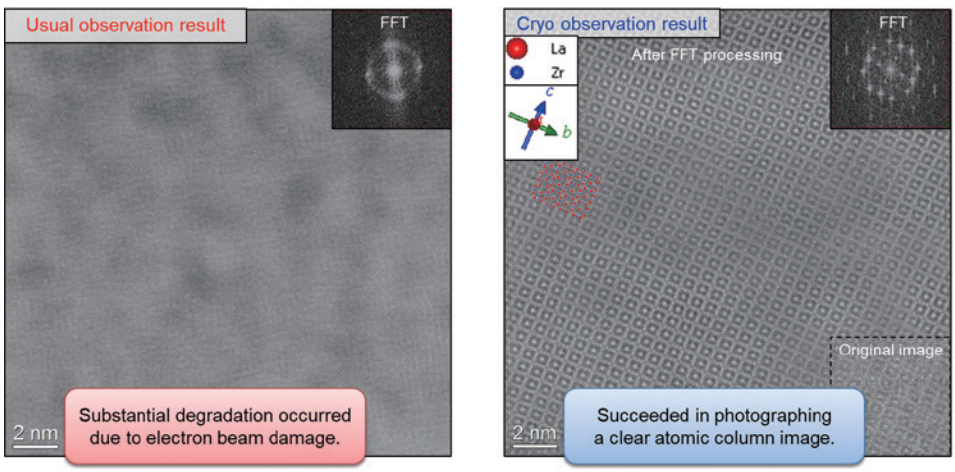

Figure 3 Cs-STEM images of $Li_7La_3Zr_2O_{12}$ solid electrolyte.

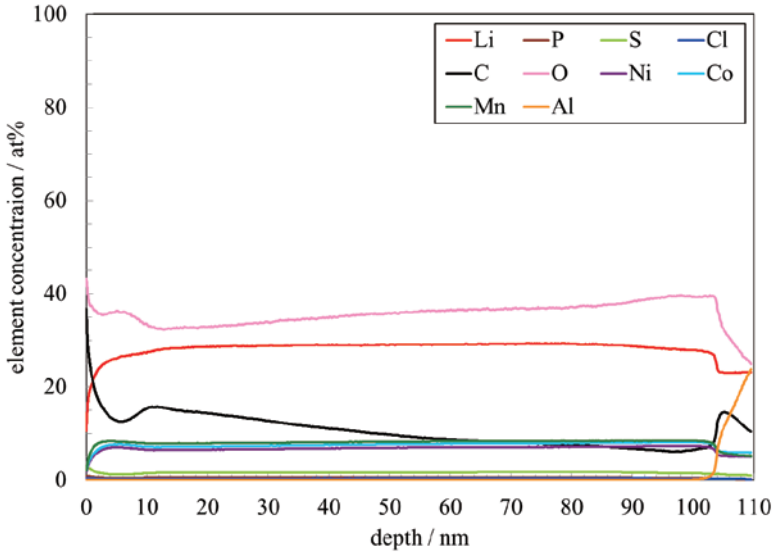

Figure 4 Depth profile analysis of cathode by GD-OES.

dispersed. In order to improve the utilization of active materials and obtain high input/output characteristics, an electrode structure with optimized electron and ion conduction pathways, respectively, is required. Therefore, the electrode is comprehensively evaluated using various analyses such as elemental analysis in the depth direction of the electrode, visualization of the three-dimensional (3D) structure of active material, solid electrolyte, and conductivity aid, and conductivity mapping.

On the other hand, from the battery point of view, small all-solid-state batteries are often used, which are made by dry mixing, pressing, and stacking of powders due to their easy manufacturing and handling methods. However, in order to conduct evaluations that more closely resemble actual use, such as cycle degradation analysis and safety evaluation, a large-capacity battery that simulates actual equipment is required. One method to fabricate large-area electrodes for high-capacity batteries is to slurry and wet-coat the electrode composite; a process similar to that used for liquid-based Li ion secondary batteries. We have fabricated a prototype of a coated sulfide all-solid-state battery by slurrying the electrode composite, coating, drying, adjusting the density by pressing, and lamination. The weight ratio of Li ($Ni_{1/3}$ $Mn_{1/3}$ $Co_{1/3}$) O_2 cathode active material with $LiNbO_3$ coating on its surface, synthesized Li_6PS_5Cl solid electrolyte, conductive aid, and binder is 74:23:3:3 wt.%. The binder and solvent were mixed, slurried, and then the coated cathode was coated and dried on the current collecting foil.

Depth elemental analysis of the coated cathode was performed by high-frequency glow discharge optical emission spectroscopy (GD-OES) using the GD-Profiler2 manufactured by HORIBA, Ltd. GD-OES was performed using a GD-Profiler2 manufactured by HORIBA, Ltd. In scanning electron microscopy-energy dispersive X-ray analysis (SEM-EDX), which is used to evaluate electrodes, it is difficult to detect Li, which is a light element, but GD-OES can detect Li emission with high sensitivity, making analysis possible. GD-OES has unique features such as a wide analysis area (e.g., Φ4 mm) and the ability to measure depths from the surface layer to 100 μm by Ar sputtering, making it a useful analysis method for depth analysis of electrodes. Electrodes were sampled in a glove box with a low dew point Ar atmosphere, transported in a transfer vessel for non-exposure to air, and set in the GD-OES. Figure 4 shows the results of elemental analysis of the coated cathode in the depth direction. For electrodes with a coating thickness of approximately 100 μm, the constituent elements Li, P, S, Cl, C, Ni, Co, Mn, and Al are captured from the surface layer to the current collecting foil, allowing evaluation of the mixing state of active materials, solid electrolytes, and binders.

The 3D structure of the electrode is analyzed using Focused Ion Beam Scanning Electron Microscopes (FIB-SEM). Across-sectional machining is performed by FIB and a cross-sectional SEM image is acquired. Then, the machined surface is further shaved and a new cross-sectional SEM image is repeatedly obtained, and a 3D construction image is obtained from multiple two dimensional (2D) cross-sectional images. The structure is further optimized by evaluating the volume ratio of each component and the contact area between components through image analysis. Since solid electrolytes are easily altered by heat during cross-sectioning, cooling processing (cryo-processing) is required to minimize thermal effects. Cross-sectional observation of all-solid-state

batteries is possible only by optimizing the observation conditions, such as low acceleration voltage and cryo-processing, in order to minimize damage to the sample.

On the other hand, from the manufacturing process perspective, it is important to understand the behavior of particles during the electrode formation and powder filling processes. The flowability and adhesiveness of solid electrolytes are very important parameters in the design of electrode mixtures and manufacturing processes. The higher the fluidity of a solid electrolyte, the better the dispersibility of the electrode during the electrode composite fabrication process. On the other hand, the higher the fluidity, the lower the adhesion required to form and maintain an interface between particles, so appropriate powder design is necessary. We have installed a powder rheometer in a dry room where flowability and shear tests can be evaluated with the same device and a relatively small amount of sample can be measured.[11]

The elastic modulus of a solid electrolyte is an important property to evaluate the ease of active material/solid electrolyte interface formation. However, it is sometimes difficult to measure the elastic modulus of the solid electrolyte itself due to the influence of the macroscopic structure of the solid electrolyte pellet by different measurement methods. We have evaluated the elastic modulus of the solid electrolyte itself by mapping the elastic modulus in a small area using scanning probe microscopy (SPM) in a low dew point Ar atmosphere glove box.

Prototyping and Evaluation Technology for All Solid-State Batteries

A coated cathode consisting of a composite of cathode active material Li ($Ni_{1/3}$ $Mn_{1/3}$ $Co_{1/3}$) O_2, synthesized solid electrolyte Li_6PS_5Cl, conductivity aid, coated anode consisting of graphite (anode active material), and solid electrolyte Li_6PS_5Cl, were placed facing each other with the solid electrolyte in between. The coated all solid-state battery was densified and an interface was formed by warm isostatic pressing (WIP).

Figure 4(a) shows the results of the discharge rate characteristic test. The voltage range was 2.0 V to 4.2 V. After constant-current and constant-voltage charging at an ambient temperature of 25°C, discharge was performed at different C rates. The output characteristics were good, with a high capacity retention rate even at 5C discharge.

Figure 4(b) shows the results of a charge-discharge cycle test at 1 C. 300 cycles resulted in a capacity retention rate of 98% and a charge-discharge efficiency of approximately 100%. Thus, 300 cycles of repeated charge-discharge at 1 C are possible, and long-term durability evaluation is possible.

Conclusion

Analytical techniques contributing to the development of materials and processes for all-solid-state batteries, which are expected to become the next-generation batteries, were introduced. Compared to liquid-based Li ion batteries, sulfide-based all-solid-state Li ion batteries are expected to have higher energy density and superior input/output characteristics. Research and development for their practical application is accelerating, especially for automotive applications. Solid electrolyte, a key material for all-solid-state batteries, requires an analysis technique for non-atmospheric exposure according to the synthesis process, and we introduced an example of evaluation using a compact Raman spectrometer in the MA process. Since all solid-state batteries are composed entirely of solid particles, the formation and maintenance of solid/solid interface and the formation of conductive paths and Li ion paths in the electrode are necessary to obtain good battery characteristics, directional analysis and depth analysis of electrode by GD-OES. Thus,

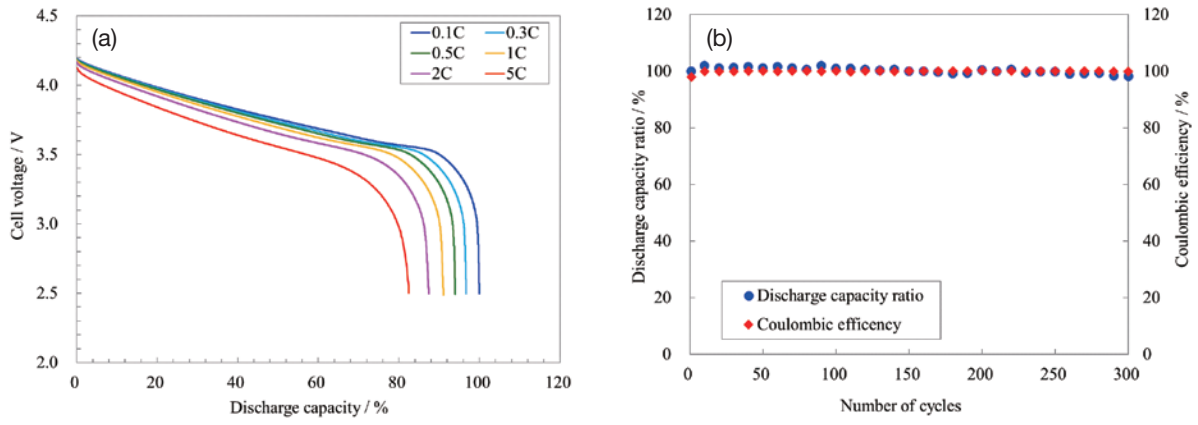

Figure 5 Electrochemical performances of solid-state battery. (a) Discharge rate performance. (b) Charge-discharge cycle performance.

evaluation of electron conduction path by SPM, etc., should be combined and evaluated comprehensively.

We will contribute to the research and development of rechargeable batteries, including all-solid-state batteries, through prototyping of rechargeable batteries, disassembly investigations using physical and chemical analysis, safety testing, and combined analyses with computational science.

References

[1] F. Mizuno, A. Hayashi, K. Tadanaga, and M. Tatsumisago: Adv. Mater. 17, 918 (2005).

[2] M. Tatsumisago, M. Nagao, and A. Hayashi, *J. Asian Ceram. Soc.*, **1** (2013) 17-25.

[3] R. Kanno, *Jpn. J. Appl. Phys.*, **90** (1), (2021) 6-23.

[4] Y. Kato, S. Hori, T. Saito, K. Suzuki, M. Hirayama, A. Mitsui, M. Yonemura, H. Iba, and R. Kanno: *Nat. Energy*, **1** (2016) 16030.

[5] N. Kamaya, K. Homma, Y. Yamakawa, M. Hirayama, R. Kanno, M. Yonemura, T. Kamiyama, Y. Kato, S. Hama, K. Kawamoto, and A. Mitsui, *Nature Materials*, **10**, (2011), 682-686.

[6] S. Boulineau, M. Courty, J.-M. Tarascon and V. Viallet, *Solid State Ionics*, **221** (2012) 1-5.

[7] H.J. Deiseroth, S.T. Kong, H. Eckert, J. Vannahme, C. Reiner, T. Zaiss, and M. Schlosser, *Angew. Chem., Int. Ed.*, **47** (2008) 755.

[8] R. Murugan, V. Thangadurai, and W. Weppner, *Angew. Chem. Int. Ed.*, **46** (2007) 7778.

[9] K. Momma and F. Izumi, J. Appl. Cryst., **44** (2011) 1272

[10] H. Muramatsu, A. Hayashi, T. Ohtomo, S. Hama, M. Tatsumisago, *Solid State Ionics*, **182** (2011)116.

[11] T. Achiha,*J. Soc. Powder Technol. (Jpn.)*, **59** (11), (2022) 575-581.

Hydrogen Concentration Measurement in Hydrogen Combustion Gas Turbine Development

TSURU Tomoko

Manager
Engine Thermal Engineering Section
Engine Technology Development Department,
Aero Engine Business Division, Aerospace Systems Company
Kawasaki Heavy Industries, Ltd.

HORIKAWA Atsushi

Manager
Section 1, Energy System Research Department
Technical Institute, Corporate Technology Division
Kawasaki Heavy Industries, Ltd.

UCHIYAMA Yuta

Section 1, Energy System Research Department
Technical Institute, Corporate Technology Division
Kawasaki Heavy Industries, Ltd.

This report introduces the efforts of Kawasaki Heavy Industries for developments of hydrogen-fueled industrial gas turbines and aircraft engines toward the realization of a decarbonized society. In the hydrogen-fueled combustor development, accurate measurement of hydrogen concentration in the exhaust gas will play more important role. Trial measurement results of hydrogen concentration using HORIBA HyEVO-1000, performed in KHI Akashi works, demonstrated favorable accuracy and time response.

Keywords: Hydrogen gas turbine, NOx, unburned hydrogen

Introduction

In the Fifth Strategic Energy Plan[1] in July 2018, it was stated that it is important to promote the development of hydrogen power generation which consumes stable and large amount of hydrogen together with the construction of international hydrogen supply chain. In October 2021, the Sixth Strategic Energy Plan[2] stated that hydrogen and ammonia power generation is one of the powerful options for decarbonizing thermal power generation to achieve carbon neutrality in 2050, and stated that the government will work to overcome technical challenges for hydrogen and ammonia power generation to function as a major supply and regulating force in the power system in 2050.
In addition, in the aircraft field, it was mentioned to promote the development of core technologies such as hydrogen combustors, which will be necessary for the realization of hydrogen aircraft after 2035.
KHI is developing and demonstrating various technologies for the production, transportation, storage and utilization of hydrogen to build an international hydrogen supply chain as shown in Figure 1[3]. Specifically, it is a comprehensive development and demonstration project that liquefies hydrogen produced from brown coal and renewable energy, transports and stores it, and uses it in gas turbines as a fuel to replace hydrocarbon fuels.
This report introduces KHI's efforts in the development of hydrogen combustors for industrial gas turbines and aircraft engines, and describes the measurement of hydrogen gas concentrations required for these developments. Finally, as an example of hydrogen concentration measurement in the development of hydrogen combustors for aircraft engines, the application of the hydrogen gas measuring device HORIBA HyEVO -1000 is introduced.

Challenges of hydrogen combustion

Comparison of combustion characteristics between

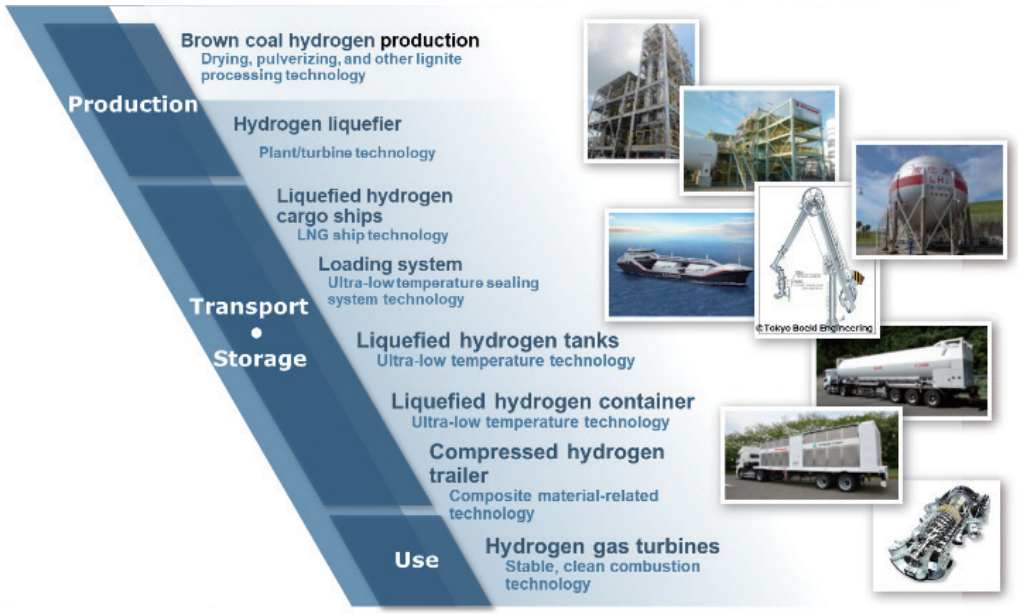

Figure 1 Technology developments for Hydrogen Society in Kawasaki Heavy Industries, Ltd.

hydrogen and methane, a major component of natural gas, and problems specific to hydrogen combustion are shown in Table 1. The maximum combustion speed of hydrogen is faster than that of methane, and the quenching distance is smaller. Therefore, the hydrogen flame tends to get close to the metal parts of the combustor, causing oxidation and damage from overheating. In addition, since hydrogen increases the combustible range, premixed combustion increases the risk of flashback.

Moreover, high combustion speed and flame temperature produce locally hot combustion gas, leading to increased NOx (nitrogen oxides) emissions. Considering these unique combustion characteristics of hydrogen, the development of a combustor with stable combustion of hydrogen and low NOx properties is required.

On the other hand, hydrogen, which is more reactive than conventional hydrocarbon fuels, has the advantage that it is rarely discharged unburned. It has been confirmed in KHI's combustion tests that unburned hydrogen is not generated in the stable combustion state of the gas turbine. However, unburned hydrogen is generated under unstable combustion conditions, rich conditions, and transient conditions such as load changes, ignition and extinguishment. It is important to know whether unburned hydrogen is generated and its concentration in the process of development, because it must be avoided that unburned hydrogen is deposited downstream of the combustor, leading to unintended combustion and explosion.

Table 1 Combustion characteristics of methane and hydrogen and problems with hydrogen combustion

Combustion characteristics	CH_4	H_2	Hydrogen problems in hydrogen combustion burning rate [m/s]
Combustion speed [m/s] (Stoichiometric mixture ratio, 0.1 MPa)	0.4	2.65	Abnormal combustion (flashback, combustion oscillation)
Quenching distance [mm]	2.2	0.64	Oxidation and damage of metal parts due to overheat
Flammability limit [Vol%]	5～15	4～75	Abnormal combustion (flashback)
Flame temperature [degC] (in the air)	1875	2045	Thermal NOx increase

Micro-mix Hydrogen Combustion Technology and Industrial Gas Turbine Demonstration Test

KHI focused on the micro-mix hydrogen combustion technology which Aachen University Applied Sciences (AcUAS) owns. This technology makes micro hydrogen flames and dry low NOx emissions. In collaboration with B&B-AGEMA, the application to industrial gas turbine combustors was investigated and a conceptual design for the combustor was carried out [4-6].

Figure 2 (a) shows a conceptual diagram of the micro-mix combustion to enable dry low NOx combustion technology, and Figure 2 (b) shows an example of numerical simulation of combustion flow field[7]. Hydrogen is injected through a minute injection hole and rapidly mixed with an orthogonal air jet to form a hydrogen flame. By forming a small hydrogen flame, the generation of the local high temperature region is eliminated and the generation of NOx is suppressed by shortening the reaction time.

In the shear zone behind the hydrogen injection hole and between the recirculation zone formed behind the air

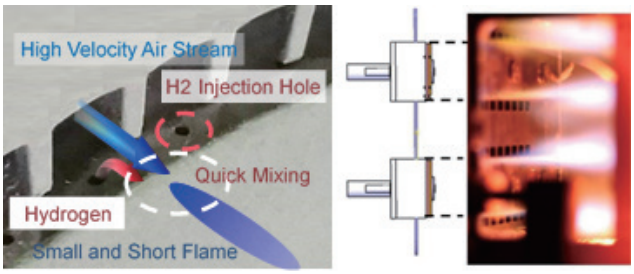

Figure 2(a) Micro-mix hydrogen flame.

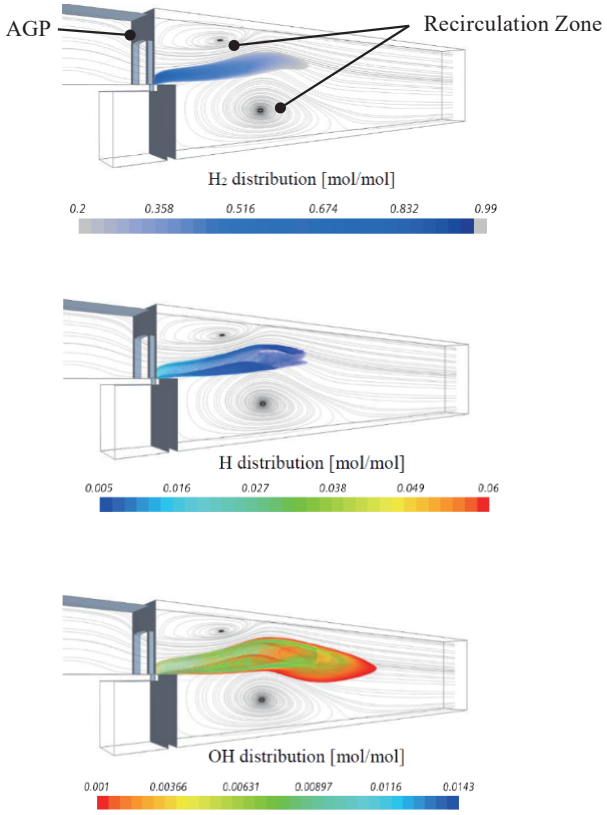

Figure 2(b) Structure of hydrogen flame and flame holding (Examples of CFD analysis).

guiding panel (AGP) and the hydrogen supply unit, OH radicals and H atoms are generated and the hydrogen flame is stabilized. Therefore, the penetration of hydrogen flame into the hydrogen supply unit and flashback to the upstream side of the AGP do not occur.

Industrial gas turbines in KHI use reverse flow can type combustors. Therefore, the rectangular micro-mix burner used in the hydrogen combustion test at AcUAS was formed into a ring shape to fit the shape of the can type combustor. Figure 3 shows the configuration of a combustor equipped with a micro-mix burner module (initial concept stage) [8]. In 2020, KHI succeeded in the technology demonstration test of the world's first dry low-NOx hydrogen combustion gas turbine using a micro-mix burner in a grant project of New Energy and Industrial Technology Development Organization (NEDO)[9].

The move to decarbonize aircraft engines

In recent years, in addition to fuel cells and Sustainable Aviation Fuel (SAF), there has been a growing momentum toward the realization of carbon neutrality in the aviation industry. Since 2020, when Airbus in France started a hydrogen aircraft development project, aiming to start operation in 2035[10], efforts for hydrogen conversion have been intensified in various fields such as engines, aircraft equipment, and infrastructure development in airports.

KHI started development of core technologies for a hydrogen aircraft in fiscal year 2021, which is expected to make a significant contribution to decarbonization as a part of NEDO Green Innovation funding project [11]. The target aircraft has a route distance of 2,000 - 3,000 km and a passenger capacity of about 200 passengers. Combustors and engine fuel systems, liquefied hydrogen fuel tanks and equipment systems, and structural study of airframe will be set as core technologies. Development of each component will be promoted until FY 2028. In the FY 2029 to 2030, KHI will conduct end-to-end ground demonstration tests by integrating them, aiming to demonstrate key technologies for social implementation of hydrogen aircraft.

In the development of combustors for aircraft engines, as well as industrial gas turbines, high environmental compatibility is required, and strict regulations have been

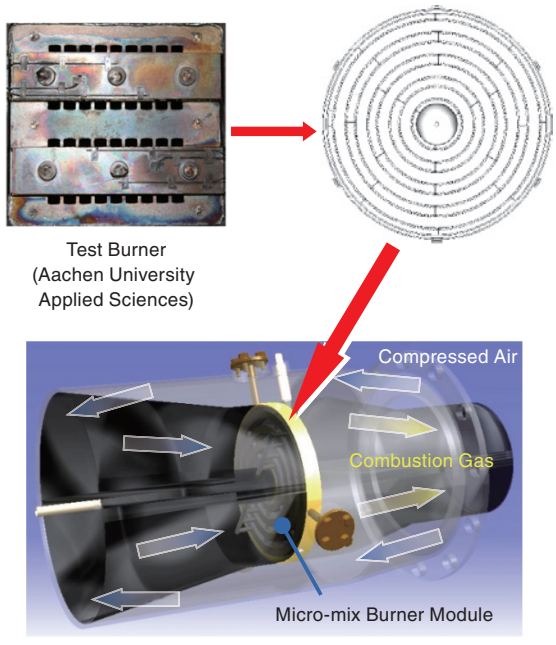

Figure 3 Schematic view of the first conceptual design of hydrogen Dry Low Emission combustor with micro-mix burner module.

established by ICAO (International Civil Aviation Organization). Decarbonizing aviation engines can greatly contribute to reducing environmental impact in terms of CO_2 and smoke, but the generation of NOx and water vapor can not be avoided. In particular, the pressure inside an aircraft engine is higher than that of an industrial gas turbine, making it difficult to reduce NOx emissions. In addition, since the power fluctuation during operation is large and rapid, the development of a combustor that can reduce the emission of harmful substances while keeping up with the changes in combustion conditions will be very important for the practical use of hydrogen aircraft.

Unburned hydrogen concentration measurement in gas turbine combustor development

As mentioned in the introduction, unburned hydrogen is hardly generated if hydrogen burns stably with a wide combustible range. However, when the engine is under low load or the transient state, the unstable combustion tends to occur and causes the generation of unburned hydrogen. In particular, aircraft engines have a risk of generating a large amount of unburned hydrogen temporarily because the air flow rate, pressure, and air excess rate change significantly in a short time compared to industrial gas turbines.

In the development of hydrogen combustors, not only the aforementioned reduction of NOx emissions during stable combustion, but also combustion efficiency above a certain level must be ensured even during low-load and transient operations. Therefore, both responsiveness (about 0.5 seconds) and accuracy (resolution on the order of several ppm) are required for measuring instruments in development tests.

Trial Measurement of unburned hydrogen concentration for aeroengine hydrogen combustor using HyEVO-1000

KHI is planning to introduce the HORIBA HyEVO-1000, which is scheduled to go on sale in 2023, as a device that can measure hydrogen concentration accurately in real time for aviation engine combustors. In preparation for the installation, a trial measurement with a demonstration machine was carried out in December 2022.

Figure 4 shows the appearance of the test apparatus. Hydrogen gas is injected from a fuel nozzle located in the combustor casing through a fuel manifold, and forms flames in an annular inner cylinder called a liner. Exhaust gas is sampled from the combustor outlet and fed through a

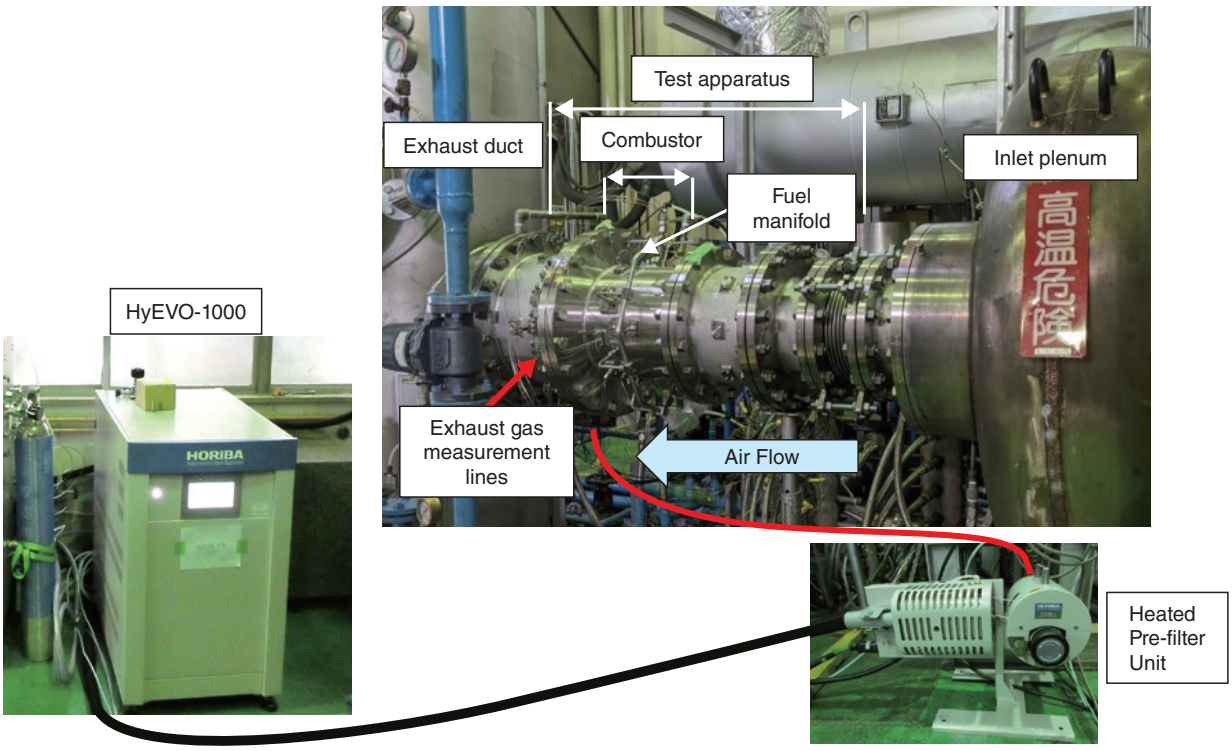

Figure 4 Test apparatus of hydrogen combustor for aeroengine.

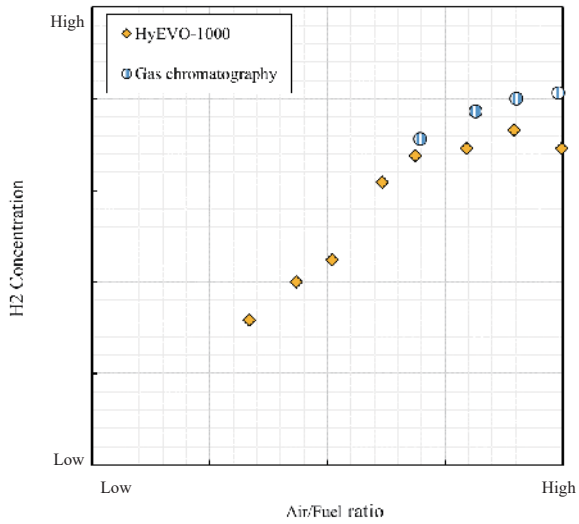

Figure 5 Comparison of hydrogen concentration between HyEVO-1000 and gas chromatography.

heating filter to the densitometer body. To verify the measured data, hydrogen concentration measurements by gas chromatography were also performed in parallel.

Figure 5 shows a comparison of hydrogen concentration measured by HyEVO-1000 with that measured by gas chromatography. In a series of air-fuel ratio conditions, both showed good agreement, and it was confirmed that the hydrogen concentration could be measured accurately. It was also responsive, and the combustion test was carried out smoothly.

Summary

KHI's efforts in the development of hydrogen combustors for industrial and aviation gas turbines are introduced, and the expected role of hydrogen concentration measurement for the development of combustors is described with an introduction of hydrogen concentration measurement examples using HyEVO-1000. It is expected that effective utilization of the high measurement capability not available in conventional measuring instruments will lead to the promotion of development of hydrogen combustors.

Considering that decarbonization by hydrogen utilization will become more active in the future, demand for hydrogen concentration measurement is expected to increase in various fields. From the user's point of view, not only the measurement capability but also the ease of handling and cost of the equipment are important points, and there are much to be expected such as further compactness, quiet structure, and adaptability to flexible operating range. It is expected that if manufacturers and users can cooperate with each other to realize more advanced and easy-to-use measuring instruments, they can greatly contribute to the demonstration of future technologies to reduce environmental impact.

Acknowledgement

Demonstration of hydrogen powerplant and cogeneration system with hydrogen-fueled dry NOx combustor was conducted in the framework of NEDO Technology Development Project for Building a Hydrogen-based Society / Technology Development Project for Large-Scale Utilization of Hydrogen / Development and Demonstration Project for Low-NOx Hydrogen-fueled Gas Turbine Combustion Technology.

The hydrogen combustor development for aircraft engine is also supported by NEDO in Green Innovation Fund Project. The authors acknowledge NEDO for their financial support in both projects.

References

[1] National Diet Library Internet Materials Collection and Preservation Project, the Ministry of Economy, Trade and Industry News Release Website; *A new Basic Energy Plan has been approved by the Cabinet.* https://warp.da.ndl.go.jp/info:ndljp/pid/11126101/www.meti.go.jp/english/press/2018/0703_002.html(accessed February 20, 2022)

[2] Ministry of Economy, Trade and Industry News Release Website; *The Sixth Basic Energy Plan has been approved by the Cabinet,* https://www.meti.go.jp/english/press/2021/1022_002.html(accessed October 25, 2021)

[3] Motohiko Nishimura, Kentaro Mizumuki, Seiichi Sugawa; Current status of technology construction in the international liquefied hydrogen supply chain, *Journal of the Japanese Society of Energy and Resources,* Vol. 229, Vol. 39 No. 3, (2018), 153-157.

[4] Funke, H., et al; Numerical and Experimental Characterization of Low NOx Micromix Principle for Industrial Hydrogen Gas Turbine Applications, *Proceedings of ASME Turbo Expo 2012,* Copenhagen, Denmark, GT2012-69421.

[5] Funke, H., et al; Experimental and Numerical Characterization of the Dry Low NOx Micromix Hydrogen Combustion Principle at Increased Energy Density for Industrial Hydrogen Gas Turbine Applications, *Proceedings of ASME Turbo Expo 2013,* San Antonio, Texas, GT2013-94771.

[6] Haj Ayed, A., et al; Numerical Study on Increased Energy Density for the DLN Micromix Hydrogen Combustion Principle, *Proceedings of ASME Turbo Expo 2014,* Dusseldorf, Germany, GT2014-25848.

[7] Kroniger, D., et al.; Numerical Study of Hydrogen-fuelled Micromix Combustion and Experimental Validation of NOx Emissions, *48 Annual Lectures of the Gas Turbine Society* (held online), A -14, (2020)

[8] Atsushi Horikawa and others; Development of dry hydrogen low NOx combustion technology, *43 Annual Lecture of the Gas Turbine Society (Yonago),* Collected Lectures A -7, (2015)

[9] NEDO News Release Website; *World's first successful technology demonstration test of dry low NOx hydrogen combustion gas turbine* https://www.nedo.go.jp/news/press/AA5en_100427.html, (accessed February 20, 2023)

[10] https://www.airbus.com/en/innovation/zero-emission/hydrogen/zeroe (accessed February 27, 2023)

[11] NEDO News Release Website; *Green Innovation Fund project begins research and development on next-generation aircraft -Aiming to establish core technology for hydrogen aircraft and drastically reduce weight of key structural components* https://www.nedo.go.jp/news/press/AA5_101488.html (in Japanese, accessed February 27, 2023)

Development of a Gas Analysis Technology "IRLAM" Using Quantum Cascade Laser and Unique Concentration Calculation Method

~ Realization of High-Sensitivity, Low-Interference, and Fast-Response Gas Analysis ~

SHIBUYA Kyoji

HORIBA's newly developed gas analysis method using a quantum cascade laser (QCL), infrared laser absorption modulation (IRLAM), dramatically reduces calculation time compared to conventional spectral fitting methods by extracting information important for concentration determination from the absorption signal of the sample gas as features (patent registered). By combining this method with QCLs manufactured in-house and a uniquely structured Herriott cell with a small volume and long optical path length, we have completed a gas analyzer with high sensitivity, small influence of interfering gases, and fast response. IRLAM has succeeded in greatly expanding the industrial application range of gas analysis using QCL, realizing the world's first QCL-based onboard exhaust gas measurement and real-time monitoring of petrochemical processes.

Keywords
gas analysis, infrared absorption spectroscopy, quantum cascade laser, spectral analysis, features

Introduction

HORIBA has long applied gas analysis technology using infrared absorption to automotive and factory exhaust gas measurement, atmospheric environment measurement, and process monitoring and control, and has contributed to reducing environmental impact and improving productivity in various industrial fields. A conventional infrared gas analysis technique called non-dispersive infrared absorption (NDIR) has been widely used.[1] NDIR uses thermal radiation from a light source such as a heated filament, cuts out the wavelength band to be used with an optical bandpass filter to match the absorption band of the target gas and determines the concentration of the target gas from the amount of absorbed infrared light. Because the wavelength resolution of the light source is not high in NDIR, it is difficult in principle to remove the influence of interfering gases whose absorption bands overlap with those of the target gas. Therefore, the use of a pneumatic detector[2] that detects infrared light in a cell filled with the target gas can provide a certain degree of gas selectivity. The gas analysis method using Fourier transform infrared spectroscopy (FT-IR) can acquire the absorption spectrum of the entire infrared region of a sample gas. This makes it possible to simultaneously measure many gas components by applying multivariate analysis. The FT-IR method is widely used for automotive emission gas measurements.[3] On the other hand, quantum cascade laser infrared spectroscopy (QCL-IR), a gas analysis method using a single wavelength quantum cascade laser (QCL) as a light source, can considerably suppress the interfering gas influences by selecting a suitable wavelength for the measurement with high wavelength resolution. Moreover, the QCL-IR method can provide higher sensitivity than NDIR and FT-IR because of the high energy density per unit wavelength of the light source and the straightness of the laser beam facilitating the use of a multipass cell to obtain a long optical length. HORIBA was the first company in the world to apply gas analyzers using QCL-IR to automotive emission gas measurements.[4,5] However, in applications such as automotive emission gas measurement, where many interfering gases coexist and their concentrations change dynamically, it is difficult to completely eliminate interfering gas influences by wavelength selection alone. In conventional QCL-IR, the concentration of the target gas corrected for interfering gas influences is calculated by curve fitting between the measured absorption spectrum of the sample gas and the model spectra of the target gas and interfering gases prepared in advance. In addition to interfering gas influences, various other disturbances such as fluctuations in environmental temperature and pressure, drifts in laser oscillation wavelength, and spectral broadening due to interactions with coexisting gases can change the absorp-

tion spectrum. Since a complex fitting process involving repetitive operations is required when these nonlinear disturbances are included in the correction, a high-performance and bulky computer has to be installed in the equipment to perform such operations in real time. However, such requirements not only increase the cost and size of the device, but also limit the scope of application for industrial instruments, which are required to operate stably even in harsh environments.

To address this, we came up with the idea of applying the concept of "features" used in a field such as machine learning to the QCL-IR concentration calculation algorithm. By extracting features of target gas, interfering gas and other disturbances from the absorption signal obtained in the measurement, the number of explanatory variables is greatly reduced while maintaining the amount of information necessary for concentration quantification. Thereby the load on the concentration calculation process is dramatically reduced. This has made it possible to achieve sufficiently high-accuracy and real-time measurement with even a board-embedded general-purpose microcomputer while eliminating various disturbances that affect the measurement accuracy. We have named this gas analysis method Infrared Laser Absorption Modulation (IRLAM[TM*1])[6] and have successfully commercialized a gas analyzer based on this principle. The following describes the principle and configuration of IRLAM, compares it with conventional technologies, and introduces examples of products in which IRLAM has been applied.

*1: IRLAM is a registered trademark or trademark of HORIBA, Ltd. in Japan and other countries.

Principle and configuration of IRLAM

Gas analysis by absorption spectroscopy, including IRLAM, uses a basic principle based on Lambert-Beer law that the absorbance A, defined as the logarithm of the ratio of the incident light intensity I_{in} to the sample gas and the transmitted light intensity I_{out} is proportional to the gas concentration c and the optical path length L, which is expressed by the following equation.

$$A = -\log\left(\frac{I_{out}}{I_{in}}\right) = \varepsilon \cdot c \cdot L$$

Here, ε is a gas-specific constant called the absorption coefficient.

Figure 1 shows a schematic diagram of the basic configuration of an IRLAM gas analyzer. In the IRLAM gas analyzer, a light from the QCL is incident on an analysis cell into which sample gas is introduced, called a Herriott cell, and the emitted light after transmission through the sample gas is received by an infrared detector to acquire absorption signals. The concentration of the target gas is then calculated from the obtained absorption signal using a unique concentration calculation algorithm with feature extraction. There are three important elements that characterize the IRLAM gas analyzer: the QCL, the Herriott cell, and the concentration calculation algorithm, each of which is described below.

Quantum cascade laser

QCLs are a relatively new type of semiconductor lasers capable of room-temperature laser oscillation in the mid-infrared region (with wavelengths ranging from 4 to 12 μm).[7] Since most gas molecules show the strongest absorption in the mid-infrared region, the QCL, which can oscillate in this wavelength region, is the most suitable light source for gas analysis. A QCL consists of a multilayer semiconductor thin film with several hundred layers, and its feature is that the oscillation wavelength can be arbitrarily designed by controlling the material composition and film thickness. HORIBA has established the technology to manufacture QCLs in-house with optimal wavelengths according to the type and concentration range of the target gas. This enables to flexibly response to a variety of gas analysis needs.

Herriott Cell

In gas analyzers using absorption spectroscopy, the longer the distance that light penetrates the sample gas (optical path length), the greater the absorbance and the higher the sensitivity, as shown by Lambert-Beer law. Therefore, the IRLAM gas analyzer employs a gas cell called Herriott cell, as shown in Figure 1, in which light is multiply reflected by opposing mirrors installed inside to obtain a long optical path length.

Conventional Herriott cells generally use circular spherical mirrors,[8] but we use elongated spherical mirrors to significantly reduce the internal volume of the cell while ensuring a sufficient optical path length.[9] Reducing the internal volume of the cell improves the response time of

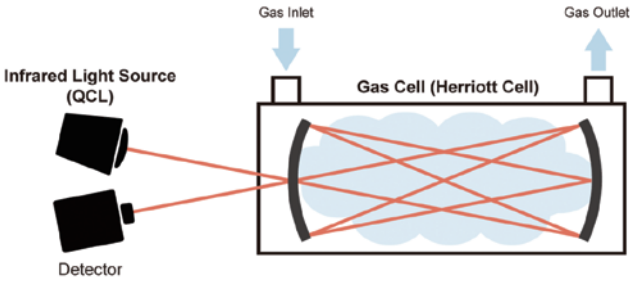

Figure 1 Schematic diagram of the basic configuration of the IRLAM gas analyzer.

the analyzer, which is dictated by the gas displacement time. In the Herriott cell with the elongated spherical mirrors, a 5 m optical path length can be achieved with an internal volume of only 40 mL. This contributes to the improved response time and the downsizing of the IRLAM gas analyzer.

Concentration calculation algorithm

The most distinctive element of the IRLAM gas analyzer is the concentration calculation algorithm.

IRLAM's concentration calculation algorithm applies the concept of "features" used in a field such as machine learning. Figure 2 shows a schematic of the gas analysis procedure in IRLAM. When the wavelength of QCL is modulated at a certain period around a peak of the absorption spectrum of the target gas, a periodic absorption signal reflecting the shape of the absorption spectrum is obtained from the detector. By correlating this absorption signal with multiple reference signals prepared in advance according to the features to be extracted, features quantities are extracted, and the obtained feature quantities are compared with the reference feature quantities obtained in advance using the calibration gas to determine the concentration using the least-squares method.[6,10]

In machine learning, the algorithm automatically determines the features to be extracted by learning from a large amount of training data, but in IRLAM, the designer selects the factors important for concentration quantification based on experience and determines the features to be extracted by understanding their influences on the absorption signal based on their physical properties. Specific factors important for concentration determination include the shape of the absorption signal of the target gas and the interfering gases, the influence of QCL oscillation wavelength drift, and the influence of spectral broadening caused by changes in pressure or coexisting gas concentration. In actual gas analysis applications of IRLAM, concentration quantification is performed using about 10 features related to these factors.

The advantage of the concentration calculation procedure using features is that by compressing spectral information through feature extraction, concentration calculations with correction functions for interference gas influences and other disturbance can be performed with significantly fewer explanatory variables than in the conventional case of direct curve fitting to absorption spectra. In general spectral curve fitting, since absorption spectral data consists of several hundred points, it is necessary to perform a least-squares method consisting of several hundred simultaneous linear equations. In the case of IRLAMs, on the other hand, the number of simultaneous linear equations is only a few to 10, so the computational load is reduced to 1/10 to 1/100. Therefore, even when high-speed real-time measurement is required, a high-performance computer is not necessary; a general-purpose embedded processor is sufficient. This allows the IRLAM to be configured without the need for a PC, facilitating downsizing and expanding its range of applications as an industrial instrument capable of stable and continuous operation even in harsh environments.

Performance comparison between IRLAM and conventional technologies

IRLAM has significantly improved from conventional gas analysis technologies using infrared absorption in terms of detection sensitivity and interference gas influence. The following is a comparison between IRLAM and conventional technologies based on specific measurement examples.

Detection sensitivity

Figure 3 compares the results of simultaneous measurement of formaldehyde (HCHO) in automotive exhaust gas by an IRLAM gas analyzer and a conventional FT-IR gas analyzer. The red line shows the FT-IR measurement results, and the blue line shows the IRLAM measurement results. The right figure shows that the overall trend of concentration change is consistent between the two methods. However, it can be clearly seen that the magnitude of the noise is very different. As shown in the left figure, which is an enlarged version of the right figure, the noise of IRLAM is less than one-tenth that of FT-IR. IRLAM can accurately measure even slight concentration

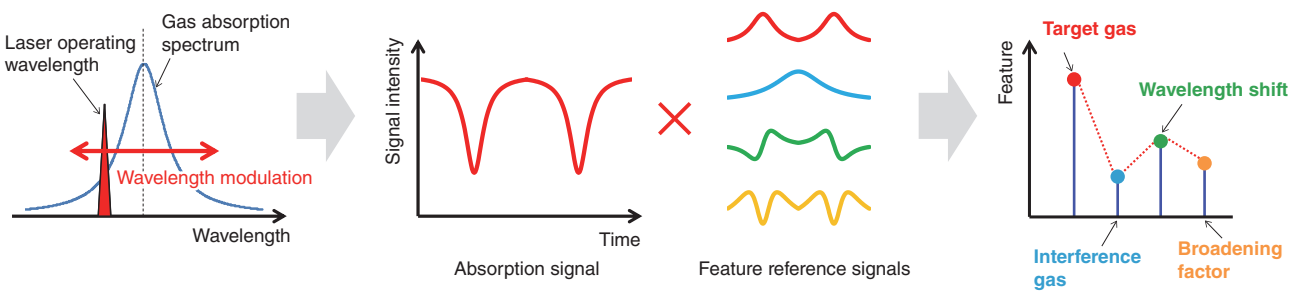

Figure 2 Conceptual diagram of the gas analysis procedure in IRLAM.

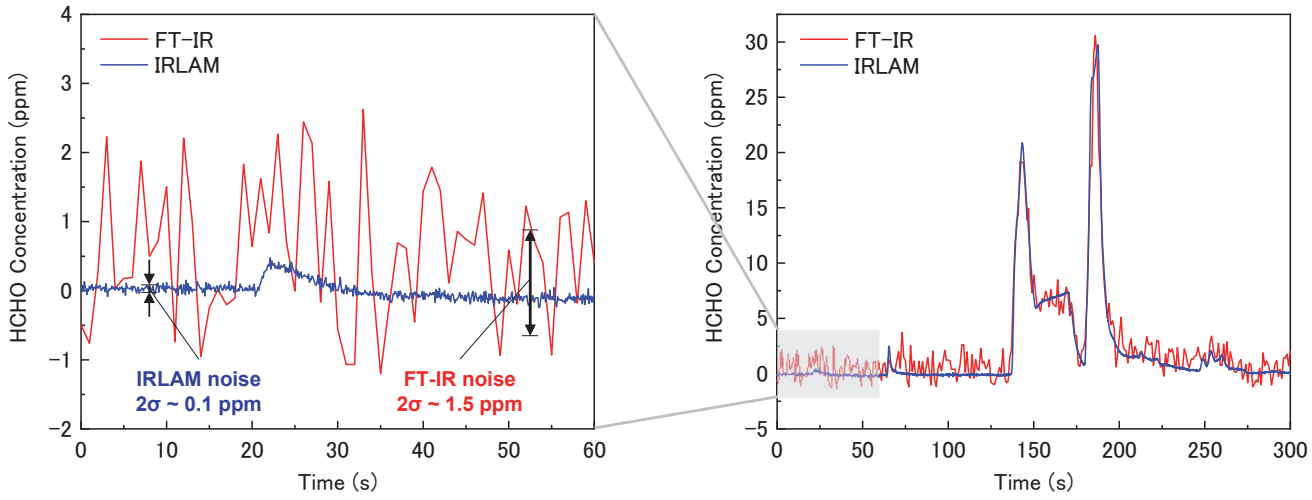

Figure 3 Comparison of detection sensitivity between IRLAM and FT-IR for HCHO measurement (the left figure is enlarged from 0 to 60 s in the right figure).

changes that is undetectable with FT-IR because they are buried in noise. Thus, IRLAM showed more than 10-fold improvement in detection sensitivity compared to conventional FT-IR.

Interfering gas influence

Figure 4 compares the changes in the concentration readings of an IRLAM gas analyzer and a conventional NDIR gas analyzer when the target gas, dinitrogen monoxide (N_2O), and the interfering gas, carbon dioxide (CO_2), were introduced into the analyzer cell in sequence. The red line graph in the left figure shows the measurement result by NDIR, and the blue line graph in the right figure shows the measurement result by IRLAM. The NDIR measurement result on the left shows that the concentration readings change significantly not only when N_2O, the target gas is introduced, but also when CO_2, the interfering gas, is introduced. This indicates that the concentration of N_2O cannot be measured correctly when CO_2 is mixed with the sample gas because it is greatly affected by the interfering gas of CO_2. On the other hand, the IRLAM measurement result shown on the right indicates that no interfering gas influence was observed, even though CO_2 was introduced at a concentration 10 times higher than in the NDIR test. This shows that the IRLAM can accurately measure the concentration of N_2O even when CO_2 is mixed at high concentration. Thus, IRLAM has achieved almost zero interfering gas influences, which was not possible with conventional NDIR technology.

Examples of products to which IRLAM is applied

IRLAM with the features described above are already used in fields requiring highly accurate, real-time measurement, such as automotive exhaust gas measurement and petrochemical processes. In the following, we will introduce some of the IRLAM gas analyzers that are currently in the market.

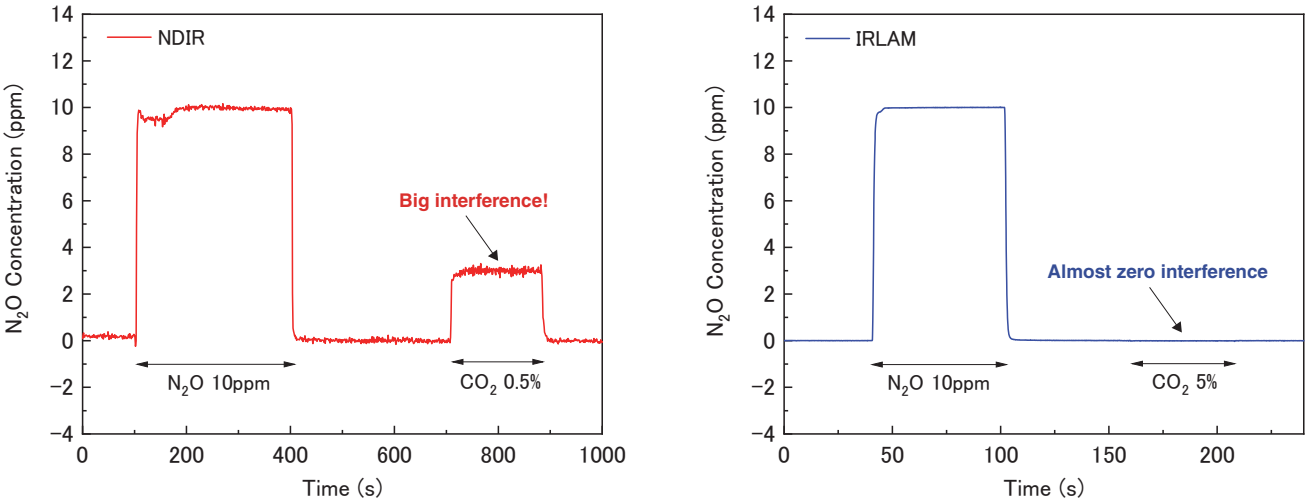

Figure 4 Comparison of interfering gas influence between IRLAM and NDIR for N_2O measurement (left: NDIR, right: IRLAM).

Engine Exhaust Gas Analyzer, MEXA-ONE IRLAM

MEXA-ONE IRLAM is an IRLAM gas analyzer for stationary automotive exhaust gas measurement. The lineup includes a type installed in the MEXA-ONE engine exhaust gas analyzer (XLA-11, XLA-13H) and a standalone unit type (MEXA-ONE-XL-NX), which are used for exhaust gas certification testing of completed vehicles and research and development to improve the environmental performance of engines.

The XLA-11 is designed to measure N_2O, a regulated greenhouse gas, with ppb-level measurement accuracy for dilution measurements using a constant volume sampling system, which is a certified test method. The MEXA-ONE-XL-NX can simultaneously measure four nitrogen compounds (NO, NO_2, N_2O, and NH_3) in real time with high accuracy, including nitrogen oxides (NOx), which have long been regulated substances, and ammonia (NH_3), which has recently been attracting attention as one of the substances causing PM2.5. It is widely used by automobile manufacturers and others as an indispensable product for the development of low environmental impact vehicles.

The XLA-13H is designed to measure HCHO, a hazardous substance that is already regulated in the United States and other countries and is being considered for regulation in Europe, and enables highly accurate continuous measurement in automotive exhaust gas test cycles, which has been difficult with conventional technology.[11] This product was also evaluated by the Joint Research Centre (JRC) of the European Commission, which provides guidelines for emission control and other policies in Europe, and its performance was shown to be sufficient for actual emission gas measurement.[12]

Onboard Emissions Measurement Systems, OBS-ONE IRLAM

In recent years, the real driving emission (RDE) regulation which measures emissions while driving on a real road has been introduced in Europe. In order to perform RDE testing, a compact and environmentally resistant analyzer called a Portable Emission Measurement System (PEMS) is required. In particular, unlike analyzers in a laboratory, on-board analyzers must be able to perform stable measurements even under severe environmental conditions, such as severe vibration and fluctuations in temperature and atmospheric pressure. IRLAM's highly robust concentration calculation algorithm and robust hardware design enabled us to meet such stringent requirements, and we succeeded in commercializing the world's first QCL-based gas analyzer dedicated for onboard emissions measurement (OBS-ONE-XL). Figure 5 shows a photograph of the OBS-ONE-XL.

In this product, N_2O and NH_3, which are under consideration for introduction in the next European automotive emission regulation Euro 7, are the measurement targets. Thanks to the aforementioned compact Herriott cell using a elongated spherical mirror and PC-free concentration calculation algorithm, the product is compact enough to withstand onboard use.[13] The product then attracted the attention of the JRC of European Commission and was evaluated for consideration for Euro 7. The results showed good correlation with stationary analyzers and sufficient performance for practical use as a PEMS.[14,15]

Process Laser Gas Analyzer, PLGA-1000

The PLGA-1000 is an IRLAM gas analyzer for real-time monitoring and control of petrochemical processes. Figure 6 shows a photograph of the analyzer. In the past, process monitoring using gas chromatography (GC) has been the mainstream, but GC lacks real-time performance, resulting in delays in detecting process abnormalities, which in some cases can lead to large raw material losses and reduced productivity. Therefore, a more real-time measurement method was required. However for the petrochemical process, it was difficult to measure with methods other than GC that do not involve gas separation because the influences of interfering gases and broadening are strong due to the presence of many hydrocarbons at high concentrations.

Figure 5 Photograph of the on-board emission measurement system, OBS-ONE-XL.

Figure 6 Photograph of the petrochemical process gas analyzer, PLGA-1000.

In spite of such difficult gas conditions, it has been demonstrated that PLGA-1000 can accurately measure the target gas in real-time by eliminating influences of the interfering gases and broadening with its unique concentration calculation algorithm. This achievement has been recognized by a major petrochemical manufacturer, which has adopted the PLGA-1000 to measure impurities such as acetylene (C_2H_2) in the ethylene (C_2H_4) production process.

Contribution to a carbon neutral society with IRLAM

Various applications of the IRLAM gas analysis technology are being considered for the utilization of carbon-neutral alternative energy sources centered on hydrogen. For example, when hydrogen is used in fuel cells, there is a demand to control impurities in hydrogen at the ppm to ppb level during hydrogen production and use because impurities in hydrogen affect the performance and life of fuel cells. In addition, direct combustion of hydrogen and NH_3, one of the hydrogen carriers synthesized from hydrogen, as a carbon-free fuel is being considered for utilization. When hydrogen and NH_3 are combusted, CO_2 is not generated, but NOx and unburned NH_3 can be emitted, so combustion control is important to suppress these emissions. Furthermore, in the Carbon Capture and Utilization (CCU) initiative to achieve carbon neutrality by capturing and reusing emitted CO_2, gas analysis plays an important role in controlling the purity of the captured CO_2 for reuse and in controlling the methanation process to synthesize methane (CH_4), which is useful as energy, from the captured CO_2 and hydrogen. IRLAM can provide solutions to these requirements and challenges through high-sensitivity and low-interference continuous gas analysis.

Conclusion

As described above, IRLAM has realized highly accurate real-time measurement under difficult conditions to measure with conventional technologies by using a QCL manufactured in-house as a light source, a Herriott cell with a unique structure and an original concentration calculation algorithm based on the feature extraction from the absorption signal. As the result, IRLAM has succeeded in greatly expanding the industrial application range of gas analysis using QCL.

The features of IRLAM can be summarized as follows

(1) High sensitivity and low interference: The fundamental features of QCL-IR and our unique concentration calculation algorithm enable highly sensitive measurement without being affected by various interfering gases contained in the sample gas.

(2) Direct and real-time: No sample gas pretreatment is required. Highly accurate real-time measurement is possible due to fast gas displacement by the small volume Herriott cell and fast concentration calculation algorithm.

(3) High stability and reliability: The unique concentration calculation algorithm and robust hardware design enable stable and accurate measurements even in harsh operating environments (large temperature and pressure fluctuations, large vibrations).

IRLAM is expected to continue to meet the gas analysis needs of all industries and contribute significantly to reducing the environmental impact of each industry, improving productivity, and realizing a carbon-neutral society. Readers who wish to deepen their understanding of the details discussed in this paper are referred to a review article[16] in which the author comprehensively summarizes the IRLAM technology.

*Editor's note: Unless otherwise indicated, the information in this article is based on our own research as of the year of publication of this article.

References

[1] Kozo Ishida: Development of Infrared Gas Analyzer, *Readout*, vol.32, 60 (2006).

[2] Junji Aoki: Pneumatic Infrared Detector, *Readout*, vol.7, 64 (1993).

[3] M. Adachi et al.: Automotive Emission Analyses using FTIR Spectrophotometer, *SAE Technical Paper*, 920723 (1992).

[4] Kenji Hara: Mid-Infrared Laser Absorption Method Automotive Exhaust Gas Analyzer, QL-N_2O, *Readout*, vol.43, 65 (2014).

[5] K. Hara et al.: Development of Nitrogen Components Analyzer Utilizing Quantum Cascade Laser, *SAE Technical Paper*, 2009-01-2743 (2009).

[6] K. Shibuya et al.: High-sensitivity and low-interference gas analyzer with feature extraction from mid-infrared laser absorption-modulated signal, *Measurement Science and Technology*, vol.32, 035201 (2021).

[7] J. Faist et al.: Quantum Cascade Laser, *Science*, vol.264, 553 (1994).

[8] D. Herriott et al.: Off-Axis Paths in Spherical Mirror Interferometers, *Applied Optics*, vol.3, 523 (1964).

[9] HORIBA, Ltd.: Japanese Patent Publication, No. 7094467 (2022).

[10] HORIBA, Ltd.: Japanese Patent Publication, No. 6886507 (2021).

[11] K. Hara et al.: Formaldehydes Measurement Using Laser Spectroscopic Gas Analyzer, *SAE Technical Paper*, 2021-01-0604 (2021).

[12] R. Suarez-Bertoa et al.: Real-Time Measurements of Formaldehyde Emissions from Modern Vehicles, *Energies*, vol.15, 7680 (2022).

[13] Y. Onishi et al.: Development of On-Board NH_3 and N_2O Analyzer Utilizing Mid-Infrared Laser Absorption Spectroscopy, *SAE Technical Paper*, 2021-01-0610 (2021).

[14] R. Suarez-Bertoa et al.: NH_3 and N_2O Real World Emissions Measurement from a CNG Heavy Duty Vehicle Using On-Board Measurement Systems, *Applied Sciences*, vol.11, 10055 (2021).

[15] T. Selleri et al.: Measuring Emissions from a Demonstrator Heavy-Duty Diesel Vehicle under Real-World Conditions—Moving Forward to Euro VII, *Catalysts*, vol.12, 184 (2022).

[16] Kyoji Shibuya: Development of High-precision, Real-time Gas Analysis Technology by Infrared Laser Absorption Modulation Method and its Industrial Application, *Bunseki-Kagaku*, Vol.72, in press (2023).

SHIBUYA Kyoji

Advanced R&D Department,
Technology Innovation Center, R&D Division
HORIBA, Ltd.
Ph.D.

Thermal Runaway: Can Ultrasound Finally Solve Li-ion Cells' Most Dangerous Challenge?

Michele BRAGLIA
Richard STOCKER

The occurrence of several battery-related accidents over the years has risen public awareness of risks and safety issues around electric vehicles (EVs). Current safety features implemented on battery management systems (BMSs) heavily depend on thermocouples instrumented to the surface of the cell. However, for an effective early warning system, the ability to record or detect internal changes of a cell is vital. One technique that may be ideally suited to this is ultrasonic measurement. As part of a European Automobile Manufacturers' Association (ACEA)-funded project, HORIBA MIRA has been collaborating with University College of London (UCL) to explore the use of ultrasound to detect internal changes in a cell to pre-emptively warn about thermal runaway (TR). This article reports on experimental studies aimed at evaluating the application of ultrasonic sensors to detect abuse conditions and early TR signals in battery cells. The changes in acoustic behaviours of battery cells have been monitored and evaluated during temperature-controlled, nail penetration, and overcharge as well as homogeneous and localised heating tests. Finally, ultrasound's ability to capture key events during thermal runaway propagation scenarios has been assessed by triggering TR in a cell of a small prototype module.

Introduction

In lithium-ion batteries (LIBs), accidents stem from two broad issues. In the first type, a cell or a battery pack can fail due to mechanical, thermal, or electrical abuse. During mechanical abuse, the two electrodes connect due to nail penetration, fracture of the separator, or deformation of the electrode. When the battery is subject to electrical abuse, such as over-discharge, metallic dendrites (mainly lithium or copper) grow on the anode surface and may penetrate the separator. Thermal abuse occurs when the cells are cycled/stored at excessive temperature, triggering the thermal decomposition of the materials inside the cells.

The second type of safety accident is generally the most feared since it occurs during the seemingly normal operations of the battery. These faults give no clear warning signals and are the most difficult to predict and detect. Such accidents are often due to the presence of internal short circuits (ISCs) caused by foreign metal particles that contaminate the electrode materials during the manufacturing process. These contaminants, in electrochemical contact with the cathode, are oxidized and dissolved into the electrolyte during cycling. They then diffuse and plate on the anode, piercing the separator and causing an ISC (grown-in internal shorts). When a large area ISC is formed, the electric energy is released at a high rate in

that area, rapidly increasing the internal temperature and, possibly, triggering TR. ISC has been the main cause of recalls of automotive LIBs.[1] This class of safety accidents is particularly eared as safety components incorporated in today's lithium-ion cells and battery packs are not effective.

What is Thermal Runaway and Why it is Challenging to Avoid

Both classes of safety accidents can trigger TR. During thermal runaway (Figure 1) the cell temperature increases due to exothermic reactions. In turn, the increased temperature accelerates the decomposition reactions and the system quickly destabilizes. At the end of the TR, temperatures higher than 1000 °C can be reached and high amounts of flammable and harmful gases are released.[2]

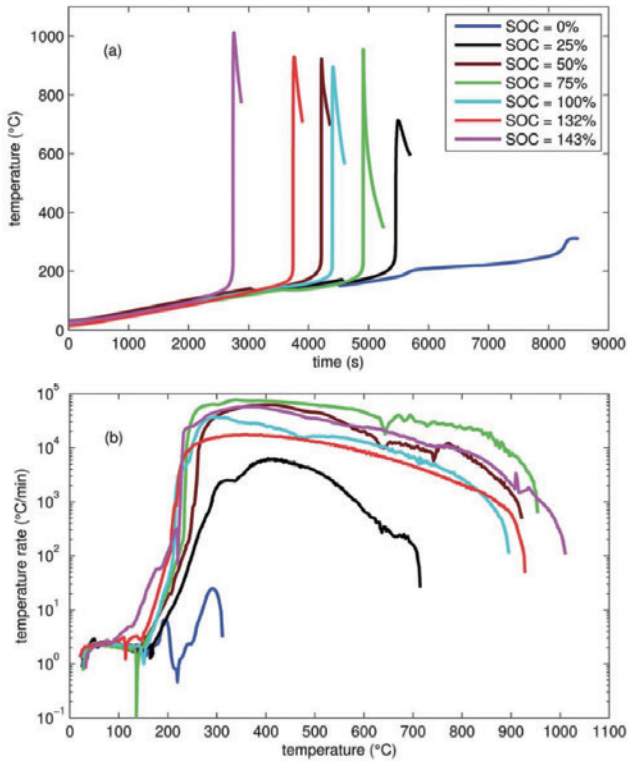

Figure 1 TR induced by thermal ramp experiments on NCA cathode cells at different states of charge.
(a) Cell temperature profiles, (b) Cell temperature rate vs. cell temperature. Adapted from.[2]

If a cell fails in a battery pack it can lead the surrounding cells to also fail, causing a chain reaction within the pack with potentially serious consequences which is known as thermal runaway propagation (TRP). Such an event is particularly scary in the automotive industry where high-capacity cells present in battery pack modules are often spaced less than 1 mm and, in some cases, there might even be direct contact among adjacent cells. In modules with banks of cells in parallel, if one cell experiences an ISC it can act as a short for the entire bank, leading to an external short for the remaining cells.

The BMS is a key safety component of the battery pack as, if properly designed, it can keep the battery pack from operating in unsafe conditions. However, some relevant issues arise when considering its implementation on EV battery packs. Standard BMSs rely on temperature readings from thermocouples located on the surface of the cell which, in the case of large cells, can be very different from the temperature of their centre. The formation of an internal cell temperature gradient can create local gassing and accelerated cell degradation. The cooling system, regardless of its efficiency, has limited efficacy on temperature gradients as it can only cool the cell surface. If not properly considered by the BMS, ageing can also cause cell unbalance which can limit cell capacity, accelerate degradation, or cause electrical abuse of some of the cells. The number of safety-related accidents that have occurred recently indicates that in some cases current BMSs alone can be inadequate.[3][4] For an effective early warning system, the ability to detect internal temperature changes is vital.

Legislation

On the 12th of May 2020, China issued three mandatory standards for EVs safety that relate to the EV battery, the EV itself and electric buses. The battery regulations mandate improved battery system safety regarding thermal diffusion, external fire, mechanical shock, simulated collision, thermal and humidity cycling, external short circuit, overcharge, and over-temperature. In addition, in the case of TR of one cell, no fire or explosion should occur in the cabin for at least 5 minutes, allowing for occupants to escape the vehicle. The battery system is required to notify the vehicle occupants of a thermal incident immediately. More stringent requirements for preventing water ingress, ensuring proper insulation and battery monitoring are also included. Due to their larger battery packs, the new standards for electric buses have more rigorous demands on battery casing collision, charging and water ingress. The standards request for appraisal of the flame-retardant performance, TR prevention and the battery management unit.[5]

To date, there exists a wide variety of battery designs and thermal management strategies across the various EVs. Manufacturers have varied between cylindrical, pouch and prismatic cells with air, water-glycol, or refrigerant-based cooling. As regulations like these are enforced it may well push the industry towards one solution. Emerging technologies like immersion cooling, where the cells are immersed in a flame-retardant dielectric fluid,

may start to take a larger share of the market. Detecting thermal events in vehicles is also a widely unexplored area of the market. Another consideration is how to notify passengers and if an active method of extinguishing the battery pack should be incorporated into the design. Crucially, all the methods have their limitations and it is imperative to avoid false positives and potentially extinguish a battery that is working correctly, as this is often the most expensive component in the vehicle.[5]

Factors of Risk

In current LIBs the cathode chemistry plays a major role with regard to proneness to TR. Transition metal oxides commonly employed as a cathode in LIBs become structurally unstable if their thermal decomposition temperature (TR onset temperature) is reached. The consequent release of the oxygen present in their crystalline structure prompts the combustion of the liquid electrolyte sustaining a rising heating rate that leads the cell to irreversibly enter TR. Among the commercially employed cathode materials, lithium iron phosphate (LFP) presents highest thermal stability. Nickel manganese cobalt oxide 111 (NMC111), has slightly better thermal stability than nickel cobalt aluminium oxide (NCA), which, combined with its good energy density, makes it one of the most widespread cathode materials in current LIBs. The thermal decomposition with associated oxygen release occurs at around 350 °C for LFP, 280 °C for NCA and 300 °C for NMC 111. The thermal stability of the high Ni-content cathodes as NMC 811 drastically decreases, with thermal decomposition starting already at 150 °C in the case of the NMC 811.[6]

The thermal stability of carbonaceous and transition metal oxides is a function of the state of charge (SoC). This becomes particularly evident in the case of overcharge where TR onset temperatures decrease sharply as SoC increases. The onset temperatures of thermal decomposition in overcharged NCA cells can go as low as 65 °C.[6]

Cell design is also crucial for safety. Nanomaterial- level design strategies can allow the usage of thermally unstable materials (Ni-core rich, Mn-shell rich active materials). A crucial design parameter for safety is the capacity load ratio. The anode should be present in slight excess with respect to the cathode to avoid lithium plating due to loss of anode active material during ageing. Kinetics mismatch between anode and cathode must also be avoided and the porosity of the electrodes must be properly implemented.

The geometry of the cell also has some important consequences on safety. Pouch cells are sometimes considered safer since they can freely expand and release pressure. However, safety vents are installed on rigid prismatic and cylindrical cells. The design and size of the vent are critical to ensure suitable pressure management. An important parameter is also the cell size. Larger cells contain more chemical energy, exhibit higher temperature gradients and their cooling is less effective due to the lower surface-to-volume ratio.

Experimental TRP studies have shown that cell spacing, tab connection, vents location/design and thermal barriers are the key parameters to mitigate TRP risks. However, the empirical nature of such tests makes their validity limited to the specific assembly and configuration tested. Small differences in cell designs, cell manufacturing methods and ageing states can severely affect the results of such tests.

Methods to Monitor Battery Packs

Optimal combinations of cell materials, design and advanced BMS strategies can reduce but not eradicate the risk of TR. Thus, it is crucial to develop methods that can promptly detect nascent TR to give the BMS more time to take suitable countermeasures or to passengers to leave the vehicle. Some TR detection methods are presented and schematically illustrated in Table 1:

- Gas/pressure/strain gauge sensors: gas generation starts occurring in the very early stages of TR, regardless of the cell type, chemistry, and format. During overheating, the liquid electrolyte expands, the internal pressure increases, and the gas is vented out of the cell. Gas and pressure sensors were proven to be capable to detect TR onset more quickly than non-embedded temperature sensors and in a stage in which TR can still be impeded if suitable countermeasures are adopted.[9] Each sensor type has its characteristic detection speed, signal clarity and actual deployment feasibility. A combination of different sensors could be instrumented to a cell to correlate each measured signal with the TR onset and the best sensors setup to detect TR identified.
- Other techniques based on self-discharge current detection, cell modelling (equivalent circuits, Kalman filters), consistency analysis of parameters within the battery pack and electrochemical impedance spectroscopy have been successfully implemented and applied to detect ISC or thermal abuse and have good potential to be implemented onboard.[10]-[20]

Table 1 Matrix summarising the TR detection methods listed in this document and their relative pros and cons.

·Detection methods	Advantages	Disadvantages
·Self-discharge measurement	- Simple, quick, and effective in detecting ISC	- Conventional methods to measure self-discharge are time-intensive (typically taking days or even weeks), costly, complex and/or not well-difined - TR triggered by thermal, mechanical, and electrical abuse is not directly detected
·Consistency within the battery pack	- Cheap and easy to implement onboard	- Relies on external temperature readings - Threshold for deviations from normal conditions might cause unacceptably frequent stops and too loose conditions might be ineffective in timely detecting TR
·Multi-sensors	- A suitable combination of different types of sensors can provide an early warning of TR	- Temperature and voltage sensors are not effective to detect TR under certain conditions. Their combination with other sensors increases system cost and complexity - More prone to sensor failure - The interpretation of the sensore's readings might not be so straightforward and false alarms can be generated since gas and pressure increases can occur also during normal battery operation
·Internal short circuit modelling	- Does not require additional sensors onboard (only I, V and T sensors needed)	- Complexity, computational resources - Can be hard to verify/adapt to different cell types
·Impedance spectroscopy	- Can infer the internal temperature of a cell - In the case of certain I, V input signals (i.e. square waves) it can be applied onboard	- Its adaptation and interpretation for different cell chemistries might be cumbersome since the SoC and the ageing of the battery can be difficult to separate from the temperature effect

A Novel Approach: Acoustic Impedance

Ultrasonic testing is a non-destructive technique based on monitoring how ultrasound waves propagate through an object of interest. In industry, ultrasound is typically used to test for cracks within materials, measure thicknesses and monitor corrosion of pipes. Another common use is in underwater range finding (Sonar) in which by measuring the difference in time between the pulse being transmitted and the echo being received, it is possible to determine the distance of an object. In medical imaging, ultrasound is used to visualize muscles, tendons, and many internal organs to capture their size, structure and any pathological lesion with real-time tomographic images. The technology is relatively inexpensive and portable, especially when compared with other techniques, such as magnetic resonance imaging and computed tomography. Recently, ultrasound is gaining attention for the study of electrochemical devices.[21]-[23] The main advantages of this technique are that it is non- destructive, can be conducted operando, it is relatively cheap, and measurements are very quick, taking only microseconds to complete.

Working Principle and Potential for Monitoring Batteries Safety

In the battery test bench used for acoustic analysis, a cell equipped with an ultrasonic transducer and a thermocouple is placed inside a thermal chamber and connected to an external battery cycler and an ultrasonic multiplexer which generates and record the electrical and acoustic signals. When conducting an ultrasonic measurement, a very short ultrasonic pulse wave is generated by a piezoelectric transducer. The signal then travels through the object of interest and the wavefront is a influenced by the properties of the object's component materials. The signal is then either received by a second transducer on the other side of the object (Transmission) or the reflected waves are received by the same transducer that generated them (Pulse Echo). An important acoustic wave property is the time of flight (ToF) which is the time taken for the generated wave to travel through the object and is affected by the speed of sound through the material through which it propagates.

Typical waveforms obtained for pulse-echo mode and transmission set-ups performed on the same cell are shown in Figure 2.[30] In pulse-echo mode Figure 2a, the initial signal at a ToF below 1 µs is due to the generation of the initial ultrasonic pulse and is not influenced by the cell under study. The peaks at ToF values higher than 1 µs are reflection peaks related to the internal structure and the interfaces present within the cell. Acoustic peaks corresponding to higher ToFs reflect the properties of interfaces located farther from the acoustic emitting device. The amplitude of these internal reflection peaks decreases steadily with penetration depth due to signal attenuation and reflection in previous layers. At ca 8.7 µs a peak with a slightly higher amplitude is observed. This is referred to as the first echo peak and corresponds to the part of the ultrasonic signal that has travelled all the way through the cell and hit the back case. Due to the large difference in acoustic impedance between the cell and the external air, nearly all the signal is reflected resulting in the slightly higher amplitude observed. In the transmission set-up (Figure 2b) a strong peak is observed at a ToF approximately half of that observed for the pulse-echo experiments. The strong multiple peaks observed at lower ToFs in pulse-echo mode are no longer observed as these are due to reflections from the internal layers within the cell.

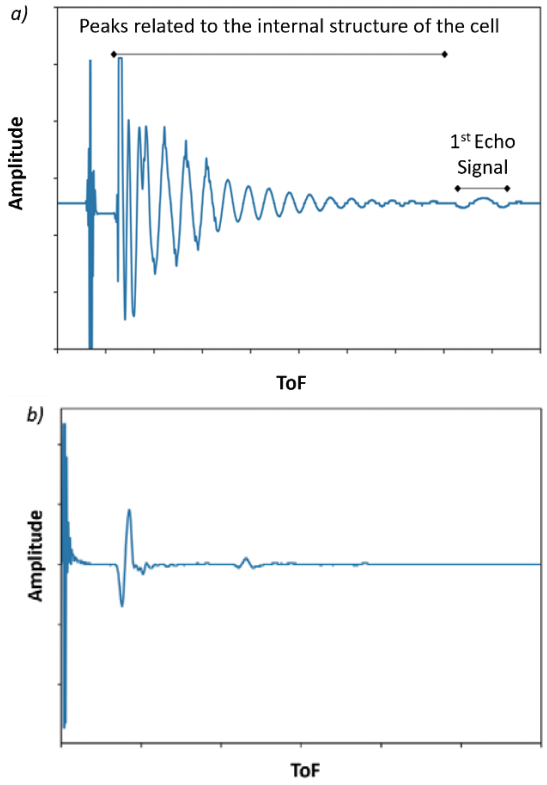

Figure 2 Typical acoustic waveform generated from a) pulse- echo mode and b) transmission mode setups. Adapted from.[30]

LIBs present a typical layered structure in which the anode is constructed of a carbon material supported on a copper current collector, the cathode consists of an active material, typically a metal oxide such as NCA or NMC supported on an aluminium current collector, and a separator which ensures that no direct contact is made between the anode and the cathode. Such layers are then wrapped together to form the so-called jelly roll. All components in the pouch cell are soaked in an electrolyte solution which acts as an acoustic couplant between different layers and allows the acoustic signal to travel through the cell. When an ultrasound waveform is generated by the transducer placed on the surface of the cell, the wavefront travels through the cell. At every material interface, some of the signal is transmitted and some is reflected back towards the transducer. The percentage reflected and transmitted is dependent on the difference between the acoustic impedance of the two materials. As the material properties change with cycling, the speed of sound through the materials will also be affected resulting in a shift in peak's ToFs. In addition, the electrode layers expand and contract as lithium ions move, also resulting in shifts in peak's ToFs.

The capability of acoustic waves to unveil information about internal interfaces and material properties of batteries has recently led to initial studies in which ultrasound and acoustic sensors have been employed to estimate SoC and state of health (SoH),[22]-[27] but only few have reported the use of acoustic measurements to monitor abuse testing of LIBs.[28] For the interested reader, the experimental studies here reported have been published in specialised scientific journals.[29][30]

Experimental Work Between HORIBA MIRA and UCL

This study aimed to assess the practical capability of acoustic-based techniques to promptly inform about abusive operating conditions occurring within battery cells. It explored the method's potential to be effectively employed in real-world applications as an early TR detection method, benchmarking it against currently employed sensors such as thermocouples and voltage sensors. A broad range of techniques for inducing TR (including nail penetration, overcharge as well as uniform and localised heating) was tested on several 210 mAh pouch cells based on a lithium cobalt oxide cathode (LCO) and a graphite anode. The acoustic measurements were compared with voltage and temperature readings and X-ray radiography was employed to give further physical insight and support findings from acoustic measurements. The TRP through a small module of cells was investigated with the use of multiple transducers.

Results

Internal Temperature

To determine how the temperature of the cell affects the waveform generated by ultrasonic analysis, a 210 mAh pouch cell was set up in an environmental chamber and the acoustic signal was monitored as the temperature was varied.[30] Figure 3a shows a plot of how the temperature was altered with time . To investigate the cell behaviour in mildly abusive conditions, the temperature was varied beyond the window temperature assigned by cell manufacturers (0-40 °C). A colourmap plot of how the acoustic signal changes during this period is shown in Figure 4b. This plot is effectively a top-down view of how the typical signal varies with temperature. Each line shows a peak, with the colour indicating the amplitude and its position in the y-direction indicating the ToF.

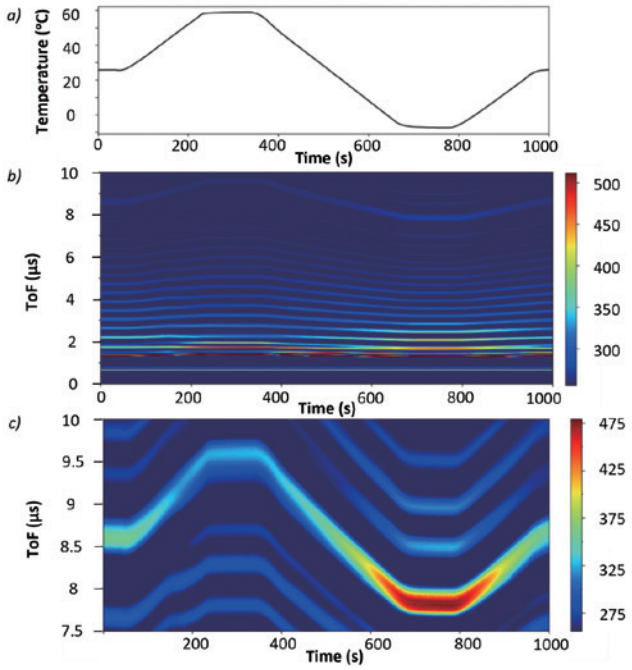

Figure 3 (a) A plot of how cell temperature varied over the course of the experiment. (b) A colourmap plot showing how the received acoustic waveform varied over the course of the temperature experiment. (c) A colourmap plot of how the first echo peak varies as the temperature is varied over the duration of the experiment. Adapted from.[30]

As the temperature is initially held constant, no variation in amplitude or ToF is observed with any peak. During heating the ToF of each peak increased due to the individual anode and cathode layers expansion, causing the entire cell to swell accordingly. The effect becomes more pronounced as the ToF of the peak increases since for reflections from deeper interfaces the signal must travel farther through the changing battery materials and the effects are increased. As the cell is cooled the changes are reversed due to the contracting of the cell, while the amplitude of all peaks increases. The first echo peak, located at 8.75 µs, shows the largest shift in ToF with temperature.

For the temperature to be accurately predicted using the acoustic techniques, an understanding of how the SoC of the cell affects the relationship is required. To investigate this, the previous experiment was repeated at various SoCs and the results are summarised in Figure 4.[30] For all SoCs, a linear relationship between the first echo peak's ToF and the temperature is observed, with a similar gradient between 0 and 50 °C, which allows to easily measure the internal temperature of a given cell. At higher and lower temperatures, the correlation deviates from linearity suggesting cell ageing/damage. This damage is likely due to taking the cell outside of the manufacturer's temperature specifications. Small deviations from the predicted linear relationship between ToF and temperature could then be used to detect and measure the extent of cell damage. This may represent a powerful tool for predicting the onset of irreversible cell degradation and TR.

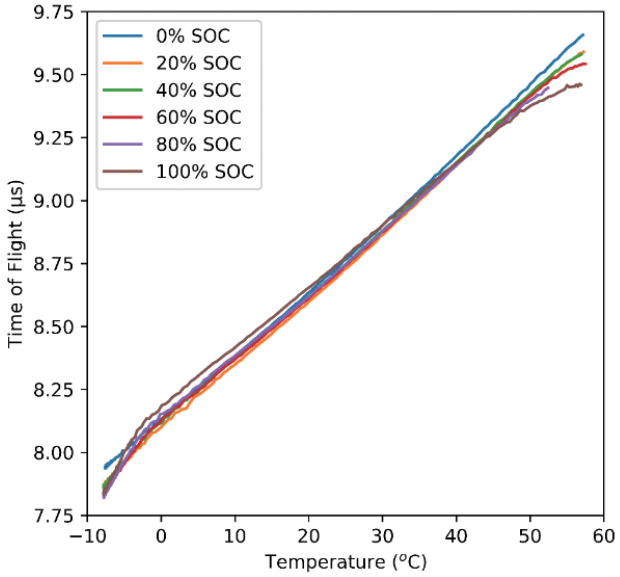

Figure 4 The variation of ToF of the first echo peak at various SOCs. Adapted from.[30]

For the applicability of ultrasound in automotive, the technique must apply to a wide range of cell geometries and capacities. As a proof of concept to show the flexibility of the technique, a range of cell geometries and capacities from a range of manufacturers were also tested. Tests on a 400 mAh cell with same cell chemistry and construction techniques from the same manufacturer and on a 20 Ah A123 pouch cell using both through-transmission and pulse-echo experiments gave consistent results with higher ToFs than the 210 mAh cell as would be expected.

The effect of the cell geometry was also explored via cylindrical cell testing in pulse-echo and transmission mode. Pulse-echo measurements did not prove successful with no repeatable readings obtained whereas tests in transmission mode did prove successful. Transducers were set up at 180º configuration. It was also found that if the transmit and receive transducers are not aligned (180º set-up) and instead are placed with a slight angle between them, the obtained results vary. The propagation of lamb waves around the outer can of the cylindrical cell results in two additional wavelets that appear in the waveform. Depending on the angle of the receiver transducer relative to the transmission transducer the ToF of these lamb waves is altered. This feature shows the potential to detect can swelling as well as surface defect formation by monitoring how the two lamb waves behave.[29]

Detection of Internal Defects

To determine the ability of acoustics to detect any defects that may be present in cells or formed during operation/abuse, acoustic tests were run on two 400 mAh pouch. One of the cells was unused whereas the other had been cycled multiple times during which a sudden failure had occurred. Typical waveforms obtained from transmission experiments for both the 'good' and 'defective' cell are shown in Figure 5.[29]

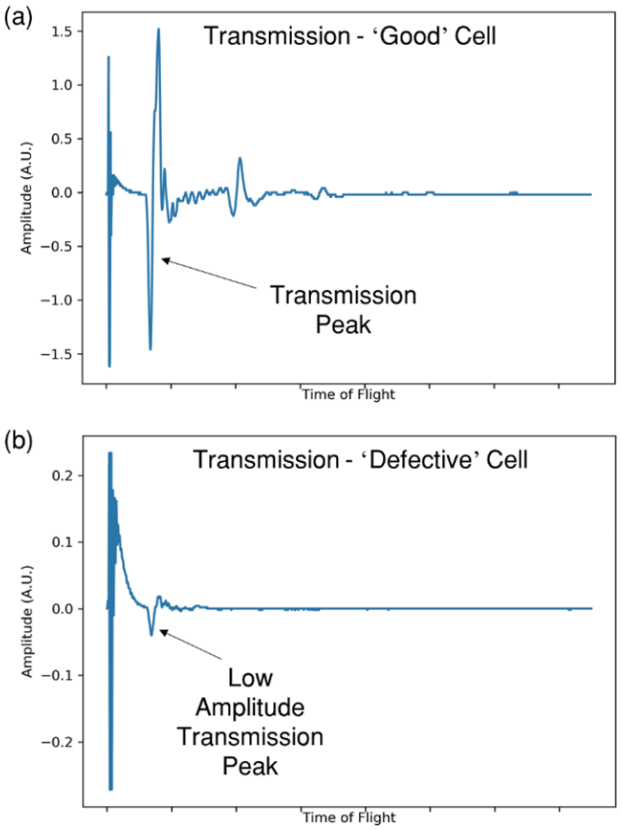

Figure 5 The difference in transmission results for a 'good' 400 mAh cell (a) and a 'defective' cell (b). Adapted from.[29]

The 'good' cell shows a high amplitude transmission peak (Figure 5a) whereas the 'defective' cell also shows the transmission peak at the same ToF but the amplitude has dropped significantly. These results suggest the presence of a defect since the formation of any gases or defect would inhibit good acoustic contact between the electrode layers. To investigate this, the defective cell was studied using X-ray computed tomography.[29] Figure 6 shows visible layer separation at 160 µm. These tests show that even small defects can lead to significant changes in the acoustic signal.

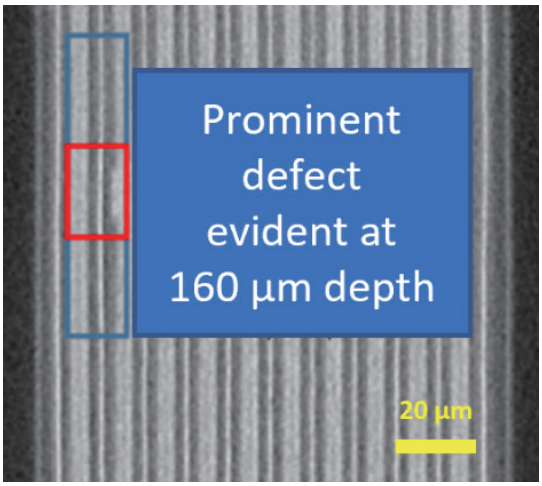

Figure 6 X-ray computed tomography results showing the internal structure of the 'defective' 400 mAh cell shows the prominent defect.. Adapted from.[29]

Thermal Runaway Studies at Cell Level

To acoustically monitor TR in individual cells and its propagation through a module or pack consisting of multiple cells, a method for triggering TR which is reliable, repeatable, and representative of EVs in real- world applications is required. Several methods were tested with a focus on those that would most closely replicate a TR event triggered by an ISC.

The first method tested was nail penetration. Nail penetration is generally regarded as the industry standard test for replication of ISCs. For internal shorts, the highest rates of reaction and largest temperature increases are expected to occur around the nail. Thus, the surface temperature of the cell is not representative of the higher temperatures within the cell. To assess the ability of ultrasound to measure the extent of damage that occurs during TR, several tests were conducted with the chosen cell, a 210 mAh LCO pouch cell, at various SoCs under the assumption that a higher SoC would release more energy during failure and cause more damage. The results showed a sudden loss of acoustic signal in all tests regardless of the SoC of the cell or the amount of damage induced, proving its high sensitivity to the structural damage caused by a nail penetration in the cell.

Another method for inducing TR is by overcharge. Overcharge of LIBs in constant current mode can lead to rapid temperature increase and eventually induce TR. For these tests, C-rates significantly above those recommended by the manufacturer's specification were chosen. A fully charged cell (4.2 V) was overcharged at 10 C followed by 20 C while acoustic measurements were conducted. A strong influence on the acoustic signal was observed. However, the complex nature of the processes occurring within the cell made this technique unsuitable as a method of triggering TR. The overcharge tests did

however suggest that the acoustic methodology could be useful for understanding the process occurring within the cell during overcharge.

Thermally-induced TR, i.e. TR triggered by heating the cell until it fails, is one of the simplest methods for inducing cell failure. To study the ability of acoustic sensors to monitor thermally-induced TR, a cell with a transducer attached was heated between two heating plates. While repeatable and consistent acoustic signals were observed for cells operating under normal conditions, when the cells were pushed outside these limits toward dangerous temperatures, clear changes in acoustic signals were visible. At lower temperatures, additional peaks were observed indicating the presence of additional interfaces within the cell as thermal damage occurs. When the temperature increased further, the ToF of the first echo peak shifted quite drastically before disappearing completely at ca. 100 °C, when the electrolyte likely evaporated. Importantly all these distinct and measurable changes occurred long before the cell entered irreversible TR.

Thermally-induced TR was proved to be a useful method for inducing TR. However, homogeneous heating of the cell is less representative of the type of thermal abuse that would likely occur in a real-world application caused by an ISC, where higher thermal gradients would be more localised within the cell. To make the tests more representative, a heating cartridge was used to heat a small area of the cell to represent the area where a short is occurring. A fully charged cell was heated from the bottom of the cell with a heating cartridge, while an acoustic transducer was placed on the top of the cell. The results of the experiment showed that the voltage remained relatively consistent until the cell entered TR, proving that monitoring cell voltage does not reveal damaging processes occurring within the cell. Over the first 150 seconds, while there was little to no change observed in the temperature recorded by the thermocouple placed on the top of the cell by the transducer, significant changes in the acoustic signal were observed. The echo peak (close to the heating cartridge) was the first peak to disappear, followed sequentially by peaks at lower ToFs, about 500 seconds before the cell entered TR. Importantly, readings from the thermocouples only showed a mild temperature rise throughout.

Thermal Runaway Propagation at Module Level

For higher power operations battery modules or packs are often used, in which multiple cells are connected in series to provide higher voltages and in parallel to provide higher currents (Figure 7).

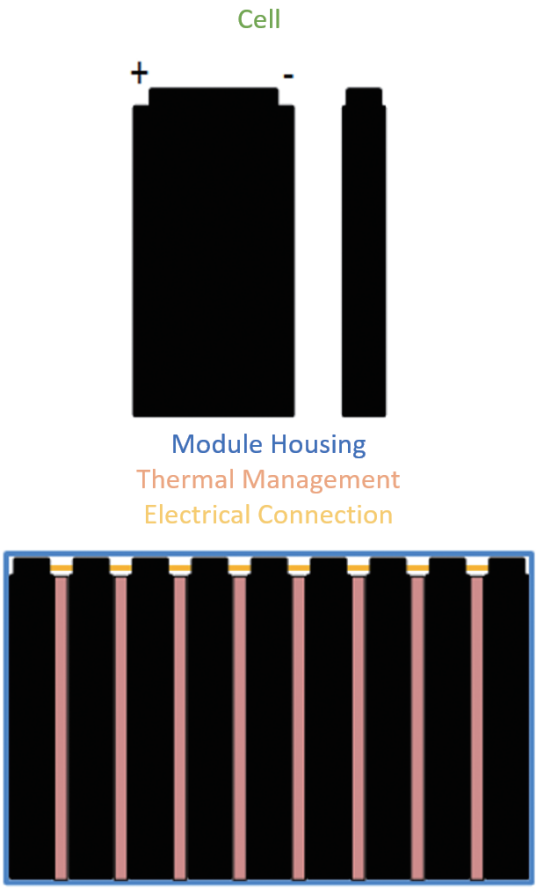

Figure 7 Single-cell and multiple cells assembled in the module configuration.

Understanding the operation of these packs and the inherent risks is of vital importance. Failure of a single cell can easily trigger the rapid heating and consequential failure of neighbouring cells causing a thermal propagation chain reaction.

To study the effectiveness of the ultrasonic technique in pack applications, a small four-cell demonstration module was constructed. Each of the four cells was placed side by side and connected in parallel with a transducer placed on the surface of each of the cells. Thermocouples were placed on the top and bottom of each cell to monitor the temperature of each cell and the thermal gradient from the top of the cell to the bottom.

To determine the expected variation in acoustic signal during normal operation the pack was first left at rest or 15 min before being discharged at 1 C, then immediately charged again at 1 C. All cells exhibited similar acoustic signatures, with changes in the acoustic signals which were measurable but not significant compared to the changes observed in the TR tests.

The four-cell module was then subjected to an abuse test (Figure 8). A heating cartridge was placed on the underside of Cell 4 to trigger localised damage followed by TR. Initially, all cells were held at room temperature for ca.

400 seconds. Then, the heating cartridge in contact with the base of Cell 4 was switched on. All cells were supported on a heat-proof mat with the heating cartridge only in contact with Cell 4. The results from this test are summarised in Figure 9, with the acoustic behaviour of the cells shown along with the temperature of the bottom of each cell.

During rest at room temperature, no shift in any of the acoustic signals is observed. As soon as the localised heating on Cell 4 is initiated, the acoustic signal of this cell begins to change. For clarity, the change in ToF of the first echo peak has been plotted for all cells in Figure 10 and compared to the temperature of the top and bottom of the cell. During heating, the ToF of the first echo peak of Cell 4 rapidly increases beyond any change that would be expected under normal operation.

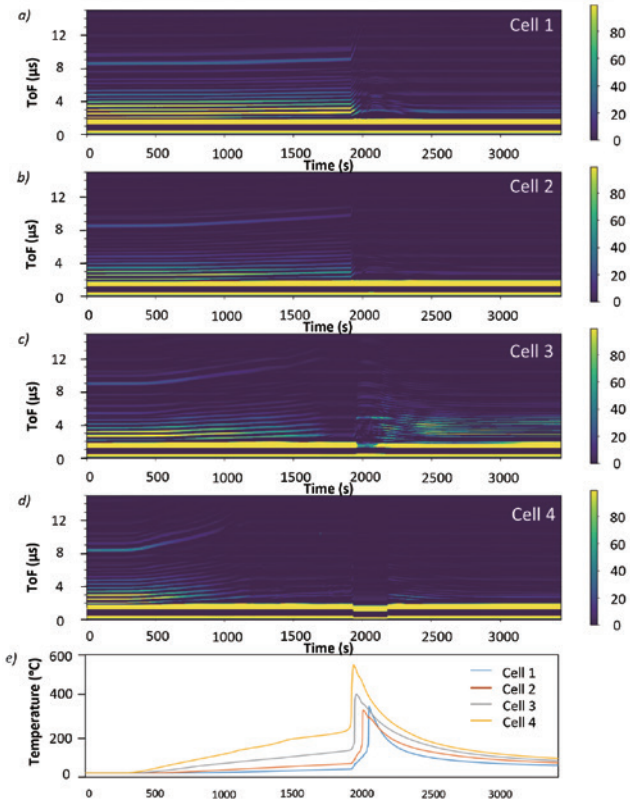

Figure 8 The propagation of thermal failure through a four-cell pack. The acoustic behaviour of Cell 1 (a), Cell 2 (b), Cell 3 (c) and the thermally abused Cell 4 (d) are shown as well as the temperature of the bottom of each cell (e).

After ca. 1000 seconds, the peak amplitude drops and the signal is lost. Meanwhile, the top of the cell is at 70 °C and the bottom at 117 °C, sufficient for electrolyte evaporation. At this point, the acoustic signal has indicated that a significant thermal event and/or damage has occurred to Cell 4. The cell, however, is heated for a further 900 seconds (15 minutes) before it enters TR. The ToF of the first echo peak in Cell 3 also begins to shift as soon as the heating of Cell 4 begins, albeit at a slower rate. After 1400 seconds, 400 seconds slower than Cell 4, the amplitude of the first echo peak in Cell 3 is also lost. The temperature at the bottom of the cell is ca. 100 °C at this point. As Cell 4 enters TR, the heat produced also causes Cell 3 to rapidly heat and enter TR. Cell 2 and Cell 1 also follow similar dynamics although at slower rates due to their farther location from the cell that first undergoes TR. However, the ToF of the first echo peak remains visible until the cells enter TR, suggesting they were still relatively undamaged until the flames coming from the other cells reached them.

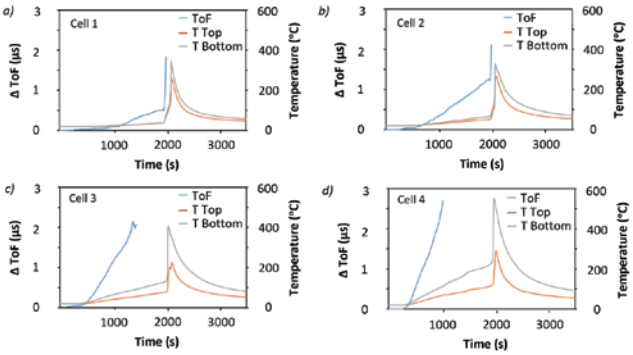

Figure 9 The temperature and ToF variation of the module cells (a) Cell 1, (b) Cell 2, (c) Cell3, (d) Cell 4.

Since the change in ToF of the first echo peak can be both measured using acoustics and predicted based on thermocouple measurements, a potential method to detect unexpected heating or damage is to look for any changes in ToF that are unexpected based on thermocouple readings. To explore this, the ToF of the first echo peak was tracked and the predicted ToF change calculated based on a thermocouple measurement. The predicted value was then subtracted from the measured one. When the cell was operated in normal conditions a value of zero was returned. Conversely, when any change in temperature that wasn't measured by the thermocouple occurred, the predicted and measured values differed, resulting in a deviation from zero. This deviation indicated that a temperature shift not recorded by the top thermocouple was occurring. This type of measurement seems promising to detect any internal temperature changes, such as those caused by ISCs.

Repeatability and Susceptibility to False Positives

For this technology to be implemented in a BMS, the measurements must be robust, repeatable, and not susceptible to false positives. While more work needs to be done before the acoustic temperature measurement technique can be employed commercially, initial results are promising. All tests reported in this study show consistent results with similar acoustic behaviours observed in all TR experiments. The acoustic waveform observed is consistent from cell to cell and the changes observed during

failure are significantly larger than any changes observed in normal use, as shown in Figure 10. The cell to cell variation under normal operation (cycling at the cell's max C rate) is significantly smaller than the changes observed for all cells in the module tested. The point at which each cell reached 60 °C, the cell's maximum working temperature, is also marked on the plot and demonstrates that, based on acoustic readings, an indication of an issue with each cell would have been recorded long before the cell entered an irreversible self-heating process or TR.

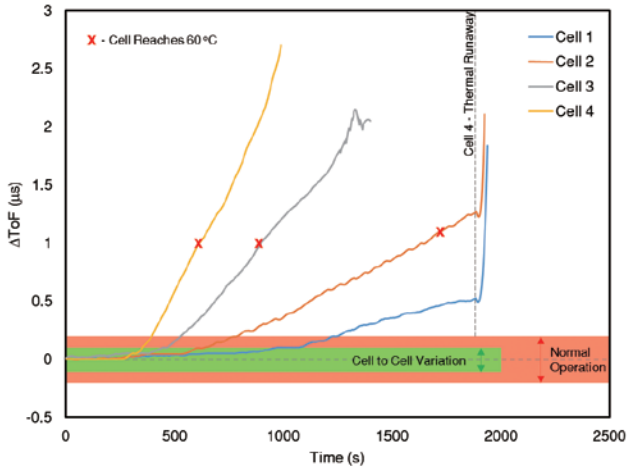

Figure 10 The changes in ToF for each peak relative to cell-to- cell variation and changes in ToF during regular operation.

Conclusions and Further Research

This study demonstrated the ability of ultrasound measurements to accurately monitor the internal temperature of a cell, detect rapid heating and indicate when a cell is about to enter TR well before conventional methods based on voltage and temperature readings. In the module setup, the acoustic signature of the first echo pulse is lost is ca. 900 seconds before the cell enters TR. It was shown that ultrasonic testing can be used to probe virtually all types of batteries. A range of techniques for inducing TR was tested. The significant structural damage caused by a nail penetration experiment instantly causes a loss in acoustic signal due to the gaps appearing between layers and stopping acoustic transmission. Thermally-induced heating of the cell proved to be the most effective and reproducible method for inducing cell failure. The changes in ToF of the first echo peak correlate with cell temperature and give a clear indication of when a cell is heating. In these tests the electrolyte evaporation resulted in a loss of acoustic signal, providing a clear indication that significant cell heating and damage were occurring. To replicate more representatively real-world applications, the thermally induced TR experiments were repeated by heating only a small area of the cell. These tests showed that the technique could detect internal temperature changes long before the thermocouples placed on the surface of the cell. With the use of multiple transducers, it was also possible to detect the propagation of TR through a small module of cells. Indications that the cells were reaching dangerous temperatures were evident from acoustic measurements long before the first cell failed triggering a chain reaction through the pack and causing all cells to fail. Finally, acoustic measurements were proven to be particularly reliable, delivering consistent acoustic signals across different cells and significantly larger ToF changes than any observed in normal use in the case of abuse conditions.

From the results here presented, a short-term application could be to include ultrasonic monitoring as part of HORIBA MIRA's abuse testing approach to provide real-time access to internal states of the cell as well as more informative data and consultancy on test outcomes. With regards to onboard battery pack applications, while these results are very encouraging, there is a long way to go before "smart" batteries (i.e. containing an ultrasonic diagnostic system) can be commercially manufactured. To take the technology forward on the journey to mass-production, more comprehensive ultrasonic tests on a wide variety of batteries (encompassing the complete spectrum of battery types), looking across the complete range of operational variables (temperature, age, charging history, battery construction, etc) shall be performed. All tests will need to be repeated multiple times to statistically have confidence that the ultrasonic data can reliably show the condition of the battery. A cost-effective integrated ultrasonic transducer system including transducers, electrical connectivity, transducer drive electronics and signal analysis will need to be developed for each class of cell/battery.

Finally, an analysis needs to be made as to what proportion of cells within the battery pack needs to be monitored. A battery-analysis system that relied on a few cells within the pack being ultrasonically active would significantly reduce costs and greatly simplify the system connectivity. With this regard, a promising technique currently under investigation at UCL for monitoring electrochemical devices is acoustic emission. While the techniques discussed thus far rely on the generation of an ultrasonic pulse to probe the device and another, or the same transducer, to receive the altered acoustic signal, emission uses a single transducer to 'listen' for any sounds generated by the cell itself. In the typical setup used for an acoustic emission experiment, an acoustic emission sensor, effectively a transducer similar to those used for ultrasound testing, is placed on the cell of interest and sounds generated by the cell are monitored. This approach presents several advantages for battery pack

monitoring where it has the potential to sensibly reduce costs and system complexity.

Acknowledgments

The authors would like to acknowledge the European Automobile Manufacturers' Association (ACEA) for support in funding the experimental work here presented.

* Editorial note: This content is based on HORIBA's investigation at the year of issue unless otherwise stated.

References

[1] Q. Wang, B. Mao, S. I. Stoliarov, and J. Sun, "A review of lithium ion battery failure mechanisms and fire prevention strategies," Prog. Energy Combust. Sci., vol. 73, pp. 95-131, Jul. 2019.

[2] A. W. Golubkov et al., "Thermal runaway of commercial 18650 Li-ion batteries with LFP and NCA cathodes - Impact of state of charge and overcharge," RSC Adv., vol. 5, no. 70, pp. 57171-57186, 2015.

[3] Faiz Siddiqui, "A Tesla Model S erupted 'like a flamethrower.' It renewed old safety concerns about the trailblazing sedans," The Washington Post, 2020.

[4] Heekyong Yang, "Kona EV owners say Hyundai mishandling recall for battery fires," Reuters, 2020.

[5] James Edmondson, "China to Enforce Electric Vehicle Safety by 2021," 2020. [Online]. Available: https://www.idtechex.com/en/research- article/china-to-enforce-electric-vehicle-safety-by-2021/20707.

[6] M. Braglia, "Thermal Runaway and Thermal Propagation Detection," 2019.

[7] C. Mikolajczak, K. White, M. Kahn, and R. T. Long, Lithium-Ion Batteries Hazard and Use Assessment. SpringerBriefs in Fire, 2013.

[8] J. Garche and K. Brandt, Eds., Electrochemical Power Sources: Fundamentals, Systems, and Applications Li-Battery Safety. Elsevier, 2019.

[9] S. Koch, K. Birke, and R. Kuhn, "Fast Thermal Runaway Detection for Lithium-Ion Cells in Large Scale Traction Batteries," Batteries, vol. 4, no. 2, p. 16, 2018.

[10] X. Feng, C. Weng, M. Ouyang, and J. Sun, "Online internal short circuit detection for a large format lithium ion battery," Appl. Energy, vol. 161, pp. 168-180, 2016.

[11] C. Wu, C. Zhu, Y. Ge, and Y. Zhao, "A diagnosis approach for typical faults of lithium-ion battery based on extended Kalman filter," Int. J. Electrochem. Sci., vol. 11, no. 6, pp. 5289-5301, 2016.

[12] N. S. Spinner, C. T. Love, and S. G. Rose-Pehrsson, Susan L. Tuttle, "Expanding the Operational Limits of the Single-Point Impedance Diagnostic for Internal Temperature Monitoring of Lithium-ion Batteries," Electrochim. Acta, vol. 174, pp. 488-493, 2015.

[13] Z. Liao, S. Zhang, K. Li, G. Zhang, and T. G. Habetler, "A survey of methods for monitoring and detecting thermal runaway of lithium-ion batteries," J. Power Sources, vol. 436, no. June 2019, p. 226879, 2019.

[14] L. H. J. Raijmakers, D. L. Danilov, J. P. M. Van Lammeren, M. J. G. Lammers, and P. H. L. Notten, "Sensorless battery temperature measurements based on electrochemical impedance spectroscopy," J. Power Sources, vol. 247, pp. 539-544, 2014.

[15] L. H. J. Raijmakers, D. L. Danilov, J. P. M. Van Lammeren, T. J. G. Lammers, H. J. Bergveld, and P. H. L. Notten, "Non-Zero Intercept Frequency: An Accurate Method to Determine the Integral Temperature of Li-Ion Batteries," IEEE Trans. Ind. Electron., vol. 63, no. 5, pp. 3168- 3178, 2016.

[16] R. Srinivasan, P. A. Demirev, and B. G. Carkhuff, "Rapid monitoring of impedance phase shifts in lithium-ion batteries for hazard prevention," J. Power Sources, vol. 405, no. September, pp. 30-36, 2018.

[17] R. Srinivasan, B. G. Carkhuff, M. H. Butler, and A. C. Baisden, "Instantaneous measurement of the internal temperature in lithium-ion rechargeable cells," Electrochim. Acta, vol. 56, no. 17, pp. 6198-6204, 2011.

[18] B. G. Carkhuff, P. A. Demirev, and R. Srinivasan, "Impedance-Based Battery Management System for Safety Monitoring of Lithium-Ion Batteries," IEEE Trans. Ind. Electron., vol. 65, no. 8, pp. 6497-6504, 2018.

[19] R. Schwarz, K. Semmler, M. Wenger, V. R. H. Lorentz, and M. Marz, "Sensorless battery cell temperature estimation circuit for enhanced safety in battery systems," IECON 2015 - 41st Annu. Conf. IEEE Ind.

Electron. Soc., pp. 1536-1541, 2015.

[20] J. P. Schmidt, S. Arnold, A. Loges, D. Werner, T. Wetzel, and E. Ivers-Tiffée, "Measurement of the internal cell temperature via impedance : Evaluation and application of a new method," J. Power Sources, vol. 243, pp. 110-117, 2013.

[21] Y. S. Chou, N. Y. Hsu, K. T. Jeng, K. H. Chen, and S. C. Yen, "A novel ultrasonic velocity sensing approach to monitoring state of charge of vanadium redox flow battery," Appl. Energy, vol. 182, pp. 253-259, 2016.

[22] B. Sood, C. Hendricks, M. Osterman, and M. Pecht, "Health monitoring of lithium-ion batteries," Electron. Device Fail. Anal., vol. 16, no. 2, pp. 4-16, 2014.

[23] A. G. Hsieh et al., "Electrochemical-acoustic time of flight: In operando correlation of physical dynamics with battery charge and health," Energy Environ. Sci., vol. 8, no. 5, pp. 1569-1577, 2015.

[24] S. Bhadra, A. G. Hsieh, M. J. Wang, B. J. Hertzberg, and D. A. Steingart, "Anode Characterization in Zinc-Manganese Dioxide AA Alkaline Batteries Using Electrochemical-Acoustic Time-of-Flight Analysis," J. Electrochem. Soc., vol. 163, no. 6, pp. A1050-A1056, 2016.

[25] G. Davies et al., "State of Charge and State of Health Estimation Using Electrochemical Acoustic Time of Flight Analysis," J. Electrochem. Soc., vol. 164, no. 12, pp. A2746-A2755, Sep. 2017.

[26] L. Gold et al., "Probing lithium-ion batteries' state-of-charge using ultrasonic transmission - Concept and laboratory testing," J. Power Sources, vol. 343, pp. 536-544, 2017.

[27] P. Ladpli, F. Kopsaftopoulos, R. Nardari, and F.-K. Chang, "Battery charge and health state monitoring via ultrasonic guided-wave-based methods using built-in piezoelectric transducers," Smart Mater. Nondestruct. Eval. Energy Syst. 2017, vol. 10171, no. March, p. 1017108, 2017.

[28] Y. Wu, Y. Wang, W. K. C. Yung, and M. Pecht, "Ultrasonic Health Monitoring of Lithium-Ion Batteries," Electronics, vol. 8, no. 7, p. 751, 2019.

[29] J. B. Robinson et al., "Identifying Defects in Li-Ion Cells Using Ultrasound Acoustic Measurements," J. Electrochem. Soc., vol. 167, no. 9626352, 2020.

[30] R. E. Owen et al., "Operando Ultrasonic Monitoring of Lithium-Ion Battery Temperature and Behaviour at Different Cycling Rates and under Drive Cycle Conditions," J. Electrochem. Soc., vol. 169, 2022.

Michele Braglia
Energy Systems Innovation Lead
Mobility Innovation Hub
HORIBA MIRA

Richard Stocker
Principal Engineer (Battery Solutions)
HORIBA US,
Mobility Innovation Hub
HORIBA MIRA

Materials Analysis of SOFC/SOEC Stack's Components using HORIBA's Scientific Instruments

Guillaume KESSLER

This article summarises measurements done on Solid Oxide Fuel Cell (SOFC)/ Solid Oxide Electrolysis Cell (SOEC) in HORIBA application lab using inhouse scientific instruments. It also gives an analysis of SOFC and SOEC market trend in testing, and summarises insights from research literature. The focus of this review was introducing materials analysis in SOFC/SOEC sector and explaining application of HORIBA's scientific instruments in this sector. It was highlighted that SOFC/SOEC markets not only needs materials analysis at the R&D step, but also along the production line. This includes measurements from the preparation of raw materials to in-line quality control and post-mortem analysis. HORIBA can provide scientific instruments to make a large number of these measurements. These measurements will help to improve SOFC/SOEC cells, stacks and systems performance and durability, which can be determined with HORIBA test stations and Balance of Plants.

Introduction

Due to climate change, Alternative Energy Solutions (AES) are under investigation to decarbonize societies. Among these solutions, fuel cells and electrolysis cells are considered as promising solutions to participate in the energy transition. Fuel cells (Solid Oxide Fuel Cell, Proton Exchange Membrane Fuel Cell…) convert certain fuels into electricity via an electrochemical reaction. Electrolysis cells (Solid Oxide Electrolysis Cell, Proton Exchange Membrane Electrolysis Cell, Alkaline Electrolysis Cell, Anion Exchange Membrane Electrolysis Cells…) convert electricity and certain fuels into other fuels (Figure 2, for SOFC and SOEC).

Fuel cells are promising because they can use renewable fuels such as Green Hydrogen, and their fuel to electricity efficiencies are higher than many energy systems such as gas turbine, Steam turbine and Diesel engine.[2] Many technologies of fuel cells exist, they are summarised in Table 1.

Electrolysers are promising because they can produce Hydrogen from water and electricity by emitting less CO_2 than the conventional steam-methane reforming process.[3] Also, electrolysers can produce synthetic fuels from non-fossil energy sources: CO_2 and H_2O.[4] Alkaline Electrolysis Cell (AEC), Proton Exchange Membrane Electrolysis Cell (PEMEC), Solid Oxide Electrolysis Cell (SOEC) and Anion Exchange Membrane Electrolysis Cell (AEMEC) are the four types of electrolyser technologies that are used today.

Table 1 Fuel Cell technologies.[2]

Type of fuel cell	Electrolyte	Operating Temperature	Fuel	Oxidant	Electrical Efficiency	Application
PEM (Proton Exchange Membrane)	Polymer: proton exchange membrane	50-80°C	Pure Hydrogen produced from hydrocarbons, melthanol or electrolysis	O_2/Air	40-50%	Transportation, H2 production.
AFC (Alkaline Fuel Cell)	Potassium hydroxide (KOH)	50-200°C	Pure Hydrogen or hydrazine liquid or methanol	O_2/Air	50-55%	Stationary (Apollo).
AEM (Anion Exchange Membrane)	Polymer	25-70°C	Hydrogen, methanol, maybe other alcohols and N-fuels (research)	O_2/Air	60%	Transportation, H2 production.
PAFC (Phosphoric Acid Fuel Cell)	Phosphoric Acid	160-210°C	Hydrogen produced from hydrocarbons or methanol	O_2/Air	40-50%	Stationary 100-400kW, Heavy duty, Air-independent propulsion (submarine)
MCFC (Molten Carbonate Fuel Cell)	Molten salts such as NO_3, SO_4, and CO_3	630-650°C	Hydrogen, CO, natural gas, propane, marine diesel	CO_2/O_2/Air	50-60%	Stationary
DMFC (Direct Methanol Fuel Cell)	Polymer	60-200°C	Liquid methanol	O_2/Air	40-55%	Power for man-portable tactical equipment, Battery chargers, and Autonomous power for test and training instrumentation
SOFC (Solid Oxide Fuel Cell)	Ceramic such as YSZ or CGO	600-1000°C	Hydrogen, natural gas or propane	O_2/Air	45-70%	Stationary, H2 production, CHP, Integrated coal gasification sysems, Integrated steam turbines, Electric vehicles (APU)

Components of a SOFC/SOEC Stack

Fuel Cells and Electrolysis Cells technologies differ in the materials used to make them. These technologies (Table 1) are not necessarily in direct competition; they can have different applications. This article focuses on the Solid Oxide Fuel Cell (SOFC) and Solid Oxide Electrolysis Cell (SOEC) technologies which are publicly known as High temperature Fuel Cell and High temperature Electrolysis Cell. When these technologies are used, they are part of a system made of a stack and auxiliaries. A stack is made of cells (fuel cells or electrolysis cells), stacked together with interconnectors, glass sealings, end plates and compression rods (not shown) (Figure 1). Interconnectors conduct gases through the stack and connect electrically cells together. Glass sealings seal gases compartment (H_2/air, H_2/atmosphere, and O_2/atmosphere compartments). End plates participate in the compression of the stack, provide electrical insulation between adjacent cells, and enable the stack to be connected to gases and electricity. Compression rods maintain the stack compressed. Depending on the kind of Solid Oxide Cells used (High temperature, Intermediate temperature, Low temperature), SOFC and SOEC stacks use different materials for the cathode, electrolyte, anode, and interconnectors. The most common materials used in SOFC stacks are listed in Table 2.

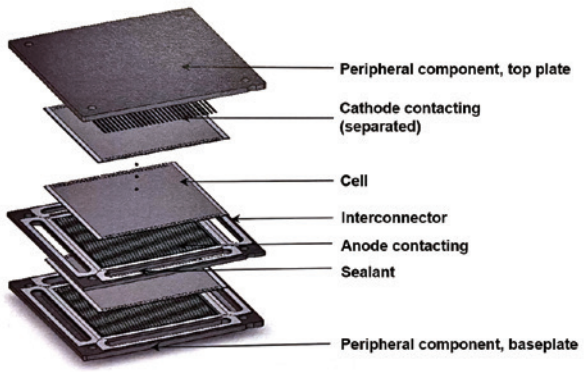

Figure 1 Exploded view of an assembled SOFC/SOEC planar cell,[5] where four rods and nuts at each corner crimp these planar cells together.

SOFCs and SOECs

SOFCs and SOECs are made of solid oxides, especially electroceramics. Some SOFC are reversible, so they can be used as SOEC.[7] The SOFC technology is well-known for its fuel tolerance and flexibility, high electrical efficiency (45-70%)[2] and high operating temperature (600-1000°C).[2] Three families of SOFC exist:

- High temperature SOFC, operating between 900°C and 1000°C;
- Intermediate temperature SOFC, operating between 700°C and 900°C;
- Low temperature SOFC, operating between 500°C and 700°C.

High temperature SOFCs are mostly used in Integrated

Table 2 Main materials used in SOFC.[6]

	Cathode	Electrolyte	Anode	Interconnect
High temperature SOFC (900-1000°C)	$La(Sr)MnO_3$	$Zr(Y)O_{2-x}$	$Ni\text{-}Zr(Y)O_2$	$LaCr(Mg)O_3$
Intermediate temperature SOFC (700-900°C)	$La(Sr)MnO_3$, $La(Sr)Co(Fe)O_{3-x}$	$Zr(Y)O_{2-x}$, $Ce(Gd)O_{2-x}$, $La(Sr)Ga(Mn)O_{3-x}$	$Ni\text{-}Zr(Y)O_2$	$Cr\text{-}Fe(Y_2O_3)$, $Inconel\text{-}Al_2O_3$
Low temperature SOFC (500-700°C)	$La(Sr)Co(Fe)O_{3-x}$	$Ce(Gd)O_{2-x}$, $La(Sr)Ga(Mn)O_{3-x}$	$Ni\text{-}Zr(Y)O_2$, $Ni\text{-}Ce(Gd)O_{2-x}$	Stainless steel

coal gasification systems and grid power distribution.[4] Intermediate temperature SOFCs are mainly used in Combined Heat and Power (CHP) systems,[8] integrated gas turbines[9] and vehicles (Auxiliar Power Unit).[10],[11] Low temperature SOFCs are principally used in Combined Heat and Power (CHP) systems, Auxiliary Power Units (APU) of electric vehicles.

SOFCs can use hydrogen as fuel, this will produce electricity and water (Figure 2): at the cathode $O_2(g)$ is reduced to O^{2-}; in the electrolyte O^{2-} ions are transported from the cathode to the anode and at the anode $H_2(g)$ is oxidised to $H_2O(g)$. Hydrogen can be produced by Solid Oxide Electrolysis Cell (SOEC) (Figure 2): at the cathode $H_2O(g)$ is reduced to $H_2(g)$ and O^{2-} ions; in the electrolyte O^{2-} ions are transported from the cathode to the anode and at the anode O^{2-} ions are oxidised to $O_2(g)$.

SOFC/SOEC Materials Analysis

Along the development cycle of a SOFC/SOEC stack, all constituting materials (interconnector, glass sealing, end plate, compression rod, cells) are analysed. In this article, a focus is made on the materials analysis of cells (SOFC/SOEC).

SOFC/SOEC Materials Properties and Performance

SOFCs/SOECs are characterised in terms of performance and durability. The performance of a SOFC/SOEC relates to its electrical efficiency, fuel utilisation, and power density at different current densities. The durability of a SOFC/SOEC has to do with the degradation of the performance over time and test cycles, in certain test conditions. The SOFC/SOEC performance and durability depend on the cell design, intrinsic properties of materials (electronic conductivity, ionic conductivity, thermal expansion coefficient, Oxygen self-diffusion coefficient, Surface exchange coefficient, Area Specific Resistance, porosity content, grains size, thickness, …)[12] and operating conditions (air and fuel compositions, temperature, gas pressure, …). To optimise SOFC/SOEC materials, the link between materials composition and microstructure, and performance and durability tests must be understood. For this, the materials composition and microstructure are analysed along the manufacturing steps, drafted in Figure 3, where firstly powders are prepared from raw materials, secondly inks are produced from powders, dispersants, solvents, and binders, thirdly inks are coated on a support and dried, fourthly cut to the right dimensions, and then fifthly coated layers are sintered.

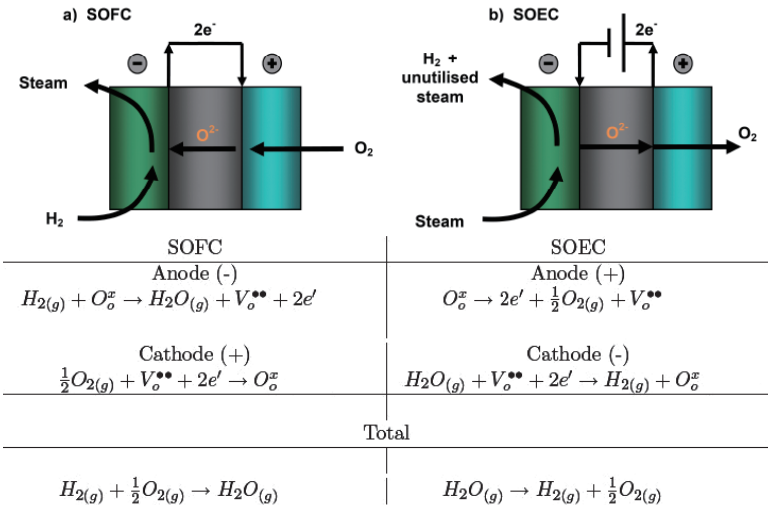

Figure 2 Schematics and electrochemical reactions taking place in a SOFC and a SOEC.[1]

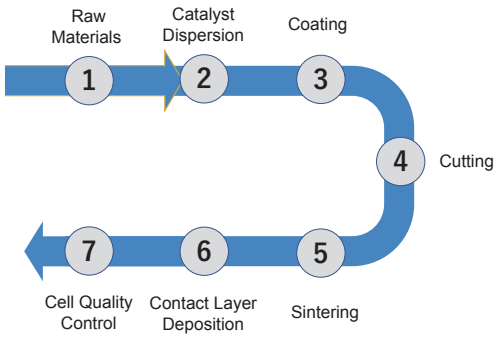

Figure 3 Schematic of the SOFC cell manufacturing.

Raw Materials Characterisation

Raw materials particles are characterised at line with instruments such as HORIBA XploRa™ PLUS confocal Raman microscope (Figure 4), HORIBA Partica LA-960V2 laser scattering particle size distribution analyzer (Figure 5), HORIBA nanoPartica SZ-100V2 Series nanoparticle analyzer (Figure 6) and HORIBA Partica CENTRIFUGE CN-300 centrifugal nanoparticle analyzer (Figure 7) to know their composition, crystallinity, size and distribution.

Ink Characterisation

Inks are characterised at line to know the particles size distribution in ink with HORIBA Partica LA-960V2 laser scattering particle size distribution analyzer (Figure 5) or with HORIBA SZ-100V2 Series nanoparticle analyzer (Figure 6) or with HORIBA Partica CENTRIFUGE CN-300 centrifugal nanoparticle analyzer (Figure 7), their rheology, viscosity, and zeta potential with HORIBA SZ-100V2 Series. Figure 8 shows results from HORIBA Partica LA-960V2 using the high concentration cell on an ink.

Figure 8 shows the results of the relationship between the scanning electron microscope (SEM) morphology of a PEFC (polymer electrolyte fuel cell), (not of SOFC here) cell coated layer and the particle size distribution of the ink analyzed by HORIBA Partica LA-960V2 using a high concentration cell. By using the high concentration cell, the particle size distribution of ink can be measured without diluting the ink as much as possible. Figures 8(a), (b), and (c) show that the particle size distribution is approximately 20 to 300 µm for Sample A, 0.2 to 1 µm for Sample B, and 0.1 µm for Sample C, respectively. Figures 8-(d), (e), and (f) show surface SEM images of the coated layers of Sample A, B, and C. Figures 8-(g), (h), and (i) show cross-sectional SEM images. The results show that the surface morphology of the coated layer becomes rougher and the variation of film thickness becomes larger when the inks with large particle size distribution are applied, that clearly confirms the effect of the catalyst dispersion solution on the microstructure of the coated layer.

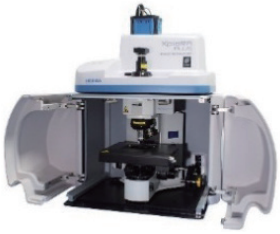

Figure 4 XploRA PLUS Raman Spectrometer - Confocal Raman Microscope.

Figure 5 Partica LA-960V2 Laser Scattering Particle Size Distribution Analyzer.

Figure 6 nanoPartica SZ-100V2 Series Nanoparticle Analyzer.

Figure 7 Partica CENTRIFUGE CN-300 Centrifugal Nanoparticle Analyzer.

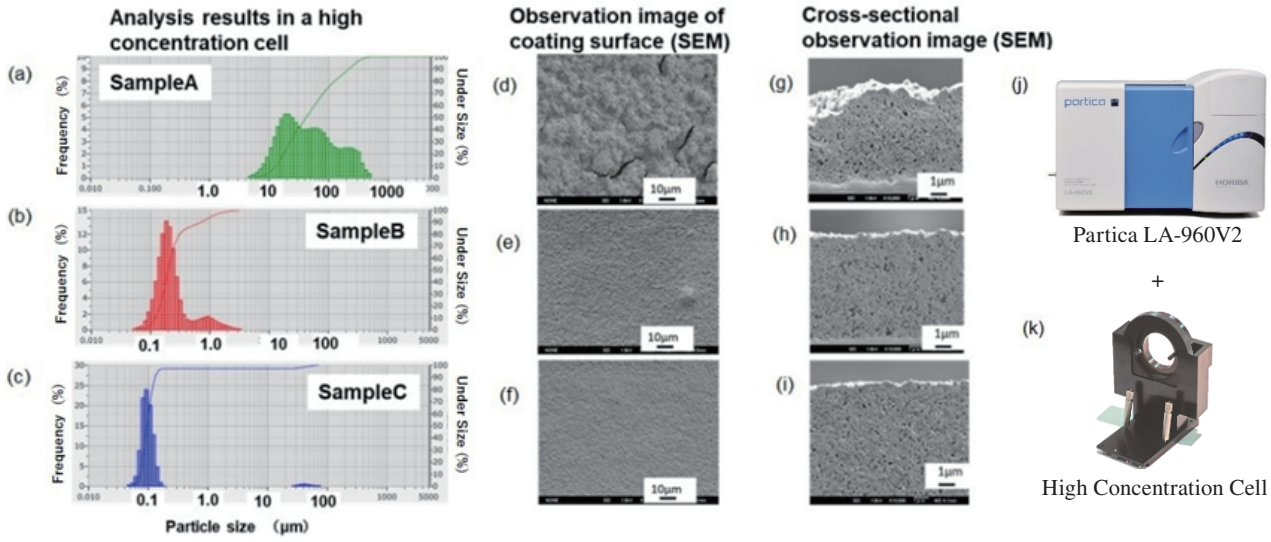

Figure 8 Particle size distributions (a-c) and SEM (d-i) data from different ink preparations. Particle size distributions were obtained with HORIBA Partica LA-960V (j) using High Concentration Cell (k) [Data provided by: Hirai & Sasabe Laboratory, Tokyo Institute of Technology, FC-Cubic].

Coating Characterisation

Nowadays, cells manufacturers want to measure the coated catalyst film thickness and catalyst loading inline, and ensure that the coated film shows a homogeneous distribution of the catalyst and the binder from the coating step to the drying step. Also, they want to detect defects (over thicknesses, impurities, pinholes, bubbles …).

HORIBA can provide an inline XRF solution to measure the amount and thickness of catalyst coated films inline. Figure 9 shows a photograph of the X-ray analysis head section (a) and an image of its X-ray analysis unit when installed in a roll-to-roll facility (b). As shown in Figure 9-(c), multiple X-ray analysis heads can be installed on the roll-to-roll coating film, or the X-ray analysis head can scan over the film while making measurements. HORIBA can also provide Raman solutions to detect defects and control the homogeneity of catalyst and binder in coated films. The example in Figure 10 shows Raman mapping (a) of the surface of a humid SOFC/SOEC air electrode using a HORIBA LabRAM Soleil Raman Spectrometer (c). The colour of each spectrum shown in Raman spectrum (b) corresponds to the colour of Raman mapping (a), where blue shows materials X, red shows materials X+C-H (polymer), and green and orange show Fe_3O_4 or Fe_2O_3 (impurity) respectively.

Sintering Characterisation

Today's market looks for inline instruments to detect defects and fast offline instruments to measure the thickness of sintered cells. HORIBA can provide inline XRF (Figure 9) or offline XRF solutions for defect detection and inline measurement of sintered layer thickness. Figure 11 shows the elemental composition analysis of dark impurity spots (b) on the SOFC anode surface using the HORIBA XGT-9000 (c), a micro X-ray fluorescence analyzer capable of elemental analysis and elemental mapping of small areas as small as φ10 µm. Figure 11-(a) shows the results of five elemental analyses, and it was found that a higher concentration of Fe_2O_3 was detected in the dark spot area than in the reference area, indicating that it was the cause of the dark spot. HORIBA can also provide a Raman solution to detect defects in the sintered layer. Figure 12 shows a microscope image and Raman mapping of a sintered SOFC anode surface by HORIBA LabRAM soleil. The colour of the Raman mapping image (a) corresponds to the colour of the Raman spectrum (b), showing red: materials X; red: ZrO2 ; blue: NiO; yellow: $BaTiO_2$ (impurity).

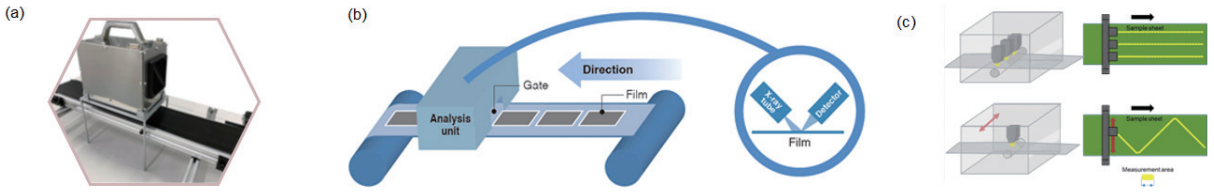

Figure 9 Photo (a) and Schematics (b and c) of inline XRF system.

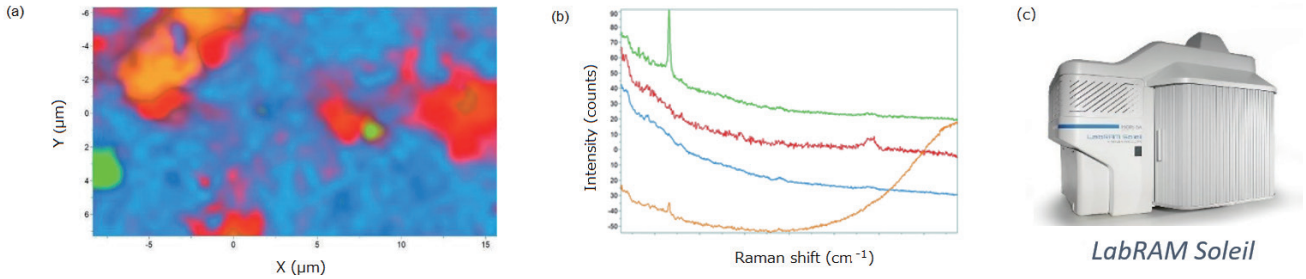

Figure 10 Raman mapping (a) and Raman spectrum (b) of a humid SOFC/SOEC air electrode measured with HORIBA LabRAM Soleil Raman Spectrometer (c). In blue: materials X; in red: materials X + C-H (polymer); in green and orange: Fe_3O_4 or Fe_2O_3 (impurity).

Post-mortem analysis

Once cells have been tested (performance and durability tests) with test stations such as the one produced by HORIBA FuelCon (Figure 13), some post-mortem analyses are done. In research, this is very common to do post-mortem analysis on cross sections with Scanning Electron Microscope (SEM)/Energy Dispersive X-ray (EDX) and Focused Ion Beam (FIB)-SEM. SEM-EDX enables to identify the chemical composition of layers (undesired phases, impurities…) and estimate both the quality of contacts and the porosity content. The FIB-SEM gives access to the 3D structure of layers (porosity content, contact surface, tortuosity…).[13] These data obtained from SEM are used to understand performance and durability tests results. For example, a loss of performance can be explained by the formation of an insulating phase at the electrode/electrolyte interface[14] or the electrode delamination[15] or the diffusion of species[14],[16] or something else. The post-mortem analysis can be completed with other characterisation technics such as Raman spectroscopy, X-ray Fluorescence spectroscopy and Glow Discharge Optical Emission Spectrometer (Figure 16), developed by HORIBA.

Raman spectroscopy was used to detect phase transformation in YSZ electrolyte enhanced by Nickel reduction.[17] It can also be used to monitor Cr poisoning behaviour of $La_{0.6}Sr_{0.4}Co_{0.2}Fe_{0.8}O_3$ (LSCF) cathodes.[18]

X-ray fluorescence spectroscopy can be used to identify, in a non-invasive way, Ni-S compound formed within a Ni-YSZ fuel electrode of a SOFC in contact with H_2S.[19] It can also be used to monitor the depletion and agglomeration of Ni in Ni-YSZ electrode[16] or a crack formation inside the YSZ electrolyte.[20]

In addition to composition and microstructural analyses, there is an interest in the industry to measure the mechanical properties of SOFC and SOEC cells.

SOFC/SOEC Stack and Hot-Box Materials Analysis

Current SOFC research is not only searching for new cathode, anode and electrolyte materials with greater performance and durability, but also for better interconnectors, glass sealings, end plates, compression rods and stack designs. That is why not only single cells are tested and characterised but also stacks and hot-box systems. Stacks and hot-box systems performance and durability can be determined with test stations such as HORIBA FuelCon test stations (Figures 14 and 15). The performance and durability test results will again be completed with measurements done from the raw materials preparation to the post-mortem analysis.

(a)

	Fe2O3	NiO	Y2O3	ZrO2	HfO2	CaO	Cr2O3	Cl	SO3
reference	0.05	28.4	7.9	61.1	2.2	0.3	0.03	0.00	0.00
Dark points									
N°1	0.11	30.2	7.8	59.3	2.2	0.3	0.02	0.02	0.00
N°2	0.18	28.7	7.9	60.6	2.2	0.3	0.03	0.03	0.00
N°3	0.09	29.9	7.8	59.9	2.2	0.2	0.02	0.00	0.00
N°4	0.24	32.3	7.5	57.4	2.2	0.2	0.05	0.05	0.00
N°5	0.21	29.6	7.8	59.9	2.1	0.2	0.04	0.05	0.00

(b)

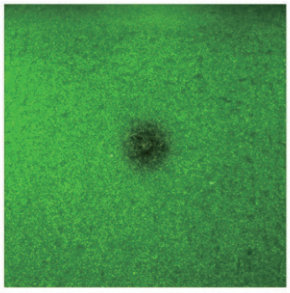

(c)

Figure 11 X-ray fluorescence signature (a) of a dark impurity spot (b) on a SOFC anode. A high concentration of Fe_2O_3 was detected with HORIBA XGT-9000 (c).

(a)

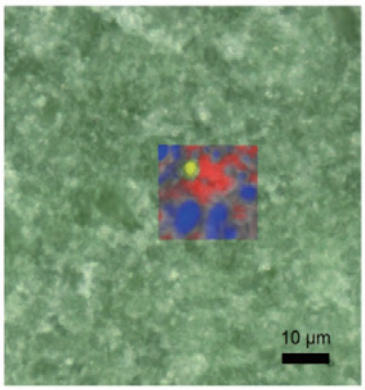

(b)

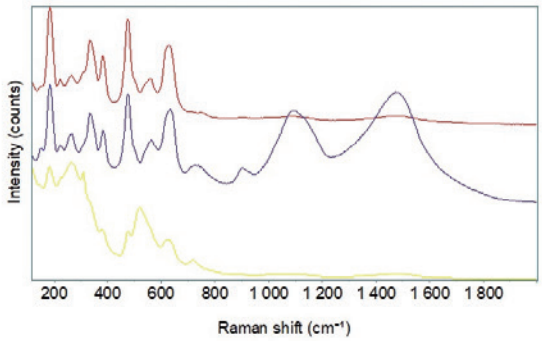

(c)

Figure 12 Microscope image and Raman mapping (a), and Raman spectrum (b) of a sintered SOFC anode measured with HORIBA LabRAM soleil (c). In red: materials X; in red: ZrO_2 ; in blue: NiO; in yellow: $BaTiO_2$ (impurity).

PEMFC/PEMEC cells, stacks, and systems Materials Analysis

Like HORIBA testing capability of SOFC/SOEC components and systems, HORIBA is capable of characterising PEMFC/PEMEC components and systems from materials to performance level. HORIBA GD-Profiler 2, coupled with HORIBA XploRa Plus Microscope are, for example, very useful to characterise the Bipolar Plates (PEM interconnectors) coating. By combining the elemental depth profile and the Raman spectrum of the Bipolar Plate coating, they helped to understand the impact of the coating morphology on the coating thickness (Figure 16).

Figure 16 shows an example of the characterization of a DLC coated film on a bipolar plate (PEM interconnector) using HORIBA GD-Profiler 2 (d) and the HORIBA XploRa Plus Microscope (e). The coated film of the bipolar plate must have a quality and thickness that satisfies high conductivity and corrosion resistance. Figure 16-(a) shows the Raman spectrum of the surface of the DLC-coated film of the bipolar plate (b). The quality of the DLC film can be evaluated by the ratio of the peak intensity of the G-band around 1580 cm-1 and the D-band around 1360 cm-1, which is derived from carbon, and the width at half maximum. Figure 16-(c) shows the elemental depth profile of a DLC-coated film on a bipolar plate. The vertical axis is indicated by the elemental emission intensity, or elemental concentration, and the horizontal axis is indicated by the sputtering time, which can be converted to the depth from the surface. The red line is the profile of carbon derived from the DLC film, and the black line is the profile of titanium, the base material of the bipolar plate. From this depth profile, the thickness of the DLC coated film can be analyzed. Thus, by combining the elemental depth profiles and Raman spectra, the influence of the DLC film quality of the bipolar plate on the thickness of the coating can also be investigated.

Conclusion

The main focus of research in SOFC/SOEC today, is the development of improved materials and designs to increase the efficiency and reduce the cost of these systems. This includes the development of new electrodes materials, electrolytes, and fuel cell components (interconnectors, glass sealings, end plates). Researchers are looking at ways to optimise the performance and durability of SOFCs/SOECs by analysing materials and their performance. The materials analysis can be made by Raman spectroscopy, X-ray Fluorescence, Dynamic light scattering, Glow Discharge Optical Spectrometer, Energy-dispersive X-ray spectroscopy and other technics. The main challenge of SOFC/SOEC industrials is the upscaling of SOFC/SOEC stacks production. To support this growth, HORIBA is offering inline monitoring solutions to control the quality of the process. Also, HORIBA is suppling end-of-line test stations to sinter stacks and validate their performance. Additionally, HORIBA provides measurement and test equipment for fuel cells and electrolysers systems development.

* Editorial note: This content is based on HORIBA's investigation at the year of issue unless otherwise stated.

Figure 13 Evaluator C1000-HT SOFC Fuel Cell Test Station.

Figure 14 EVALUATOR S25-HT.

Figure 15 S25-HT for Hot-Box systems.

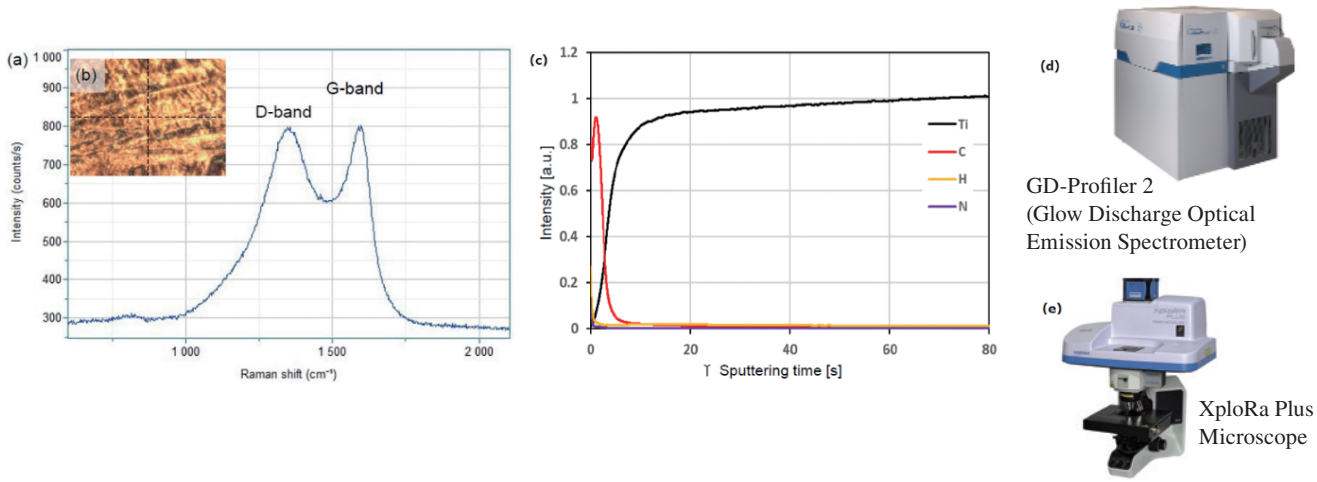

Figure 16 Raman spectrum obtained with HORIBA XploRa Plus Microscope (e) on a carbon coated surface of a bipolar plate and Optical image of the measurement area (a), and Elemental depth profile of the bipolar plate analysed by GD-Profiler 2 (d).[21]

References

[1] S. Skinner, 'Lecture 8', presented at the Lecture 8, Imperial College London, 2021.

[2] S. Skinner, 'MSE 411 Lecture 2 Fuel Cell Technology', presented at the MSE 411 Lecture 2 Fuel Cell Technology, Imperial College London, 2021.

[3] M. Katebah, M. Al-Rawashdeh, and P. Linke, 'Analysis of hydrogen production costs in Steam-Methane Reforming considering integration with electrolysis and CO2 capture', *Clean. Eng. Technol.*, vol. 10, p. 100552, Oct. 2022, doi: 10.1016/j.clet.2022.100552.

[4] S. H. Jensen, X. Sun, S. D. Ebbesen, R. Knibbe, and M. Mogensen, 'Hydrogen and synthetic fuel production using pressurized solid oxide electrolysis cells', *Int. J. Hydrog. Energy*, vol. 35, no. 18, pp. 9544-9549, Sep. 2010, doi: 10.1016/j.ijhydene.2010.06.065.

[5] M. Kusnezoff *et al.*, 'Progress in SOC Development at Fraunhofer IKTS'.

[6] S. Skinner, 'MSE 411 Lecture 6', presented at the MSE 411 Lecture 6, Imperial College London, 2021.

[7] M. Shen, F. Ai, H. Ma, H. Xu, and Y. Zhang, 'Progress and prospects of reversible solid oxide fuel cell materials', *iScience*, vol. 24, no. 12, p. 103464, Dec. 2021, doi: 10.1016/j.isci.2021.103464.

[8] E. J. Naimaster and A. K. Sleiti, 'Potential of SOFC CHP systems for energy-efficient commercial buildings', *Energy Build.*, vol. 61, pp. 153-160, Jun. 2013, doi: 10.1016/j.enbuild.2012.09.045.

[9] V. Zaccaria, D. Tucker, and A. Traverso, 'Gas turbine advanced power systems to improve solid oxide fuel cell economic viability', *J. Glob. Power Propuls. Soc.*, vol. 1, p. U96IED, Jun. 2017, doi: 10.22261/U96IED.

[10] D. J. L. Brett, A. Atkinson, N. P. Brandon, and S. J. Skinner, 'Intermediate temperature solid oxide fuel cells', *Chem. Soc. Rev.*, vol. 37, no. 8, pp. 1568-1578, Jul. 2008, doi: 10.1039/B612060C.

[11] J. Lawrence and M. Boltze, 'Auxiliary power unit based on a solid oxide fuel cell and fuelled with diesel', *J. Power Sources*, vol. 154, no. 2, pp. 479-488, Mar. 2006, doi: 10.1016/j.jpowsour.2005.10.036.

[12] G. Kessler, S. Skinner, and P. D. Z. Xie, 'Optimising the performance of the electrolyte barrier layer in Ruddlesden-Popper based fuel cells', MEng Thesis, Department of Materials Imperial College, Jun. 2021.

[13] O. Celikbilek, 'An experimental and numerical approach for tuning the cathode for high performance IT-SOFC', PhD thesis, Université Grenoble Alpes, 2018.

[14] S. Zarabi Golkhatmi, M. I. Asghar, and P. D. Lund, 'A review on solid oxide fuel cell durability: Latest progress, mechanisms, and study tools', *Renew. Sustain. Energy Rev.*, vol. 161, p. 112339, Jun. 2022, doi: 10.1016/j.rser.2022.112339.

[15] Z. Pan et al., 'On the delamination of air electrodes of solid oxide electrolysis cells: A mini-review', *Electrochem. Commun.*, vol. 137, p. 107267, Apr. 2022, doi: 10.1016/j.elecom.2022.107267.

[16] J. Villanova, S. Schlabach, A. Brisse, and A. Léon, 'X-ray fluorescence nano-imaging of long-term operated solid oxide electrolysis cells', *J. Power Sources*, vol. 421, pp. 100-108, May 2019, doi: 10.1016/j.jpowsour.2019.02.084.

[17] T. Ishiyama, H. Kishimoto, K. D.- Bagarinao, K. Yamaji, T. Horita, and H. Yokokawa, 'Gradual Conductivity Degradation of Nickel Doped Yttria Stabilized Zirconia by Phase Transformation at Operating Temperature', *ECS Trans.*, vol. 78, no. 1, pp. 321-326, May 2017, doi: 10.1149/07801.0321ecst.

[18] Y. Chen *et al.*, 'An effective strategy to enhancing tolerance to contaminants poisoning of solid oxide fuel cell cathodes', *Nano Energy*, vol. 47, pp. 474-480, May 2018, doi: 10.1016/j.nanoen.2018.03.043.

[19] W. M. Harris *et al.*, 'Three-Dimensional Microstructural Imaging of Sulfur Poisoning-Induced Degradation in a Ni-YSZ Anode of Solid Oxide Fuel Cells', *Sci. Rep.*, vol. 4, no. 1, p. 5246, Jun. 2014, doi: 10.1038/srep05246.

[20] L. Bernadet *et al.*, 'Enhanced diffusion barrier layers for avoiding degradation in SOFCs aged for 14000 h during 2 years', *J. Power Sources*, vol. 555, p. 232400, Jan. 2023, doi: 10.1016/j.jpowsour.2022.232400.

[21] C. Nishimura, T.-H. Wu, E. Iso, A. Fujimoto, P. Chapon, and J. Hirose, 'Proton Exchange Membrane Fuel Cell Bipolar Plate Analyses by GD-OES and Raman', *HORIBA Sci.*.

Guillaume KESSLER

Hydrogen Product Specialist,
ATS (Automotive Test Systems) - AES (Alternative Energy Systems- Hydrogen),
HORIBA FRANCE SAS

Production of Solid Oxide Fuel Cell and Electrolyzer Stacks using HORIBA FuelCon's Sintering Equipment

Mathias RACHAU

Fuel cell and electrolyzer solutions will play a major role in the development of the future Hydrogen economy helping to replace fossil fuels. Specifically, high temperature solid oxide cell (SOC) technology has important advantages such as increased efficiencies and the extended range of applications based on its fuel flexibility. The production of solid oxide cells and stacks is a key aspect on the way to an increased number and higher power level of system installations. HORIBA FuelCon provides SOC sintering, reduction and testing equipment that helps to scale-up the production to an industrial level and by that, to minimize the production costs. The present article provides insides on HORIBA FuelCon's solutions based on the specific SOC production steps.

Introduction

The "Paris Agreement" from 2015 that determined to limit global warming clearly below 2 K compared with pre-industrial times motivates the recently raised international activities aiming for reduction of global CO_2 emissions.

Reaching that goal will require to establish a throughout interaction between different energy sectors such as electricity, heat, chemistry and mobility based on alternative energy sources, mainly renewables.

The nature of renewable energy sources like wind and solar power implies the need for seasonal energy storage solutions.

Also, the associated reduction of fossil fuel utilization down to zero will only be successful if there is a way to substitute today's fossil feedstock sources in the chemical industry, the agri-food sector as well as the cement and steel production.

A basic and key and element for the implementation of all three mentioned aspects sector coupling, energy storage and fossil feedstock substitution will be Hydrogen.

A major part of the Hydrogen amounts required will be provided by electrolysis solutions. Amongst different electrolyzer technologies, the high-temperature Solid Oxide Electrolysis (SOEC) shows the highest efficiencies for pure water electrolysis and allows even to utilize CO_2 for provision of a $CO + H_2$ mixture, termed syngas, a major feedstock gas in the chemical industry. Moreover, the efficiency can be increased by heat coupling with subsequent exothermal processes like methanation and ammonia synthesis which play an important role for higher hydrocarbon production as well as for the agri-food sector.

The escalating Hydrogen demand leads to a rapidly rising request for electrolysis facilities, already now. Scaling up the capacities for SOEC cell and stack production requires specifically optimized and fully automated production equipment.

HORIBA FuelCon, as a provider of fuel cell and electrolyzer evaluation and manufacturing equipment for more than 20 years, offers a wide line-up of SOEC testing and production solutions in the full scope from cells to stacks. The same equipment is able to produce and test SOFC fuel cell stacks as well as rSOC reversible solid oxide stacks as these are just two more variants of the solid oxide technology.

The following article gives a detailed overview about solid oxide cell design and stack manufacturing processes. HORIBA FuelCon's associated production equipment will be illustrated providing insides of the applied technologies.

R&D and Quality tests for Cells

Solid oxide cells basically consist of a thin, sintered electrolyte foil that is applied with specific fuel and air electrode materials on each side.

A common electrolyte material is yttrium-oxide-stabilized zirconium dioxide (YSZ), a ceramic material that is gas tight in order to separate the reactants being in contact with the cell. While the electrolyte needs to be a good electrical insulator, it allows O^{2-} ions to pass. Aside from the high temperature that is needed to activate the O^{2-} ion conductivity (min. 600 °C), the O^{2-} ion transport is the main difference to PEM technology which is based on the transport of H^{+} ions (protons).

The fuel and air electrode materials are highly porous allowing the reacting gases to reach the three-phase boundary (electrolyte, electrode and gas). Also, a good electrical conductivity is desired to lead the electrons being released when O_2 split into O^{2-} ions. In order to assure the electrodes staying attached at the electrolyte when operating at high temperatures, the thermal expansion coefficients (TEC) of the electrodes need to be aligned to the electrolyte's properties.[1]

Commonly, the fuel and air electrode materials are printed on the electrolyte (e.g. by screen printing or tape casting) in form of a paste or slurry. After printing, the materials need to dry before they will be sintered at 1,000-1,400 °C. The materials being typically used are Nickel for the fuel electrode and lanthanum strontium manganite (LSM) for the air electrode.[1] Their main job is to catalyze the reactions, O^{2-} ion generation on air side and oxidation of the supplied fuel on the fuel side. In order to increase the electrochemical active zones and for TEC optimization, both electrodes are provided as a composite (cermet = ceramic + metal) of the basic materials mentioned above and electrolyte material (YSZ).[1]

To provide mechanical support to the cell, one of the layers need to be made thicker and by that representing a distinctive feature of the cell concept. Most manufactures use one of these 3 common cell types:

- Electrolyte supported cells (ESC, e.g. IKTS, Sunfire)
- Anode supported cells (ASC, e.g. Topsoe, Elcogen) or
- Metal supported cells (MSC, e.g. Ceres Power)

HORIBA FuelCon's cell test equipment accommodates all these cell types by using the integrated, fully ceramic cell

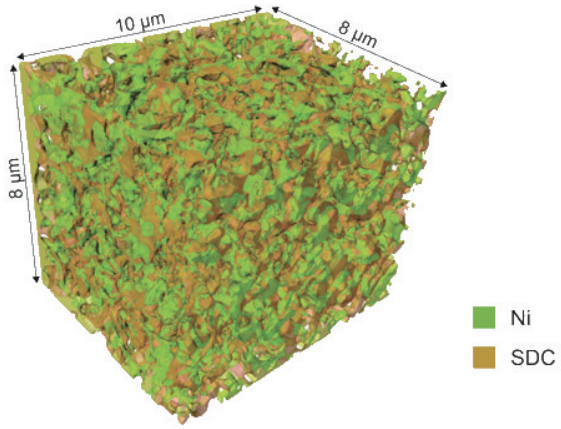

Figure 1 3D example of a Ni/SDC cermet, Gregor Kapun, Ljubljana.[3]

Cell type	Electrolyte Supported Cells (ESC)	Anode Supported Cells (ASC)	Metal Supported Cells (MSC)
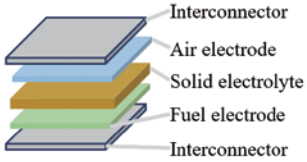	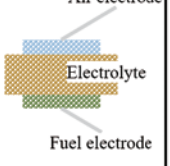	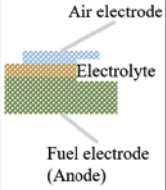	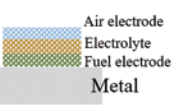
Example	IKTS, Sunfire	Topsoe, Elcogen	Ceres Power

Figure 2 SOC cell types.

housing for standard 5 × 5 cm cell designs as well as button cells. The all-ceramic cell housing approach provides a clean testing environment avoiding impurities. Mirror-finishing the ceramic surface improves the adhesion between ceramics. Thus, there is no need to use gaskets or glass sealing which allows to operate the cell in another test run or to apply academic examinations using HORIBA Scientific's wide range of sophisticated equipment such as Raman Spectroscopy.

Cell tests are supported by a number of proprietary features including a direct injection humidifier providing steam with a minimized noise or a direct combustion humidifier with zero noise, both for fuel cell and electrolysis operation at up to 100% steam.

Desulfurizer and reformer units being available for integration in HORIBA FuelCon's test stations allow for reformat fuel cell tests while a number of diverse supply media, such as H_2, CO_2, CO, CH_4, NH_3, support reformat simulation as well.

Electrolysis and reverse SOC operation based on steam and/or CO_2 is just another operation mode as the integrated 2-quadrant load provides smooth changing through the current origin.

Specific cell properties are determined by the integrated high-performance impedance spectrometer (EIS).

Stack Sintering

In order to receive an adequate power output for a specific SOFC/EC application, the single cells are piled on top of each other. The so called "stack" provides a higher voltage, equivalent to the number of cells, while the current through the complete stack is identical with the one applicable to a single cell.

In most cases, the cells are stacked in a bipolar manner meaning that the anode of one cell faces directly to the cathode of the next cell. The advantage of that method is a very simple electrical interconnection. However, since both air and fuel electrode need to be supplied with air and fuel gas just at the point of common contact, an additional interconnector layer is required to separate the two gas sections.

The interconnector plate has multiple functions as it needs to assure an optimal electrical contact and conductivity between the cells, provide main gas channels and stabilization to the stack and carries contacting and tightening elements. The interconnector material should have a high thermal conductivity to keep the temperature gradients inside the stack low and, at the same time, its thermal expansion coefficient (TEC) needs to meet the associated cell properties to prevent mechanical stress.[1] Finally, the interconnector's surface needs to build a tight oxide layer being protected from further oxidation and evaporation of metal contents while still keeping a good electrical conductivity in reducing and oxidizing atmospheres. A proven and widely used material for all these purposes is Crofer22APU, a ferritic high-temperature stainless steel.[1]

To contact the interconnector plate to the anode and cathode electrodes, additional materials are desired to fill the space between the rough surfaces of electrodes and interconnector.[1] Nickel foam or grids provide good results in reducing atmospheres at the fuel electrode.

The oxidizing atmosphere at the air electrode does not allow to use similar metal foams or grids due to their large active surface. A common solution is using electrically well conducting oxide ceramics with perovskite or spinell structures. Elements like manganese, lanthanum, strontium, chromium, kobold, copper or iron are part of these structures to obtain the required properties like the

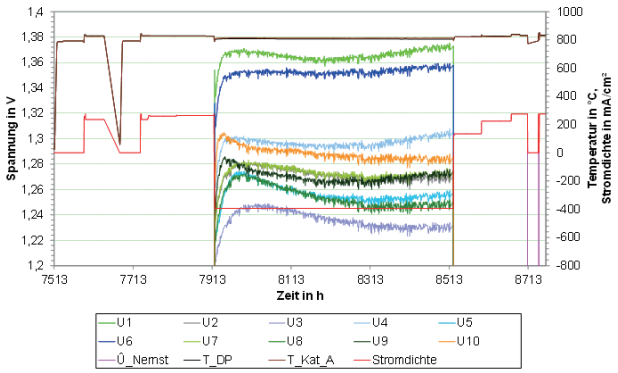

Figure 3 SOEC cell voltages @ 10...20 g/min steam over 600 h, IKTS.

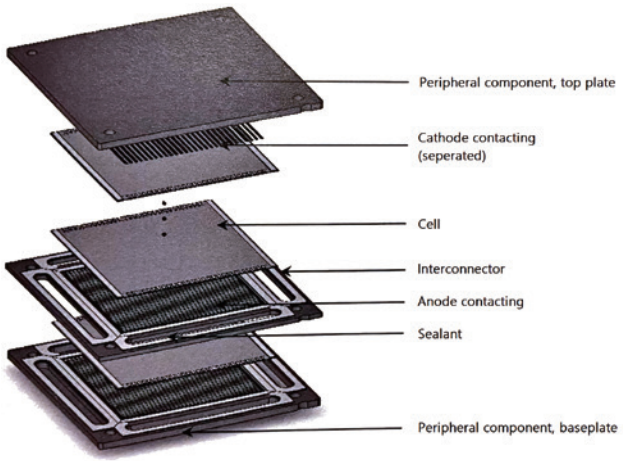

Figure 4 Explosion view of a planar, bipolarly assembled stack.[1]

good electrical conductivity.[1]

Usually, these contacting materials are applied in green state to the interconnector plate or to the air electrode where they build ceramic contacting bars. In this way, the oxide ceramics also represents a favored local barrier between interconnector and cathode that complicates evaporated chromium to reach the air electrode where it would harm the long-term cell performance.[1]

The air electrode connecting bars have contact to the opposite side after stack assembly already. Depending on the stack concept, they will be sintered (substance-to-substance bonds) or pressed with high pressure (force-fit bonds) at the next step.[1]

Before sintering can take place, the interconnector plates and the cell electrodes need to receive a sealant to keep the air and fuel gas inside the channels. Commonly, a glass solder, a special glass composition that allows to achieve the optimal TECs, is applied to the interconnector plate as a foil or paste. Beside sealing, the glass provides a leveling effect between the cells.[1]

Using HORIBA FuelCon's sintering stations, the stack is heated above typical operating temperatures up to 1.000 °C while air is supplied to both fuel and air side. During the sintering process, the stack releases organics coming from the glass solder binders which need to be removed safely. HORIBA FuelCon integrates purging and trace heating features as well as exhaust incinerator solutions.

The furnaces provided by HORIBA FuelCon come with multi-zone control to assure optimal heat distribution and can be arrange to accompany multiple stacks. Once the desired temperature is reached, the proprietary mechanical load design applying compression forces from above or from below the stack allows to compress the stack uniformly in order to secure the intended stack geometry. The maximum force level depends on the specific stack design and can reach up to 40 kN which is kept safely by HORIBA FuelCon's load concept, even at power outage or emergency shut down.

It is important to calculate the optimal glass amount, in order to receive optimal electrical contact after sintering without having surplus glass entering other parts of the stack. Using an open air side concept allows to waive the glass sealant at the air electrode which simplifies air side contacting as the green connecting bars described above can be sintered onto the air electrode, directly.[1]

Partly glass crystallization during the sintering process shifts the TEC toward the value of the cell. In addition, by crystallization, the glass viscosity increases by magnitude which provides the stack with the desired mechanical stability even at maximum operation temperatures.[1]

Stack Reduction

In preparation to the first real stack operation after sintering, the fuel electrode must be reduced using Hydrogen. The catalytic component, a nickel-containing material, forms nickel oxide (NiO) in air, although the nickel compound must be in the metallic state. Reduction with Hydrogen reduces nickel oxide to nickel. The reduced fuel electrode must have enough porosity to transfer the fuel gases. Good electrical conductivity is needed for decreasing the area specific resistance.

The time allowed to conduct the overall anode reduction process is a critical variable in stack production as this step may causes thermal and mechanical stress to the single cells and to the interconnection with other cells. Thus, Hydrogen is commonly diluted with nitrogen in order to control the speed of reduction and by that to protect the stack integrity.[1]

Using HORIBA FuelCon's sintering and reduction stations, the operator can control both the Hydrogen dilution and the flow rate of Hydrogen mixture in a well-defined way. A typical starting ratio is 20 % H_2 and 80 % N_2.[4] The test stand automation allows to control the duration and a continuous increase of Hydrogen content perfectly in accordance with manufacture's requirements.

The reduction process takes place at furnace temperatures between 700 - 800 °C which is below the sintering temperature. The sintering station's multi-zone furnace control follows the given temperature curves and limits precisely.

Stack Test

After sintering and reduction, one important test is to verify the stack's gas tightness. The glass sealant between cells and interconnectors needs to provide reliable leak protection.

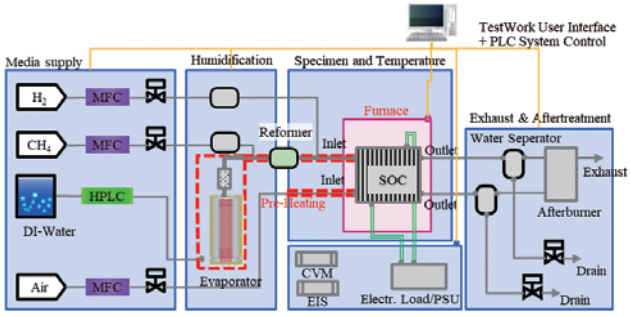

Figure 5 Overview of an SOC evaluation system.

HORIBA FuelCon's test stations offer diverse methods for leak testing. One is the fully automated online leakage test allowing to check for fuel and air electrode and for cross-over leakages during hot operation, depending on stack design. Another method is injecting noble gas like helium to fuel and/or air side. Helium traces found in the opposite gas compartment does indicate a cross-over leakage.

Once Hydrogen is supplied by 100 %, the OCV provides a more detailed picture about successful gas channel sealing as the OCV level highly depends on cross-over leak tightness. HORIBA FuelCon's sintering stations allow to measure the overall stack voltage as well as potentials of single cells or cell groups by multiple cell voltage measurement (CVM) options. By this means, manufacturing quality can be checked down to each single cell. High voltage measurement accuracy by superior input resistances for a large number of cells is the basis.

Polarization tests are a standard to receive quick information on the stack performance after manufacturing.[2] Typically, these tests are conducted under part load of the stack's nominal power. Depending on the intended application, the stack is operated in either fuel cell, electrolysis or reversible mode.

HORIBA FuelCon's sintering stations support all these operation variants in one rig. In most cases, focusing on Hydrogen and steam provision is sufficient for quality checks. If required, additional gases are available, e.g. NH_3 and CH_4 for ammonia and carbon fuel operation or CO_2 for co-electrolysis.

HORIBA FuelCon's proprietary direct injection humidifier provides large amounts of steam with a minimized noise. Together with the fully integrated 2-quadrant load concept, the stations support to change smoothly between fuel cell and electrolysis mode.

For all sintering and testing steps, HORIBA FuelCon supports closed stack concepts as well as open air or fuel side stack designs by proprietary furnace solutions that take care about chromium and silica prevention at the same time. Exhaust gases are cooled down and led to outside the station safely while sample ports allow manufacturers to check gas compositions continuously using gas analyzers from HORIBA. Defined exhaust interfaces enable operators to remove exhausts or to connect to sub-sequent processes.

Scaling-up Stack Production

The worldwide increasing CO_2 reduction goals will motivate the fuel cell and electrolyzer manufacturers to scale-up their production, rapidly. This concerns the cell and stack production in equal measure.

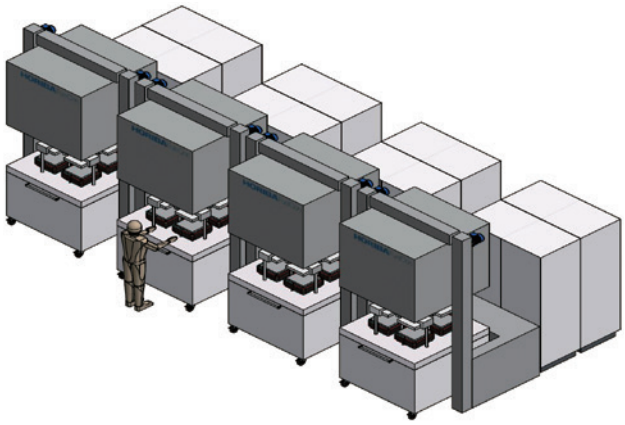

Figure 7 HORIBA FuelCon's Multiple Sintering Stations with 4-fold trolleys.

Higher volumes can be reached by installing additional production capacities. Optimizing the manufacturing processes and logistics does need to take place at the same time in order to increase the output of one production line to an optimum.

HORIBA FuelCon does provide next generation sintering and reduction stations, already now. Larger furnaces with space for multiple stacks are just a first step.

HORIBA FuelCon's proprietary trolley concept supports manufacturers with a movable and universal multi-stack platform that can be used for the whole range from stack assembly down to stack sintering, reduction and testing. As the trolleys include mechanical load systems for each

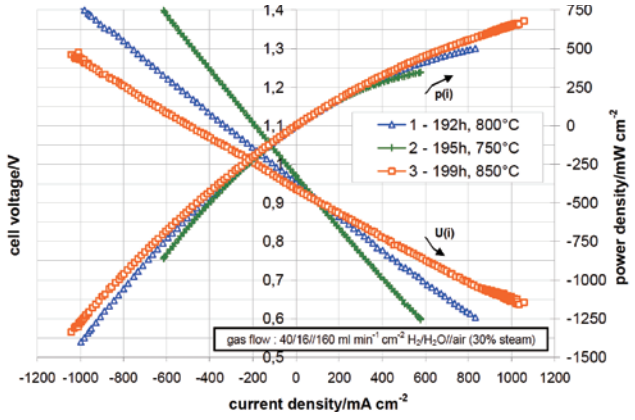

Figure 6 Polarization and i-p curves for reversible SOC operation at different temperatures.[2]

single position, the assembled stacks can be pre-compressed for safe stack transfer. Prepared like that, a trolley is in pool position for docking with the next allocated sintering station once the previous trolley is ready. That might be the case even if the cool down procedure has not finished yet as a quick cool down by furnace opening and stack transport may be acceptable at intermediate temperatures already to shorten the station's occupation time. Moreover, docking the trolley to HORIBA FuelCon's multiple sintering stations is conducted without manual help as they come with an automated docking solution. The described handling covering a number of compatible stack trolleys does allow to reduce the setup and production time to a minimum.

Conclusion

A detailed outline of solid oxide technological principles with HORIBA FuelCon's associated testing and production equipment and their upscaling concepts has been provided.

Solid oxide cell technologies comprise a number of sophisticated methods on cell and stack level, developed over the last decades. Diverse manufacturing steps are required, specifically differentiated according to the concrete SOC type and its fuel cell or electrolyzer application.

HORIBA FuelCon provides proven and progressive sintering, reduction and testing solutions for the broad range of existing SOC variants. Cell and stack manufacturers receive strong support for SOC production and for their upscaling strategy - saving time and resources.

* Editorial note: This content is based on HORIBA's investigation at the year of issue unless otherwise stated.

References

[1] Megel, S.: *Kathodische Kontaktierung in planaren Hochtemperatur-Brennstoffzellen*, Fraunhofer Verlag, **2009**

[2] Schiller, G.; Ansar, A.; Patz, O: *High Temperature Water Electrolysis Using Metal Supported Solid Oxide Electrolyser Cells (SOEC)*, Advances in Science and Technology Vol. 72, **2010**

[3] G. Kapun, S. Šturm, M. Marinšek, M. Gaberščcek: *Three-dimensional characterization of Ni-Sm0.2Ce0.8O2-δ cermet for SOFC anodes by high-resolution FIB-SEM Tomography*, The 16th European Microscopy Congress, **2018**

[4] Hagen, A.; Caldogno, R.; Capotondo; F.; Sun X.: *Metal Supported Electrolysis Cells*, energies, **2022**

Mathias Rachau
Application Expert
HORIBA FuelCon GmbH

Scientific Research Papers from HORIBA Group

From July 1, 2022 to March 31, 2023 on ScienceDirect

Towards tailpipe sub-23 nm solid particle number measurements for heavy-duty vehicles regulations

a: Barouch Giechaskiel, b: Matthias Schwelberger, c: Linus Kronlund, d: Christophe Delacroix, e: Logan A. Locke, f: M. Yusuf Khan, g: Tobias Jakobsson, Hua Lu Karlsson, h: Yoshinori Otsuki, i: Sawan Gandi, j: Stefan Keller, Benedikt Grob, k: Christos Dardiodis, Athanasios Mamakos

a: European Commission, Joint Research Centre (JRC)
b: Daimler Truck AG
c: Volvo GTT
d: Volvo Powertrain Engineering
e: Cummins Ltd
f: Cummins Inc.
g: Scania
h: Horiba Europe GmbH
i: Sensors Europe GmbH
j: AIP GmbH Co. KG
k: AVL List GmbH
Transportation Engineering Volume 9, September 2022, 100137

Indocyanine green conjugated phototheranostic nanoparticle for photodiagnosis and photodynamic therapy

a: Kenta Shinoda, Akane S. Suzuki, Toshinori Nakayama, bc: Akiko Suginami, Yutaka Tamura, d: Yasumitsu Moriya, e: Masamichi Yamashita, e: Tsutomu Tanaka, Yoshiharu Okamoto, f: Hiroshi Suito, Yasunori Akutsu, Hisahiro Matsubara, g: Kengo Saito, Hiroshi Shirasawa, h: Yoko Shinozaki, i: Kazuoki Isojima, j: Naohito Nakamura, Yasushi Miyauchi

a: Department of Immunology, Graduate School of Medicine, Chiba University
b: Department of Bioinformatics, Graduate School of Medicine, Chiba University
c: Molecular Chirality Research Center, Chiba University
d: Department of General Thoracic Surgery, Graduate School of Medicine, Chiba University
e: Department of Veterinary Clinical Medicine, School of Veterinary Medicine, Tottori University
f: Department of Frontier Surgery, Graduate School of Medicine, Chiba University
g: Department of Molecular Virology, Graduate School of Medicine, Chiba University
h: HORIBA Techno Service Co., Ltd.
i: Tateyama Machine Co., Ltd.
j: Kamakura Techno-Science, Inc.
Photodiagnosis and Photodynamic Therapy Volume 39, September 2022, 103041

Electro-thermal modelling of redox flow-batteries with electrolyte swapping for an electric ferry

a: Richard Woodfield, Stephan Glover, b: Robert Watson, c: Peter Nockemann, d: Richard Stocker

a: School of Mechanical and Aerospace Engineering, Queen's University Belfast
b: School of Aeronautical and Automotive Engineering, Loughborough University
c: School of Chemistry, The QUILL Research Centre, Queen's University Belfast
d: HORIBA MIRA
Journal of Energy Storage Volume 54, October 2022, 105306

Determination of Cabernet Sauvignon wine quality parameters in Chile by Absorbance-Transmission and fluorescence Excitation Emission Matrix (A-TEEM) spectroscopy

a: Jorge Zincker, Alvaro Gonzalez, ac: Doreen Schober, b: Adam Gilmore, Linxi Chen

a: Center for Research and Innovation, Vina Concha y Toro
b: HORIBA Instruments Inc.
c: Emiliana Organic Vineyards
Food Chemistry Volume 392, 30 October 2022, 133101

Quantitative assessment of visual microscopy as a tool for microplastic research: Recommendations for improving methods and reporting

a: Syd Kotar, Kristine Gesulga, Wenjian Lao, Leah M. Thornton Hampton, Stephan B. Weisberg, Charles S. Wong, b: Rae McNeish, c: Clare Murphy-Hagan, Andrew B. Gray, Samiksha Singh, d: Violet Renick, e: Chih-Fen T. Lee, Theresa Slifko f: Clare Steele, g: Bert van Bavel, gh: Amy Lusher, i: Charles Moore, Win Cowger, j: Elizabeth Minor, k: Paul Helm, m: Keith Rickabaugh, n: Hannah De Frond, Keenan Munno, Chelsea M. Rochman, o: Gaurav Amarpuri, p: Robert C. Andrews, q: Steven M. Barnett, rs: Silke Christiansen, s: Florian Vollnhals, t: Kevin Crampond, u: Fangni Du, v: Jeanne Hankett, w: Kay Ho, x: Julia Jaeger, y: Claire Lilley, z: Lei Mai, aa: Odette Mina, ab: Eunah Lee, ac: Sebastian Primpke, ad: Joakim Skovly, ae: Suja Sukumaran, af: Jennifer Van Brocklin, ag: Chenxi Wu

a: Southern California Coastal Water Research Project Authority
b: Department of Biology, California State University
c: Department of Environmental Sciences, University of California-Riverside
d: Orange County Sanitation District
e: Water Quality Laboratory, Metropolitan Water District of Southern California
f: Environmental Science and Resource Management, California State University
g: Norwegian Institute for Water Research
h: Department of Biological Sciences, University of Bergen
i: The Moore Institute for Plastic Pollution Research
j: Department of Chemistry and Biochemistry and Large Lakes Observatory, University of Minnesota Duluth
k: NatureWorks LLC
l: Environmental Monitoring & Reporting Branch, Ontario Ministry of the Environment
m: RJ Lee Group
n: Department of Ecology and Evolutionary Biology, University of Toronto
o: Eastman Chemical Company
p: Department of Civil and Mineral Engineering, University of Toronto
q: Barnett Technical Services
r: Fraunhofer Institute for Ceramics Technology and Systems (IKTS)
s: Institute for Nanotechnology and Correlative Microscopy (INAM)
t: Institut des Sciences de la Mer de Rimouski, Universite du Quebec a Rimouski
u: State Key Laboratory of Estuarine and Coastal Research, East China Normal University
v: BASF Corporation
w: US Environmental Protection Agency, Atlantic Coastal Environmental Sciences Division
x: Eurofins Environment Testing Australia
y: Eurofins SF Analytical Laboratories, Inc.
z: Center for Environmental Microplastics Studies, Guangdong Key Laboratory of Environmental Pollution and Health, School of Environment, Jinan University
aa: The Energy and Environmental Sustainability Laboratories, The Pennsylvania State University

ab: Horiba Instruments, Inc.
ac: Alfred Wegener Institute, Helmholtz Centre for Polar and Marine Research
ad: Eurofins Environmental Testing Norway AS
ae: Thermo Fisher Scientific
af: Department of Fisheries, Wildlife, and Conservation Sciences, Oregon State University
ag: State Key Laboratory of Freshwater Ecology and Biotechnology, Institute of Hydrobiology, Chinese Academy of Sciences
Chemosphere Volume 308, Part 3, December 2023, 136449

Isothermal crystallization of polyhydroxyalkanoate (PHA) utilizing Raman spectroscopy to follow chain packing as well as molecular motion

a: Fran Adar, b: Reva Street, c: Isao Noda

a: HORIBA Scientific, USA
b: Drexel University
c: University of Delaware
Spectrochimica Acta Part A: Molecular and Biomolecular Spectroscopy Volume 285, 15 January 2023, 121861

pH response and mechanical properties of Fe_2O_3-TeO_2-based glass/stainless steel enamel electrodes for pH sensors

a: Tadanori Hashimoto, Tomonari Kuno, Daiki Ito, Atsushi Ishihara, b: Yuji Nishio

a: Division of Chemistry for Materials, Graduate School of Engineering, Mie University
b: HORIBA Advanced Techno, Co., Ltd.
Heliyon Volume 9, Issue 1, January 2023, e12966

Non-destructive estimation of the cation composition of natural carbonates by micro-Raman spectroscopy

ab: Shu-hei Urashima, Hiroharu Yui, c: Mayu Morita, Shintaro Komatani

a: Department of Chemistry, Faculty of Science, Tokyo University of Science
b: Water Frontier Research Center, Research Institute for Science & Technology, Tokyo University of Science
c: HORIBA Techno Service Co., Ltd.
Analytica Chimica Acta Volume 1242, 15 February 2023, 340798

What determines accuracy of chemical identification when using microspectroscopy for the analysis of microplastics?

a: Hannah De Frond, b: Win Cowger, c: Violet Renick, d: Susanne Brander, e: Sebastian Primpke, f: Suja Sukumaran, g: Dounia Elkhatib, h: Steve Barnett, i: Maria Navas-Moreno, j: Keith Rickabaugh, k: Florian Vollnhals, l: Bridget O'Donnell, m: Amy Lusher, n: Eunah Lee, o: Wenjian Lao, p: Gaurav Amarpuri, q: George Sarau, kq: Silke Christiansen

a: Department of Ecology & Evolutionary Biology, University of Toronto
b: Moore Institute for Plastic Pollution Research
c: Environmental Services Department, Orange County Sanitation District
d: Department of Fisheries, Wildlife, and Conservation Sciences, Coastal Oregon Marine Experiment Station, Oregon State University
e: Alfred Wegener Institute, Helmholtz Centre for Polar and Marine Research, Biologische Anstalt Helgoland

f: Thermo Fisher Scientific
g: Oak Ridge Institute of Science Education, c/o U.S. Environmental Protection Agency, ORD/CEMM Atlantic Coastal Environmental Sciences Division
h: Barnett Technical Services
i: Lever Photonics
j: RJ Lee Group
k: Institute for Nanotechnology and Correlative Microscopy - INAM
l: HORIBA Scientific, USA
m: Norwegian Institute for Water Research, Oslo, Norway, Department of Biological Sciences, University of Bergen
n: HORIBA Instruments Inc.
o: Southern California Coastal Water Research Project Authority
p: Eastman Chemical Company
q: Fraunhofer Institute for Ceramics Technology and Systems - IKTS
Chemosphere Volume 313, February 2023, 137300

Absorbance-transmission and fluorescence excitation-emission matrix (A-TEEM) with multi-block data analysis and machine learning for accurate intraregional classification of Barossa Shiraz wine

a: Ranaweera K.R. Ranaweera, ab: Susan E.P. Bastian, Dimitra L. Capone, David W. Jeffery, c: Adam M. Gilmore

a: Department of Wine Science and Waite Research Institute, The University of Adelaide (UA)
b: Australian Research Council Training Centre for Innovative Wine Production
c: HORIBA Instruments Inc.
Food Control Volume 144, February 2023, 109335

Effect of natural and forced charge air humidity on the performance and emissions of a compression-ignition engine operating at high warm altitude

a: Jose Ramon Serrano, Jaime Martin, Pedro Piqueras, Roberto Tabet, b: Javier Gomez

a: Universitat Politecnica de Valencia, Spain
b: HORIBA Europe GmbH, Germany
Energy Volume 266, March 2023, 126409

Machine learning for classifying and predicting grape maturity indices using absorbance and fluorescence spectra

ab: Claire E.J. Armstrong, Vinay Pagay, David W. Jeffery c: Adam M. Gilmore, ad: Paul K. Boss

a: Australian Research Council Training Centre for Innovative Wine Production, The University of Adelaide
b: School of Agriculture, Food and Wine, and Waite Research Institute, The University of Adelaide
c: HORIBA Instruments Inc.
d: CSIRO Agriculture and Food
Food Chemistry Volume 403, 1 March 2023, 134321

Influence of nitro group on solvatochromism, nonlinear optical properties of 3-morpholinobenzanthrone: Experimental and theoretical study

a: Anup Thomas, b: Elena M. Kirilova, c: B.V. Nagesh, B. Siddlingeshwar, d: Krishna Chaitanya, e: Reji Philip, f: S.R Manohara, g: H.C. Sudeeksha

a: Centre for Computational Research in Clean Energy Technologies, Sree Chitra Thirunal College of Engineering

b: Department of Chemistry, Daugavpils University

c: Department of Physics, M.S. Ramaiah Institute of Technology, (Autonomous Institute affiliated to VTU)

d: School of Chemical Sciences, SRTM University

e: Light and Matter Physics Group, Raman Research Institute

f: Nano-Composites and Materials Research Lab, Department of Physics, Siddaganga Institute of Technology, (Autonomous Institute affiliated to VTU)

g: HORIBA India Scientific

Journal of Photochemistry and Photobiology A: Chemistry Volume 437, 1 March 2023, 114434

* Editorial note: This content is based on HORIBA's investigation at the year of issue unless otherwise stated.

HORIBA World-Wide Network

JAPAN

HORIBA, Ltd.

2 Miyanohigashi-cho, Kisshoin, Minami-ku, Kyoto, 601-8510, Japan
Phone : (81)75-313-8121 Fax : (81)75-321-8312

Biwako Factory
1-15-1, Noka, Otsu, Shiga, 520-0102, Japan
Phone : (81)-77-548-6130 Fax : (81)-77-548-6193

Saiin Factory
43-1 Nishimizosaki-cho, Saiin, Ukyo-ku, Kyoto, 615-0046, Japan
Phone : 81-75-323-7067 Fax : 81-75-323-7085

Tokyo Branch
Kanda Awaji-cho Nichome Building, 2-6 Kanda Awaji-cho, Chiyoda-ku, Tokyo, 101-0063, Japan
Phone : 81-3-6206-4711 Fax : 81-3-6206-4720

Tokyo Sales Office
Kanda Awaji-cho Nichome Building, 2-6 Kanda Awaji-cho, Chiyoda-ku, Tokyo, 101-0063, Japan
Phone : 81-3-6206-4721 Fax : 81-3-6206-4730

Hokkaido Sales Office
6F Park East Sapporo, 1-3 Minami Ichijo Higashi, Chuo-ku, Sapporo, Hokkaido, 060-0051, Japan
Phone : 81-11-207-1800 Fax : 81-11-207-1802

Tohoku Sales Office
4-21-8 Izumichuo, Izumi-ku, Sendai, Miyagi, 981-3133, Japan
Phone : 81-22-776-8251 Fax : 81-22-772-6727

Tochigi Sales Office
1F Flora Building, 1-9-15 Higashishukugo, Utsunomiya, Tochigi, 321-0953, Japan
Phone : 81-28-634-7051 Fax : 81-28-634-6099

Yokohama Sales Office
1F ShinYokohama Mineta Building, 2-3-19 Shinyokohama, Kohoku-ku, Yokohama, 222-0033, Japan
Phone : 81-45-478-7017 Fax : 81-45-478-7029

Nagoya Sales Office
4F BIZrium Nagoya, 3-1-17 Noritakeshinmachi, Nishi-ku, Nagoya, Aichi, 451-0051, Japan
Phone : 81-52-433-3450 Fax : 81-52-433-3460

Toyota Sales Office
2-23 Tsukasa-cho, Toyota, Aichi, 471-0831, Japan
Phone : 81-565-37-8510 Fax : 81-565-37-8511

Hamamatsu Sales Office
221-1 Sanjino-cho, Minami-ku, Hamamatsu, Shizuoka, 430-0816, Japan
Phone : 81-53-468-7780 Fax : 81-53-468-7781

Osaka Sales Office
4F ShinOsaka UenoToyo Building, 7-4-17 Nishinakajima, Yodogawa-ku, Osaka, 532-0011, Japan
Phone : 81-6-6390-8011 Fax : 81-6-6390-8012

Shikoku Sales Office
9-9 Imazato-cho, Takamatsu, Kagawa, 760-0078, Japan
Phone : 81-87-867-4800 Fax : 81-87-867-4801

Hiroshima Sales Office
1F Furuta Building, 2-5-27 Miyanomachi, Fuchu-cho, Aki-gun, Hiroshima, 735-0005, Japan
Phone : 81-82-288-4433 Fax : 81-82-286-0761

Kyusyu Sales Office
1F Hakata Fukoku Seimei Building, 8-30 Tenyamachi, Hakata-ku, Fukuoka, 812-0025, Japan
Phone : 81-92-292-3593 Fax : 81-92-292-3594

HORIBA Advanced Technology Center
11-5 Hokotate-cho, Kamitoba, Minami-ku, Kyoto, 601-8116, Japan
Phone : 81-75-693-2300 Fax : 81-75-693-2350

Kutsuki Training Center
335-10 Tochu, Kutsuki, Takashima, Shiga, 520-1425, Japan
Phone : 81-740-38-3127 Fax : 81-740-38-3126

HORIBA STEC, Co., Ltd.

11-5 Hokotate-cho, Kamitoba, Minami-ku, Kyoto, 601-8116, Japan
Phone : (81)-75-693-2300 Fax : (81)-75-693-2350

Aso Factory
Torikokogyodanchi, 358-11, Koumaibata, Toriko, Nishiharamura, Aso-gun, Kumamoto, 861-240, Japan
Phone : (81)-96-279-2921 Fax : (81)-96-279-3364

Fukuchiyama Technology Center
11-1 Miwa-cho Miwa, Fukuchiyama, Kyoto, 620-1445 Japan
Phone : (81)-773-59-2070 Fax : (81)-773-59-2074

Tokyo Sales Office
5F Kanda Awaji-cho Nichome Building, 2-6 Kanda Awaji-cho, Chiyoda-ku, Tokyo, 101-0063, Japan
Phone : 81-3-6206-4731 Fax : 81-3-6206-4740

Tohoku Sales Office
4-21-8 Izumichuo, Izumi-ku, Sendai, Miyagi, 981-3133, Japan
Phone : 81-22-772-6717 Fax : 81-22-772-6727

Yamanashi Sales Office
3F Daita Building, 2-14-13, Marunouchi, Kofu, Yamanashi, 400-0031, Japan
Phone : 81 55-231-1351 Fax : 81- 55-231-1352

Nagoya Sales Office
4F BIZrium Nagoya, 3-1-17 Noritakeshinmachi, Nishi-ku, Nagoya, Aichi, 451-0051, Japan
Phone : 81-52-433-3451 Fax : 81-52-433-3461

Kyushu Chuo Sales Office
Torikokogyodanchi, 358-11 Koumaibata, Toriko, Nishiharamura, Aso-gun, Kumamoto, 861-2401, Japan
Phone : 81-96-279-2922 Fax : 81-96-279-3364

HORIBA Advanced Techno, Co.,Ltd.

2 Miyanohigashi-cho, Kisshoin, Minami-ku, Kyoto, 601-8551, Japan
Phone : (81)-75-321-7184 Fax : (81)-75-321-7291

Factory
2 Miyanohigashi-cho, Kisshoin, Minami-ku, Kyoto, 601-8551, Japan
Phone : 81-75-321-1215 Fax : 81-75-321-1079

Tokyo Sales Office
Kanda Awaji-cho Nichome Building, 2-6 Kanda Awaji-cho, Chiyoda-ku, Tokyo, 101-0063, Japan
Phone : 81-3-6206-4751 Fax : 81-3-6206-4760

Tohoku Sales Office
4-21-8 Izumichuo, Izumi-ku, Sendai, Miyagi, 981-3133, Japan
Phone : 81-22-776-8253 Fax : 81-22-772-6727

Nagoya Sales Office
4F BIZrium Nagoya, 3-1-17 Noritakeshinmachi, Nishi-ku, Nagoya, Aichi, 451-0051, Japan
Phone : 81-52-433-3452 Fax : 81-52-433-3462

Osaka Sales Office
4F ShinOsaka UenoToyo Building, 7-4-17 Nishinakajima, Yodogawa-ku, Osaka, 532-0011, Japan
Phone : 81-6-6390-8211 Fax : 81-6-6390-8222

Shikoku Satellite Office
9-9 Imazato-cho, Takamatsu, Kagawa, 760-0078, Japan
Phone : 81-87-867-4841 Fax : 81-87-867-4842

Kyusyu Sales Office
1F Hakata Fukoku Seimei Building, 8-30 Tenyamachi, Hakata-ku, Fukuoka, 812-0025, Japan
Phone : 81-92-292-3595 Fax : 81-92-292-3596

Kyushu Chuo Sales Office
Torikokogyodanchi, 358-11, Koumaibata, Toriko, Nishiharamura, Aso-gun, Kumamoto, 861-240, Japan
Phone : 81-96-234-8035 Fax : 81-75-321-7291

HORIBA TECHNO SERVICE Co., Ltd.

2 Miyanohigashi, Kisshoin, Minami-ku, Kyoto, 601-8305, Japan
Phone : (81)-75-313-8125 Fax : (81)-75-321-5647

Tokyo Service Station
4F Kanda Awaji-cho Nichome Building, 2-6 Awaji-cho, Kanda, Chiyoda-ku,Tokyo, 101-0063, Japan
Phone : 81-3-6206-4750 Fax : 81-3-6206-4742

Hokkaido Sevice Station
6F Park East Sapporo, 1-3 Minami Ichijo Higashi, Chuo-ku, Sapporo, Hokkaido, 060-0051, Japan
Phone : 81-11-207-1801 Fax : 81-11-207-1802

Tohoku Service Station
4-21-8 Izumichuo, Izumi-ku, Sendai, Miyagi, 981-3133, Japan
Phone : 81-22-776-8252 Fax : 81-22-772-6727

Fukushima Service Station
101 Office Tatsumi, 5-13-17 Saikon, Koriyama, Fukushima, 963-8862, Japan
Phone : 81-24-925-9311 Fax : 81-24-925-9312

Tochigi Service Station
1F Flora Building, 1-9-15 Higashishukugo, Utsunomiya, Tochigi, 321-0953, Japan
Phone : 81-28-634-6098 Fax : 81-28-634-6099

Chiba Service Station
1-8-12 Goichuo-higashi, Ichihara, Chiba, 290-0054,Japan
Phone : 81-436-24-3914 Fax : 81-436-24-0642

Kashima Service Station
1-4-35 Kamisu, Kamisu, Ibaraki, 314-0143, Japan
Phone : 81-299-91-0808 Fax : 81-299-92-9561

Tsukuba Service Station
203 Tsukuba Cityia Moi Building, 5-20-2 Kenkyugakuen, Tsukuba, Ibaraki, 305-0817, Japan
Phone : 81-29-863-7311 Fax : 81-29-859-5221

Saitama Service Station
1F Higashikawaguchi Garden Plaza, 1-6-1 Totsukahigashi, Kawaguchi, Saitama, 333-0802, Japan
Phone : 81-48-298-6871 Fax : 81-48-298-6880

Nishitokyo Service Station
1F The-Macrocosm, 3-37-34 Izumi, Kokubunji, Tokyo, 185-0024, Japan
Phone : 81-42-322-3211 Fax : 81-42-322-3210

Yokohama Service Station
1F Plime ShinYokohama Building, 2-3-19 Shinyokohama, Kohoku-ku, Yokohama, Kanagawa, 222-0033, Japan
Phone : 81-45-478-7018 Fax : 81-45-478-7029

Fuji Service Station
1F Suzuki Building, 4-7 Suzukawahigashi-cho, Fuji, Shizuoka, 417-0012, Japan
Phone : 81-545-33-3152 Fax : 81-545-33-3159

Hamamatsu Service Station
221-1 Sanjino-cho, Minami-ku, Hamamatsu, Shizuoka, 430-0816, Japan
Phone : 81-53-464-1339 Fax : 81-53-464-6528

Tokai Service Station
2-23 Tsukasa-cho, Toyota, Aichi, 471-0831, Japan
Phone : 81-565-37-3510 Fax : 81-565-37-3520

Nagoya Service Station
1F Riverpage, 3-203 Kamiyashiro, Meito-ku, Nagoya, Aichi, 465-0025, Japan
Phone : 81-52-705-0711 Fax : 81-52-705-0710

Hokuriku Service Station
1F Ichigo-Toyama-Eki-Nishi Building, 1-1-19 Jintsu-Honmachi, Toyama, 930-0008, Japan
Phone : 81-76-422-6112 Fax : 81-76-422-6446

Mie Service Station
1F Taiyo-Seimei Yokkaichi Building, 1-1-18 Unomori, Yokkaichi, Mie, 510-0074, Japan
Phone : 81-59-340-6061 Fax : 81-59-340-6063

Kyoto Service Station
2 Miyanohigashi, Kisshoin, Minami-ku, Kyoto, 601-8305, Japan
Phone : 81-75-325-5291 Fax : 81-75-321-5647

Osaka Service Station
4F ShinOsaka UenoToyo Building, 7-4-17 Nishinakajima, Yodogawa-ku, Osaka, 532-0011, Japan
Phone : 81-75-325-5291 Fax : 81-75-321-5647

Hyogo Service Station
381 Nnjyo, Himeji, Hyogo, 670-0952, Japan
Phone : 81-79-284-8320 Fax : 81-79-284-8321

Shikoku Service Station
9-9 Imazato-cho, Takamatsu, Kagawa, 760-0078, Japan
Phone : 81-87-867-4821 Fax : 81-87-867-4822

Okayama Service Station
1-12-35 Tsurajima, Kurashiki, Okayama, 712-8012, Japan
Phone : 81-86-448-9760 Fax : 81-86-446-5637

Hiroshima Service Station
1F Furuta Building, 2-5-27 Miyanomachi, Fuchucho, Aki-gun, Hiroshima, 735-0005, Japan
Phone : 81-82-283-3378 Fax : 81-82-286-0761

Yamaguchi Service Station
1F 3rd Hanada Building, 1-72 Hashimoto, Shunan, Yamaguchi, 745-0022, Japan
Phone : 81-834-34-8684 Fax : 81-834-34-8685

Kyusyu Service Station
1F Hakata Fukoku Seimei Building, 8-30 Tenyamachi, Hakata-ku, Fukuoka, 812-0025, Japan
Phone : 81-92-292-3597 Fax : 81-92-292-3598

Oita Service Station
1F Tsuruwa Building, 2-2-37 Hagiwara, Oita, 870-0921, Japan
Phone : 81-97-551-3982 Fax : 81-97-551-3889

Kumamoto Service Station
Toriko-kogyodanchi, 358-11, Koumaibata, Toriko, Nishiharamura, Aso-gun, Kumamoto, 861-2401, Japan
Phone : 81-96-279-2985 Fax : 81-96-279-2986

HORIBA World-Wide Network

BRAZIL

HORIBA Instruments Brasil, Ltda.
Rua Presbitero Plinio Alves de Souza, 645, Loteamento Multivias, Jardim Ermida II - Jundiai Sao Paulo - CEP 13.212-181 Brazil
Phone : (55)-11-2923-5400 Fax : (55)-11-2923-5490

TCA/HORIBA Sistemas de Testes Automotivos Ltda.
Avenida Luigi Papaiz, 239 - Campanário, Diadema, São Paulo, Brazil CEP: 09931-610
Phone : (55)-11-4224-0200 Fax : (55)-11-4227-3133

CANADA

HORIBA Canada, Inc.
Unit102, 5555 North Service Road Burlington, Ontario, Canada, L7L 5H7
Phone : (1)-905-335-0234 Fax : (1)-905-331-2362

London Office
347 Consortium Court, London, Ontario, Canada, N6E 2S8
Phone : 1-519-668-6920 Fax : 1-519-668-8437

U.S.A.

HORIBA Americas Holding Incorporated
9755 Research Drive, Irvine, CA 92618, U.S.A.
Phone : (1)-949-250-4811

HORIBA Instruments Incorporated
9755 Research Drive, Irvine, CA 92618, U.S.A.
Phone : (1)-949-250-4811 Fax : (1)-949-250-0924

Ann Arbor Office
5900 Hines Drive, Ann Arbor, MI 48108, U.S.A.
Phone : (1)-734-213-6555 Fax : (1)-734-213-6525

Austin Office
9701 Dessau Road, Suite 605, Austin, TX 78754, U.S.A.
Phone : (1)-512-836-9560 Fax : (1)-512-836-8054

Canton Office
5449 Research Drive Canton, MI 48188, U.S.A.
Phone : (1)-800-445-9853 Fax : (1)-734-483-1592

Fletcher Office
270 Rutledge Road, Unit D Fletcher, NC 28732, U.S.A.
Phone : (1)-828-676-2801 Fax : (1)-828-676-2805

Houston Office
5390 Bay Oaks Drive, Pasadena, TX 77505, U.S.A.
Phone : 1-281-482-4334 Fax : 1-281-674-6058

Novato Field Office
359 Bel Marin Keys Blvd, #18, Novato, CA 94949, U.S.A.

HORIBA New Jersey Optical Spectroscopy Center
20 Knightsbridge Rd, Piscataway, NJ 08854, U.S.A.
Phone : +(1)-732-494-8660 Fax : +(1)-732-549-5125

Portland Office
7007 S.W. Cardinal Lane, Suite 185, Portland, OR 97224, U.S.A.
Phone : +(1)-503-624-9767 Fax : +(1)-503-968-3236

HORIBA Reno Technology Center
3740 Barron way Reno, Nevada 89511, U.S.A.
Phone : +(1)-775-358-2332 Fax : +(1)-775-358-0434

Sunnyvale Office
430 Indio Way, Sunnyvale CA 94085, U.S.A.
Phone : +(1)-408-730-4772 Fax : +(1)-408-730-8975

Tempe Office
1515 West University Drive, Suite 101 Tempe, AZ 85281, U.S.A.
Phone : +(1)-480-791-2203

Troy Office
2890 John R Road, Troy, MI 48083, U.S.A.
Phone : +(1)-248-689-9000 Fax : +(1)-248-689-8578

AUSTRIA

HORIBA (Austria) GmbH
Kaplanstrasse 5, A-3430 Tulln, Austria
Phone : +(43)-2272-65225 Fax : +(43)-2272-65225-45

CZECH

HORIBA Czech Olomouc Factory
Zeleznicni 512/7, 779 00 Olomouc, Czech Republic
Phone : +(420) 588 118 365 + (420) 588 118 393

HORIBA Czech Prague Office
Prumyslova 1306/7, CZ-10200, Praha 10, Czech Republic
Phone : +(420) 246 039 265

FRANCE

HORIBA Europe Holding SASU
14 Boulevard Thomas Gobert - CS 45002 - 91120 Palaiseau - France

HORIBA Europe Research Center
14 Boulevard Thomas Gobert - Passage Jobin Yvon CS 45002 - 91120 Palaiseau - France
Phone : +(33)-1-69-74-72-00 Fax : +(33)-1-69-31-32-20

HORIBA FRANCE SAS, Longjumeau Office
16-18, rue du Canal, 91165 Longjumeau Cedex, France
Phone : +(33)-1-69-74-72-00 Fax : +(33)-1-69-09-07-21

HORIBA FRANCE SAS, Lille Office
455 avenue Eugène Avinée - 59120 LOOS - France
Phone : +(33)-1-69-74-72-00 Fax : +(33)-3-20-59-18-08

HORIBA ABX SAS
Parc Euromédecine, rue du Caducée, BP7290, 34184 Montpellier Cedex 4, France
Phone : +33 (0)4 67 14 15 16 Fax : +33 4-67-14-15-17

GERMANY

HORIBA Europe GmbH / Oberursel Office
Hans-Mess-Str.6, D-61440 Oberursel, Germany
Phone : +(49)-6172-1396-0 Fax : +(49)-6172-1373-85

HORIBA Europe GmbH, Darmstadt Office
Landwehrstrasse 55, D-64293, Darmstadt, Germany
Phone : +(49)-6151-5000-0 Fax : +(49)-6151-5000-3865

HORIBA Europe GmbH, Dresden Office
Hugo-Junckers-Ring 1, 01109 Dresden, Germany
Phone : +(49)-351-8896807 Fax : +(49)-351-8896808

HORIBA Europe GmbH, Florsheim Office
Mariechen-Graulich-Straße 10-12a, 65439 Flörsheim, Germany
Phone : +49 6145 37699-12

HORIBA Europe GmbH, Hanover Office
Frankenring 14, D-30855 Langenhagen, Germany
Phone : +49 511-65523987 Fax : +49 511-54571751

HORIBA Europe GmbH, Korschenbroich Office
Friedrich-Ebert-Str. 9-11, D-41352 Korschenbroich, Germany
Phone : +(49)-2161-47537-0

HORIBA Europe GmbH, Leichlingen Office
Julius-Kronenberg-Str. 9, D-42799 Leichlingen, Germany
Phone : +(49)-2175-8978-0 Fax : +(49)-2175-897850

HORIBA Europe GmbH, Munich Office
Waldmeisterstr. 72-74/Robinienstr. 66, D-80935 Munich, Germany
Phone : +(49)-89-2444779-0 Fax : +(49)-89-2444779-10

HORIBA Europe GmbH, Potsdam Office
Dennis-Gabor-Str. 2, D-14469 Potsdam, Germany
Phone : +(49)-3316-4900-70 Fax : +(49)-3316-4900-74

HORIBA Europe GmbH, Stuttgart Office (Boeblingen)
Hanns-Klemm-Str. 56, D-71034 Boeblingen, Germany
Phone : +(49)-7031-677-9440 Fax : +(49)-7031-677-9450

HORIBA Europe GmbH, Stuttgart Office (Neuhausen)
Zabergaeustr. 3, D-73765 Neuhausen, Germany
Phone : +(49)-7158-933-800 Fax : +(49)-7158-933-899

HORIBA Europe GmbH, Wolfsburg Office
Klauskamp, Heinenkap II 38444 Wolfsburg, Germany
Phone : +(49)-5361-38653-16 Fax : +(49)-5361-38653-24

HORIBA Jobin Yvon GmbH
Neuhofstrasse 9, D_64625, Bensheim, Germany
Phone : 49(0)62-51-84-750 Fax : 49(0)62-51-84-7520

HORIBA FuelCon GmbH
Otto-von-Guericke-Allee 20, 39179 Barleben, Germany
Phone : +49 39203 514 400 Fax : +49 39203 514 409

BeXema GmbH
Otto-von-Guericke-Allee 20, 39179 Barleben, Germany
Phone : +49 39203 964 200

HORIBA Tocadero GmbH
Johann-Hittorf-Str. 8 12489 Berlin Germany
Phone : +49 (0)30 6392 3150 Fax : +49 (0)30 6392 3151

ITALY

HORIBA ITALIA Srl
Via Luca Gaurico 209 - 00143 ROMA,Italy
Phone : +(39)-6-51-59-22-1 Fax : +(39)-6-51-96-43-34

Torino Office
Via Feroggio, 30, 10151 Torino, Italy
Phone : +(39)-1-19-04-06-01 Fax : +(39)-1-19-00-04-48

HORIBA ABX SAS, Italy Branch
Viale Luca Gaurico 209/211, 00143 Roma, Italy
Phone : +(39)-6-51-59-22-1 Fax : +(39)-6-51-96-43-34

NETHERLANDS

HORIBA Europe GmbH, Netherlands Branch
Science Park Eindhoven 5080 (Industrial park " Ekkersrijt ") 5692 EA, Son, Netherlands
Phone : +(31)-40-2900240 Fax : +(31)-40-2900624

POLAND

HORIBA ABX Sp. z o.o.
Aleja Niepodleglosci 18, 02-653 Warszawa (Warsaw), Poland.
Phone : +(48)-22-673-2022 Fax : +(48)-22-673-2026

PORTUGAL

HORIBA ABX SAS, Portugal Branch
Alfrapark - Estrada de Alfragide n° 67, Edificio F - Piso 0 Sul, 2610-008 Amadora, Portugal
Phone : +(35)-12-14-72-17-70 Fax : +(35)-12-14-72-17-89

ROMANIA

HORIBA (Austria) GmbH, Romania Branch
B-dul.Republicii, nr. 164, Etaj Parter, Birourile nr. 3 si 4, Pitesti, 110177, Judetul Arges, ROMANIA
Phone : +(40)-348-807117 Fax : +(40)-348-807118

RUSSIA

HORIBA OOO
Altufievskoe shosse, 13, building 5, 127106, Moscow, Russia
Phone : +(7)-495-221-87-71 Fax : +(7)-495-221-87-68

Zelenograd Office
Office 106, 2nd West st., 1, build 1, 124460, Zelenograd city, Moscow, Russia
Phone : (+7)-499-995-09-54

SPAIN

HORIBA ABX SAS, Spain Branch
Calle Apolonio Morales. Num. 6 (Bajos), 28036 Madrid, Spain
Phone : +(34)-91-353-30-10 Fax : +(34)-91-353-30-11

HORIBA MIRA SPAIN, S.L.
Calle Oficios, nave 22, 04620 Vera (Almería), Spain
Phone : +(34)-950-39-11-53

SWEDEN

HORIBA Europe GmbH, Sweden Branch (Gothenburg)
Grimboasen 10 A, S-417 05 Gothenburg, Sweden
Phone : +(46)-10-161 1500 Fax : +(46)-10-161 1503

HORIBA Europe GmbH, Sweden Branch (Sodertalje)
Sydhamnsvagen 55-57, SE- 15138, Sodertalje, Sweden
Phone : +(46)-8-550-80701 Fax : +(46)-8-550-80567

TURKEY

HORIBA Europe GmbH, Istanbul Office
Veysel Karani Mahallesi, Colakoglu Sokak No: 10, Rings Rezidans D:23, PK: 34885, Sancaktepe / Istanbul, Turkey
Phone : +90 216 572 1166 Fax : +90 216 572 1167

HORIBA World-Wide Network

UNITED KINGDOM

HORIBA UK Limited
Kyoto Close Moulton Park Northampton NN3 6FL UK
Phone : +44 (0)1604 542500 Fax : +44 (0)1604 542699

HORIBA UK Finance Limited
Kyoto Close Moulton Park Northampton NN3 6FL UK
Phone : +(44) 1604 542500

HORIBA Jobin Yvon IBH Ltd.
133 Finnieston St. Glasgow G3 8HB, UK
Phone : +(44)-141-229-67-89 Fax : +(44)-141-229-67-90

HORIBA Test Automation Limited
Brook Court Whittington Hall Worcester WR5 2RX, UK
Phone : +(44)-1905-359359 Fax : +(44)-1905 359332

HORIBA MIRA Limited
Watling Street, Nuneaton, Warwickshire, CV10 0TU, United Kingdom
Phone : +(44)-24-7635-5000

Quatro Park
Unit 1, Quatro Park, Paycocke Road, Basildon, Essex, SS14 3GH, United Kingdom
Phone : +(44)-1268-290100

HORIBA MIRA Certification Limited
Watling Street, Nuneaton, Warwickshire, CV10 0TU, United Kingdom
Phone : +(44)-24-7635-5000

MIRA Service Limited
Watling Street, Nuneaton, Warwickshire, CV10 0TU, United Kingdom
Phone : +(44)-24-7635-5000

MIRA Technology Park Limited
Watling Street, Nuneaton, Warwickshire, CV10 0TU, United Kingdom
Phone : +(44)-24-7635-5000

MIRA UGV Limited
Suite 1.03, Technology Centre Nw05 Mira Technology Park, Watling Street, Nuneaton, Warwickshire, United Kingdom, CV10 0TU

CHINA

HORIBA INSTRUMENTS (SHANGHAI) CO., LTD
No.99, Chunxiu Rd, Anting Town, Jiading District, Shanghai, China 201804
Phone : +(86)-21-6952-2835 Fax : +(86)-21-6952-2823

HORIBA Technology (Suzhou) Co.,LTD.
No.1 building, Industry park, No.101 Chenmenjing Rd, Taicang, Jiangsu, China (215400)
Phone : +(86)-0512-3306-6388

HORIBA (China) Co., Ltd.
Room 1604, Building 1, No.185 Moyu Road, Anting Town, Jiading District, Shanghai, China, 201805
Phone : +(86)-21-6289-6060 Fax : +(86)-21-6289-5553

HORIBA (China) Trading Co., Ltd.
Unit D, 1F, Building A, Synnex International Park, 1068 West Tianshan Road, 200335, Shanghai, China
Phone : +(86)-21-6289-6060 Fax : +(86)-21-6289-5553

Beijing Branch
12F, Metropolis Tower, No.2, Haidian Dong 3 Street, Beijing, 100080, China
Phone : +(86)-10-8567-9966 Fax : +(86)-10-8567-9066

Guangzhou Branch
Room 1611/1612, Goldlion Digital Network Center, 138 Tiyu Road East, Guangzhou 510620, China
Phone : +(86)-20-3878-1883 Fax : +(86)-20-3878-1810

HORIBA Precision Instruments (Beijing) Co., Ltd.
Building1, No.3 yuan, Xixing Road, Houshayu Town, Shunyi District, Beijing, 101318 China
Phone : +86-10 8492 9402 Fax : +86-10 8492 7216

MIRA China Ltd.
Unit E, B1F, Building A, Synnex International Park, No. 1068 Tianshan West Road, Shanghai 200335, China
Phone : +(86)-21-6220-6377 Fax : +(86)-21-6220-6379

Xiangyang Workshop
A27-1, Jiahai industrial park, High-tech District, Xiangyang, Hubei, 441004, China
Phone : +(86)-710-2578-268

INDIA

HORIBA India Private Limited
246, OKHLA INDUSTRIAL ESTATE, PHASE 3 NEW DELHI - 110020, India
Phone : +91-11-4646-5000 Fax : +91-11-4646-5020

Bangalore Office
3rd, No.504, 22nd Cross HSR Club Road Sector-3, Bengaluru, Karnataka, 560102, INDIA
Phone : +(91)-80-4127-3637

Chennai Office
No.9, 01 & 02 Floor,Ganapathy Colony,Thiru-Vi-Ka Industrial Estate,Guindy, Chennai ,600032 India
Phone : +(91)-44-42077899

Haridwar Factory
Plot No. 26, Sector-7, IIE, SIDCUL, Haridwar, Uttarakhand - 249403, India
Phone : +(91)-1334-239139

Kolkata Office
EK Tower/6th Floor/Office -4A, Action Area-II D, Newtown, Pin Code 700161,India
Phone : +(91)-90073-63356

Nagpur Factory
Plot No B-3, C-32, MIDC Industrial Area, Butibori, Phase 2, Nagpur, Maharashtra, 441122, India
Phone : +(91) 71-0328-0200

Technical Center
D-225,Chakan MIDC Phase-II, Bhamboli Village, Pune-410501., India
Phone : +(91) 21-3567-6000

INDONESIA

PT HORIBA Indonesia
Jl. Jalur Sutera Blok 20A, No. 16-17, Kel. Kunciran, Kec. Pinang Tangerang - 15144, Indonesia
Phone : +62-21-3044 8525 Fax : +62-21-3044 8521

KOREA

HORIBA KOREA Ltd.
25, 94-Gil, Iljik-Ro, Manan-Gu, Anyang-Si, Gyeonggi-Do, 13901, Korea
Phone : +(82)-31-296-7911 Fax : +(82)-31-296-7913

Ulsan Office
613, Doosan We've the Zenith, 1877, Sinjeong-Dong, Nam-Gu, Ulsan-Si, 44679, Korea
Phone : +(82)-52-275-0122 Fax : +(82)-52-276-0136

HORIBA STEC KOREA, Ltd.
98, Digital valley-ro Suji-gu, Yongin-si Gyeonggi-do 16878 Korea
Phone : +(82)-31-8025-6500 Fax : +(82)-31-8025-6599

PHILIPPINES

HORIBA INSTRUMENTS (SINGAPORE) PTE LTD., MANILA OFFICE
27/F Tower 2, The Enterprise Center, 6766 Ayala Avenue corner Paseo de Roxas, Brgy. San Lorenzo, Makati City, Philippines, 1226
Phone : +63 2 8885 8468 Fax : None

SINGAPORE

HORIBA Instruments (Singapore) Pte Ltd
3 Changi Business Park Vista #01-01, Singapore 486051
Phone : +(65)-6-745-8300 Fax : +(65)-6-745-8155

West Office
83 Science Park Drive, #02-02A, The Curie, Singapore 118258
Phone : +(65)-6-908-9660

TAIWAN

HORIBA Taiwan, Inc.
8F.-8, No.38, Taiyuan St. Zhubei City, Hsinchu County 30265, Taiwan (R.O.C.)
Phone : +(886)-3-5600606 Fax : +(886)-3-5600550

Tainan Office
1F., No.90 Ziyou Rd., Shanhua Dist., Tainan City, 74158, Taiwan (R.O.C.)
Phone : +(886)6-581-1108 Fax : +(886)6-581-1160

THAILAND

HORIBA (Thailand) Limited
46/8 Rungrojthanakul Bld., 1st, 2 nd Floor Ratchadapisek Road., Huai Khwang, Bangkok 10310, Thailand
Phone : +66 (0) 2 861 5995 ext.123 Fax : +66 (0) 2 861 5200

HORIBA Holding (Thailand) Limited
46/8 Rungrojthanakul Bld., 1st, 2 nd Floor, Ratchadapisek Road., Huai Khwang, Bangkok 10310, Thailand
Phone : +(66)-2-861-59-95 Fax : +(66)-2-861-52-00

VIETNAM

HORIBA Vietnam Company Limited
Lot 3 and 4, 16 Floor, Detech Tower II, No. 107 Nguyen Phong Sac Street, Dich Vong Hau Ward, Cau Giay District, Hanoi, Vietnam
Phone : +(84)-24-3795-8552 Fax : +(84)-24-3795-8553

Branch in Ho Chi Minh city
7th Floor, No 09 Dinh Tien Hoang Street, Da Kao Ward, District 1, Hochiminh City, Vietnam
Phone : +84 2871095386

Readout **HORIBA Technical Reports English Edition No.57**

Publication Date : August 31st, 2023
Publisher : HORIBA, Ltd.
Editor : NAKAMURA Hiroshi
Associate Editor : NOMURA Satoshi
Publication Members : NAKATANI Shigeru, URAKAMI Chikako
MATSUDA Tetsuya, SAKAMOTO Junichi, OKAMOTO Naoko, SATAKE Hiromi
DTP, Printing : SHASHIN KAGAKU Co., Ltd.
Information : R&D Planning Center, R&D Division, HORIBA, Ltd.
2, Miyanohigashi-cho, Kisshoin, Minami-ku, Kyoto 601-8510, Japan
Phone : (81)75-313-8121
E-mail : readout@horiba.co.jp
URL : https://www.horiba.com/publications/readout/

HORIBA

Explore the future